U.S. Department of Transportation

Federal Railroad Administration

Discrete Element Modeling of Railroad Ballast Behavior

Office of Research,
Development
and Technology
Washington, DC 20590

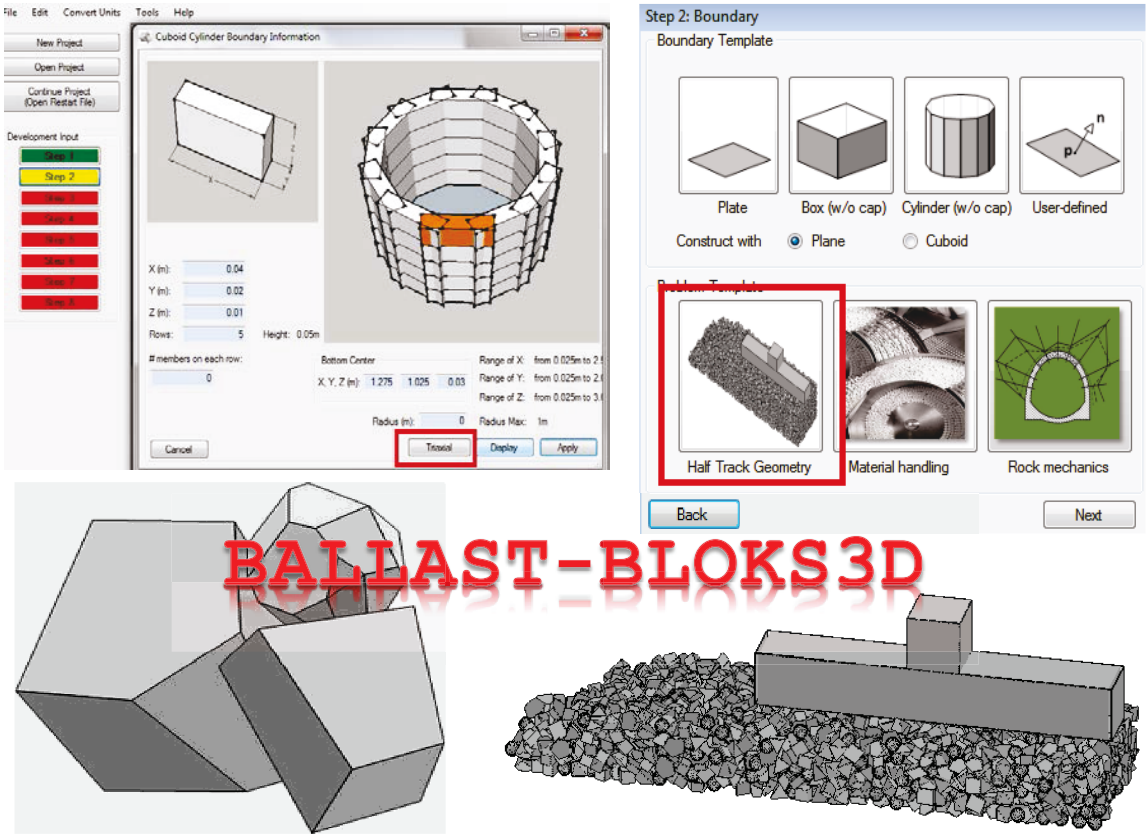

DOT/FRA/ORD-18/20

Final Report
July 2018

REPORT DOCUMENTATION PAGE

Form Approved
OMB No. 0704-0188

1. AGENCY USE ONLY (Leave blank)	2. REPORT DATE	3. REPORT TYPE AND DATES COVERED
	July 2018	Technical Report 2011–2013

4. TITLE AND SUBTITLE
Discrete Element Modeling of Railroad Ballast Behavior

5. FUNDING NUMBERS
FR-RRF-0033-11-01-00

6. AUTHOR(S)
Erol Tutumluer, Youssef M.A. Hashash, Jamshid Ghaboussi, Yu Qian, Seung J. Lee, and Hai Huang

7. PERFORMING ORGANIZATION NAME(S) AND ADDRESS(ES)
University of Illinois Urbana-Champaign
1901 S 1st St, Ste A
Champaign, IL 61820-7473

8. PERFORMING ORGANIZATION REPORT NUMBER

9. SPONSORING/MONITORING AGENCY NAME(S) AND ADDRESS(ES)
U.S. Department of Transportation
Federal Railroad Administration
Office of Railroad Policy and Development
Office of Research, Development and Technology
Washington, DC 20590

10. SPONSORING/MONITORING AGENCY REPORT NUMBER
DOT/FRA/ORD-18/20

11. SUPPLEMENTARY NOTES
COR: Hugh Thompson

12a. DISTRIBUTION/AVAILABILITY STATEMENT
This document is available to the public through the FRA Web site at http://www.fra.dot.gov.

12b. DISTRIBUTION CODE

13. ABSTRACT (Maximum 200 words)

An innovative integrated computational-experimental laboratory testing framework has been developed at the University of Illinois at Urbana-Champaign to evaluate clean and fouled ballast behavior. The railroad ballast layer consists of discrete aggregate particles and it is a critical substructure component that controls the track response under repeated train loading. Laboratory experiments and discrete element numerical simulations were performed to understand the underlying mechanisms of the complex ballast behavior and to provide the quantitative evaluation of response under periodic train loading. Large scale triaxial tests were performed in the laboratory under controlled monotonic and repeated loading conditions for shear strength, modulus, and deformation characteristics. A user-friendly discrete element simulation platform, BALLAST-BLOKS3D, was also developed. It utilizes realistic polyhedral particles digitally quantified from image analysis technology. The behavior of clean and fouled ballast was successfully studied via BALLAST-BLOKS3D.

14. SUBJECT TERMS
Ballast behavior, discrete element modeling, DEM, Discrete Element Method, triaxial test, fouling, dynamic train loading, ballast degradation and image analysis

15. NUMBER OF PAGES
97

16. PRICE CODE

17. SECURITY CLASSIFICATION OF REPORT	18. SECURITY CLASSIFICATION OF THIS PAGE	19. SECURITY CLASSIFICATION OF ABSTRACT	20. LIMITATION OF ABSTRACT
Unclassified	Unclassified	Unclassified	

NSN 7540-01-280-5500
Standard Form 298 (Rev. 2-89)
Prescribed by ANSI Std. 239-18
298-102

METRIC/ENGLISH CONVERSION FACTORS

ENGLISH TO METRIC	METRIC TO ENGLISH
LENGTH (APPROXIMATE)	**LENGTH (APPROXIMATE)**
1 inch (in) = 2.5 centimeters (cm)	1 millimeter (mm) = 0.04 inch (in)
1 foot (ft) = 30 centimeters (cm)	1 centimeter (cm) = 0.4 inch (in)
1 yard (yd) = 0.9 meter (m)	1 meter (m) = 3.3 feet (ft)
1 mile (mi) = 1.6 kilometers (km)	1 meter (m) = 1.1 yards (yd)
	1 kilometer (km) = 0.6 mile (mi)
AREA (APPROXIMATE)	**AREA (APPROXIMATE)**
1 square inch (sq in, in^2) = 6.5 square centimeters (cm^2)	1 square centimeter (cm^2) = 0.16 square inch (sq in, in^2)
1 square foot (sq ft, ft^2) = 0.09 square meter (m^2)	1 square meter (m^2) = 1.2 square yards (sq yd, yd^2)
1 square yard (sq yd, yd^2) = 0.8 square meter (m^2)	1 square kilometer (km^2) = 0.4 square mile (sq mi, mi^2)
1 square mile (sq mi, mi^2) = 2.6 square kilometers (km^2)	10,000 square meters (m^2) = 1 hectare (ha) = 2.5 acres
1 acre = 0.4 hectare (he) = 4,000 square meters (m^2)	
MASS - WEIGHT (APPROXIMATE)	**MASS - WEIGHT (APPROXIMATE)**
1 ounce (oz) = 28 grams (gm)	1 gram (gm) = 0.036 ounce (oz)
1 pound (lb) = 0.45 kilogram (kg)	1 kilogram (kg) = 2.2 pounds (lb)
1 short ton = 2,000 pounds (lb) = 0.9 tonne (t)	1 tonne (t) = 1,000 kilograms (kg)
	= 1.1 short tons
VOLUME (APPROXIMATE)	**VOLUME (APPROXIMATE)**
1 teaspoon (tsp) = 5 milliliters (ml)	1 milliliter (ml) = 0.03 fluid ounce (fl oz)
1 tablespoon (tbsp) = 15 milliliters (ml)	1 liter (l) = 2.1 pints (pt)
1 fluid ounce (fl oz) = 30 milliliters (ml)	1 liter (l) = 1.06 quarts (qt)
1 cup (c) = 0.24 liter (l)	1 liter (l) = 0.26 gallon (gal)
1 pint (pt) = 0.47 liter (l)	
1 quart (qt) = 0.96 liter (l)	
1 gallon (gal) = 3.8 liters (l)	
1 cubic foot (cu ft, ft^3) = 0.03 cubic meter (m^3)	1 cubic meter (m^3) = 36 cubic feet (cu ft, ft^3)
1 cubic yard (cu yd, yd^3) = 0.76 cubic meter (m^3)	1 cubic meter (m^3) = 1.3 cubic yards (cu yd, yd^3)
TEMPERATURE (EXACT)	**TEMPERATURE (EXACT)**
[(x-32)(5/9)] °F = y °C	[(9/5) y + 32] °C = x °F

QUICK INCH - CENTIMETER LENGTH CONVERSION

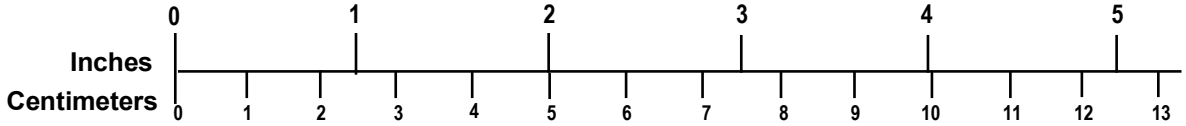

QUICK FAHRENHEIT - CELSIUS TEMPERATURE CONVERSIO

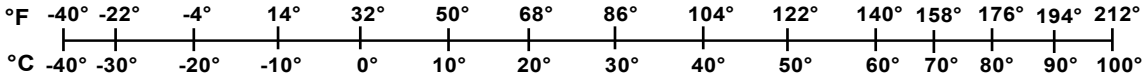

For more exact and or other conversion factors, see NIST Miscellaneous Publication 286, Units of Weights and Measures. Price $2.50 SD Catalog No. C13 10286

Updated 6/17/98

Acknowledgements

This research project was supported by the Federal Railroad Administration (FRA). The authors would like to acknowledge Mr. Gary Carr, Chief, Track Research Division at the FRA Office of Research, Development and Technology for his vision, leadership and research support. The authors also appreciate the valuable support and guidance provided by Mr. Hugh Thompson of FRA and Dr. Ted Sussmann of the Department of Transportation's Volpe Center.

Special thanks go out to the faculty and staff of the Rail Transportation and Engineering Center located at the University of Illinois at Urbana-Champaign (UIUC). Mr. James Pforr, Research Engineer at the Illinois Center for Transportation (ICT), as well as Dr. Debakanta Mishra and PhD students Hasan Kazmee and Huseyin Boler in UIUC's Department of Civil and Environmental Engineering provided considerable help with the laboratory large scale triaxial tests. In addition, Wenting Hou and Maziar Moaveni, also both PhD students provided help with the laboratory image analyses.

The development of DEEPSOIL has been directed by Prof. Youssef Hashash of UIUC for 10 years and it is acclaimed by software users around the world. DEEPSOIL's website is at: http://deepsoil.cee.illinois.edu/.

Contents

Illustrations

Tables

Executive Summary

From 2011 through 2013, the University of Illinois at Urbana-Champaign (UIUC) developed an innovative integrated computational-experimental laboratory testing framework for evaluating the behavior of clean and fouled ballast. To better understand the underlying mechanisms of complex ballast behavior and to provide the quantitative evaluation of response under periodic train loading, laboratory experiments and discrete element numerical simulations were performed. Also, the team developed a user-friendly Discrete Element Method (DEM) simulation computer program, BALLAST-BLOKS3D, which utilizes realistic polyhedral particles digitally quantified from image analysis technology.

A dynamic track model, which included discrete tie support and three-dimensional (3D) subgrade, provided realistic load pulse shapes, magnitudes, and rest periods acting on the ballast in the field. The loading cycle applied on ballast specimens in the laboratory testing environment and the DEM model simulations took into account the characteristics of the track, individual car axle spacing, car length, multiple wheel-load interaction, and train speed.

Large scale triaxial tests were performed in the laboratory on clean and fouled ballast under controlled monotonic and repeated loading conditions for shear strength, modulus, and deformation characteristics. The experimental study indicated that the shearing rate has no significant influence on the results of the triaxial tests of clean ballast.

The mechanisms and progression of ballast fouling were investigated: Stages of railroad ballast degradation were studied through Los Angeles (LA) abrasion tests. The aggregate image analysis approach is also utilized to investigate ballast particle abrasion and breakage trends at intermediate fouling stages through detailed quantifications of individual ballast particle size and shape properties.

The study results indicated that the commonly used Fouling Index (FI), which is expressed by the summation of percent (by weight) passing the No. 4 and No. 200 sieves, was indeed a good indicator of ballast fouling conditions. The index was particularly useful when all voids created by larger particles were filled by fine materials as FI values approached 40 for the heavily fouled case.

The ballast particles larger than 9.5 mm (3/8 in.) were subjected to a varying number of turns of the LA abrasion drum, and an image analysis exhibited good correlations between percent changes in aggregate shape properties, i.e., imaging based flatness and elongation, angularity and surface texture indices, and FI. Establishing relationships between in-service track fouling levels and ballast size and shape properties with similar field imaging techniques would help researchers understand field degradation trends and, as a result, improve ballast serviceability and life cycle performance.

The research team also developed a DEM simulation computer program named BALLAST-BLOKS3D that employs a graphical user interface (GUI). The platform successfully simulated confinement and applied stress conditions on cylindrical specimens, captured the stress-strain behavior of triaxial tests on clean ballast, and also showed that the “incremental displacement” shearing method (IDSM) can capture the measured shearing response. By adopting the IDSM in DEM computations, it is possible to simulate many more loading cycles during limited timeframe and with the available computational power. This approach was adopted to simulate

permanent deformation accumulation, assuming a realistic load pulse with rest period from typical freight train dynamic loading. The DEM simulations computed average permanent strains comparable to experimental results for up to 2,000 loading cycles, taking into account the effects of different initial conditions and proper specimen compaction in the laboratory.

1. Introduction

Ballast consists of discrete aggregate particles, and it plays an essential role in railroad track by providing load distribution and drainage. A basic understanding of the ballast engineering behavior plays an essential role in mitigating track problems and failures caused by fouled ballast, deformed ballast, pumping and degradation due to repeated train wheel load, and track shifts resulted of weak ballast.

1.1 Background

Insight into the compositions of the larger aggregate particles, the amount of fine fouling material, and the detrimental effects of the moisture retained but not drained in a fouled ballast layer can be gained by sampling new and used ballast and testing it for degradation and fouling with laboratory sieve analyses. Nonetheless, for a better evaluation of the serviceability and proper functioning of the existing ballast layer, the basis for a quantitative track performance simulation tool should be built by characterizing variables such as ballast strength, modulus, and deformation behavior in the laboratory and applied it to field by means of demonstrated a realistic and robust modeling capability.

1.2 Objectives

To better understand the particulate nature of granular interactions and associated complex mechanical behavior of ballast aggregate materials, in order to achieve this goal, the research effort currently developed to test the framework requirement of an integrated computational-experimental in laboratory to comprehend the complex ballast behavior under train loading environment.

1.3 Overall Approach

The strength, modulus and deformation characteristics of ballast materials are tested in the laboratory and are modeled by a Discrete Element Method (DEM) simulation platform. DEM modeling properly represents the particulate nature of different sized and shaped ballast aggregate particles as well as their interactions with each other at contact points for both clean and fouled ballast. This approach to modeling also allows researchers to better understand and improved ballast strength and stability; resistance to lateral and permanent deformations; and improved designs of bridge approaches of fixed structures, grade crossings and track transition zones.

1.4 Scope

The experimental and modeling research effort on ballast aggregates with the development of ballasted track performance simulation software are divided into four tasks:

1) Developing and enhancing the dynamic track loading model.
2) Conducting laboratory testing and evaluating the ballast samples.
3) Development of DEM capability to model ballast dynamic behavior.
4) Developing friendly graphical user interface for the ballast DEM model.

1.5 Organization of the Report

A dynamic track model was originally developed by Huang et al. (2010) and further studied and enhanced it to provide support for discrete ties and 3D subgrades modeling. The model properly identifies typical load pulse shapes, magnitudes and rest periods acting on the ballast in the field under realistic operating conditions for both freight and passenger trains at differing speeds. Accordingly, one load cycle applied on ballast specimens in the laboratory testing program and the DEM model simulations adequately generated realistic load pulse shapes and rest periods according to the characteristics of the track, individual car axle spacing, car length, multiple wheel load interaction, and train speed.

1.5.1 Laboratory Testing and Evaluation of Ballast Samples

Laboratory tests were conducted on both new and fouled ballast materials to determine basic aggregate properties, such as gradation and imaging-based aggregate particle shape indices Monotonic and repeated load dynamic tests determined strength and modulus, and large-scale triaxial test equipment was used to discover the permanent deformation properties of clean and fouled ballast materials. The key research findings from this research task are summarized below.

1. Shear strength of clean ballast was insensitive to shearing rate when studied through large scale triaxial tests in the laboratory.
2. Los Angeles (LA) abrasion test was used as the experimental approach in the laboratory to study ballast degradation and the test results showed good correlation with the most commonly used Fouling Index (FI) and aggregate particle image analysis based shape properties. The FI, summation of percent passing No. 4 and No. 200 sieves, was indeed a good indicator of fouling conditions especially when all voids created by larger particles were filled by fine materials when FI values approached 40, which corresponds to a heavily fouled ballast layer.
3. Clean ballast, heavily fouled ballast (FI=40), and the scalped gradation (or the coarse aggregates fraction with larger than 9.5 mm or 3/8 in. size) of the heavily fouled ballast (FI=40) showed permanent deformation accumulations in an expected orderly fashion. Accordingly, the lowest permanent deformation accumulated in the clean ballast samples. The largest accumulation of permanent deformation was in the heavily fouled ballast specimens and the scalped gradation of the heavily fouled ballast exhibited permanent deformation values in between the clean and the heavily fouled.
4. There are two important observations: 1) when the uniform ballast gradation changes from coarse to fine, there is an increase in permanent deformation accumulation, and 2) when the fine materials, smaller than 9.5 mm or 3/8 in. size, are present typically in a heavily fouled ballast sample, there is a significant increase in the permanent deformation accumulation.

1.5.2 Development of DEM Capability to Model Ballast Dynamic Behavior

The DEM simulation platform BALLAST-BLOKS3D was developed to model the ballast behavior from the laboratory triaxial test results. Efficient numerical approximations were carefully studied to represent the consequences of complex ballast sample deformation

mechanisms observed under monotonic and repeated load triaxial testing. The key research findings from this research task are summarized below:

1. The BALLAST-BLOKS3D software was used to simulate clean ballast behavior initially. The Polyhedral particles, which were developed via an image analysis based particle shape characterization technique and properly to represented the shape geometry of ballast particles in the DEM simulations. The developed DEM model provided reasonable levels of simulation fidelity in the estimated shear strength and permanent deformation responses of the ballast aggregates.
2. "Incremental displacement" shear method (IDSM) was successfully adopted for simulating both shear strength and permanent deformation type ballast mechanical behavior from large scale triaxial tests for computational efficiency with accuracy.
3. The DEM simulations took into account the effects of different initial conditions and proper specimen compaction in the laboratory to successfully predict average permanent strains comparable to experimental results for up to 2,000 loading cycles.

1.5.3 Development of Graphical User Interface for Ballast DEM Model

A user-friendly DEM software tool developed with the BALLAST-BLOKS3D program will allow easy and straightforward menu-driven inputs for ballast aggregate types and properties, including fouling/degradation trends and other relevant track geometry and loading characteristics. This tool beneficial used to conduct field applications and investigate various life-cycle or performance aspects of railroad ballast designs.

2. Background on Discrete Element Modeling

2.1 DEM for Granular Materials Research

A granular material assembly exhibits complex load-deformation behavior because it is neither completely solid nor fluid due to its discrete nature. To account for such particulate nature of granular materials in a simulation, the DEM has been proposed by Cundall and Strack (1979), and currently the most popular discontinuum-based numerical analysis approach. In DEM, a granular assembly is modeled as a discrete system in which each particle is modeled as an individual rigid element to explicitly account for particle interactions and associated energy dissipation. This is certainly more realistic when individual grain deformations are considered. Therefore, the DEM differs significantly from the continuum mechanics modeling framework, which utilizes the Finite Element Method (FEM). Theoretical overlaps between particles are considered as material deformation of the particles in contact, and used to determine the contact force via a certain contact force–deformation mechanics. Normal and shear springs are modeled between the particles to determine corresponding contact forces to each direction of the contact and the fundamental difference scheme utilized to integrate the second order differential equation of motion and the DEM calculation cycle as shown in Figure 2.1.

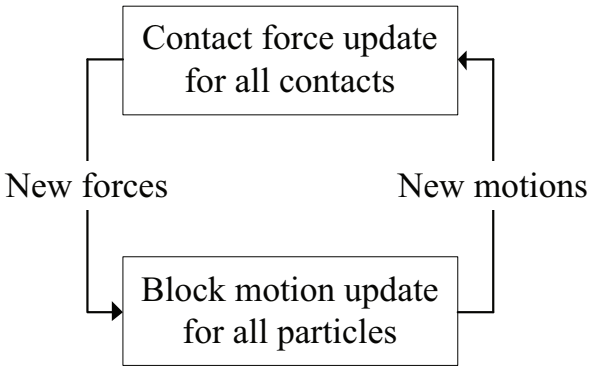

Figure 2.1. DEM Calculation Cycle (Cundall, 1988)

In the original DEM introduced in 1979, each particle was modeled as a two-dimensional (2D) disk. Later on, DEM has evolved to consider realistic particle shapes for more accurate interactions between particles (Cundall, P. A., 1988) (Barbosa, R., and Ghaboussi, J., 1990) (Sallam, A. M., 2004) (Zhao et al., 2006) (Hogue, C., and Newland, D., 1994) (O'Connor, R., and Williams, J. R., 1999) (Peña et al., 2007) (Garcia et al., 2008) (Andrade et al., 2012) (Mollon, G., and Zhao, J., 2013).

To generate and create realistic particle shapes requires expensive geometric testing for contact detection mechanism. Much improvement algorithmic developments have increased the speed of particle contact detection. In 1988, Common Plane (CP) method was first introduced and utilized in DEM simulations with polyhedral particle modeling to simplify particle-to-particle contact detection into a much faster particle-to-plane contact detection problem (Cundall, P. A., 1988). Later, Hashash, Ghaboussi and their colleagues have made significant algorithmic advancements that resulted in very fast particle contact detection (Ghaboussi et al., 2004) (Ghaboussi et al., 2006) and more usable DEM simulations with realistic polyhedral particles (Zhao et al., 2006) (Ghaboussi et al., 2007) (Agui et al., 2011) (Hashash et al., 2012).

2.2 DEM Modeling for Railroad Ballast Simulation

Generally, ballast aggregate materials are said to be uniformly graded in size with angular particle shapes and crushed faces. Ballast engineering properties, such as aggregate type and gradation, particle shape, texture and angularity, as well as particle hardness and abrasion resistance, can vary within certain conditions to influence overall track behavior and performance.

Previously, research on numerical modeling of ballast behavior in railroad tracks has focused on conducting DEM-based simulations of aggregate particle assemblies to address the particulate nature of ballast gradations. Indraratna et al. (2010) studied ballast behavior under cyclic loading, such as permanent deformation and degradation. They carried out 2D DEM simulations with fifteen particles of different shapes that represented ballast aggregates. The 15 particles were generated by cluster of bonded circular particles, which were obtained from a 2D projection of the real particles. Lu and McDowell (2010) studied ballast behavior by modeling ballast particles as a ten-ball triangular clump with eight small balls (asperities) bonded together. Indraratna et al. (2012) employed a similar modeling approach using sphere clumps in which a number of spheres were linked and overlapped to model irregular 3D particle shapes to study the direct shear behavior of fresh and fouled ballast.

This approach—using clumps of disks or spheres to represent ballast particles—has advantages such as keeping computational cost manageable, and it is relatively easier to simulate particle breakage. However, the approach generates particles with knobby surfaces, which makes it hard to realistically account for geometric interactions of particles at grain scale and capture corresponding macroscopic responses of ballast aggregates. As an indicator to the error, micromechanical parameters in published DEM simulations with the sphere-clumps often have been calibrated to unrealistic values, deviated from a typical range, e.g., inter-particle friction (commonly defined by ϕ'_{μ}) which has a range of typical values for each major mineral (Mesri, G., Peck, R. B., and Terzaghi, K., 1996) (Olson, S. M., and Sadrekarimi, A., 2011).

Therefore, realistic particle shapes are needed to enhance predictive capabilities and enable more systematic quantitative comparisons with experimental data. Tutumluer et al. (2006) introduced an image analysis-based approach to 3D aggregate shape recreation for representing individual ballast particle sizes and shapes, and to model polyhedral particles for use in 3D DEM simulations.

2.3 Previous DEM Studies at the University of Illinois

At the University of Illinois at Urbana-Champaign (UIUC), Barbosa and Ghaboussi developed the first polyhedral 3D DEM code, BLOCKS3D, to simulate granular particle flow (Barbosa, R., and Ghaboussi, J., 1990). During the ongoing efforts at UIUC, Ghaboussi et al. developed the second-generation polyhedral DEM code (BLOKS3D) from the ground up based on the original BLOCKS3D program (Ghaboussi et al., 2006). Note that BLOKS3D includes vastly enhanced particle shape properties and contact detection methods, which led to improved coding and significantly result faster computational algorithms therefore shortened DEM simulation run-times and consequently computationally affordable. In term, BLOKS3D code provides more realistic and accessible DEM simulation with the polyhedral elements generated from the image analysis results of ballast materials.

Tutumluer et al. used the University of Illinois Aggregate Image Analyzer (UIAIA) to develop key particle morphological indices such as the flat and elongated (F&E) ratio, the angularity index (AI), and the surface texture (ST) index for ballast particle shapes (Tutumluer et al., 2006). The DEM approach was first calibrated by large-scale laboratory direct-shear test results for ballast strength simulations (Huang, H., and Tutumluer, E., 2011). Then, the calibrated DEM model was utilized to model strength and settlement behavior of railroad ballast for the effects of multi-scale aggregate morphological properties (Tutumluer et al., 2006, 2007). The DEM model has also been used to investigate ballast gradation (Tutumluer et al., 2009) and fouling issues that are known to influence track performance (Dombrow et al., 2008) (Huang, H., and Tutumluer, E., 2011).

A successful field validation study was conducted with the ballast DEM simulation approach by constructing and monitoring field settlement records of four different ballast test sections and comparing the measured ballast settlements under monitored train loadings to DEM model predictions (Tutumluer et al., 2011). More recently, Hashash et al. (2012) presented realistic drained and undrained responses of sands via polyhedral DEM simulations of triaxial compression tests with BLOKS3D. They introduced new elements to represent triaxial cell membrane and rational successful computational approach to simulate the triaxial test results.

3. Development and Enhancement of Dynamic Track Loading Model

In this section, a dynamic track model originally developed by Huang et al. is enhanced to properly identify typical load pulse shapes, magnitudes and rest periods acting on the ballast in the field under realistic operating conditions of both freight and passenger trains at different speeds (Huang et al., 2010). The typical load pulse shapes, magnitudes and rest periods are needed for consideration in the laboratory testing program and the DEM model simulations.

Traditional dynamic track models are divided into two categories: analytical and numerical. Numerical models can take almost any track structural details into account (Banimahd et al., 2005). However, most of those models are very computationally expensive. Analytical models usually assume the track consists of continuously supported beam systems and they are usually much compute faster than numerical models (Grassie, S. L., and Knothe, K. L., 1993) (Cai, Z., and Raymond, G. P., 1994) (Blader et al., 1997) (Andersson, C., and Oscarsson, J., 1999).

For the purpose of track transition zone studies, traditional analytical solutions are no longer sufficient because a suitable track model has to have a critical component (the discretized tie supporting system). In other words, track can no longer be treated as continuous but rather as a beam supported at each individual tie position with possibly different supporting characteristics. Huang et al. proposed a 2D "Sandwich" model (see Figure 3.1) which semi-analytically solved a discretely supported beam system (Huang et al., 2010). In their study, subgrade was also treated as rigid and therefore, was not applicable to model track transition properly.

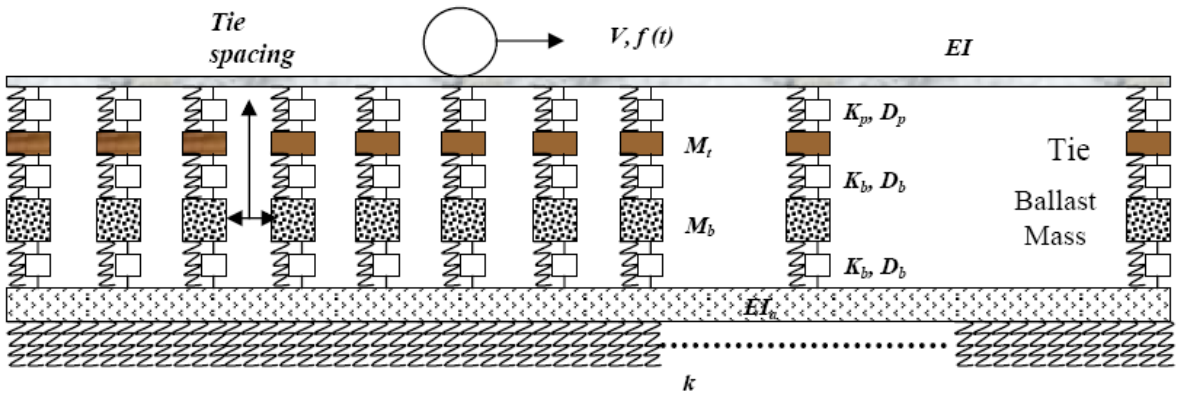

Figure 3.1. Beam-Discrete Support-Beam Model for Railroad with Asphalt Track Bed (Huang et al., 2010)

Using the derived solutions by Huang et al., forces on top of a single tie can be calculated from moving wheel loads and their realistic dynamic loading patterns (Huang et al., 2010). Figure 3.2 shows those forces computed on top of the tie at two different train speeds using standard US railcar configurations that were studied by Huang et al. (Huang et al., 2010). These two loading patterns fully consider realistic load pulses and the rest periods, i.e., the interactions between different axles and axle spacings. Accordingly, the faster the train travels the more independent the effects of the different axle loadings become.

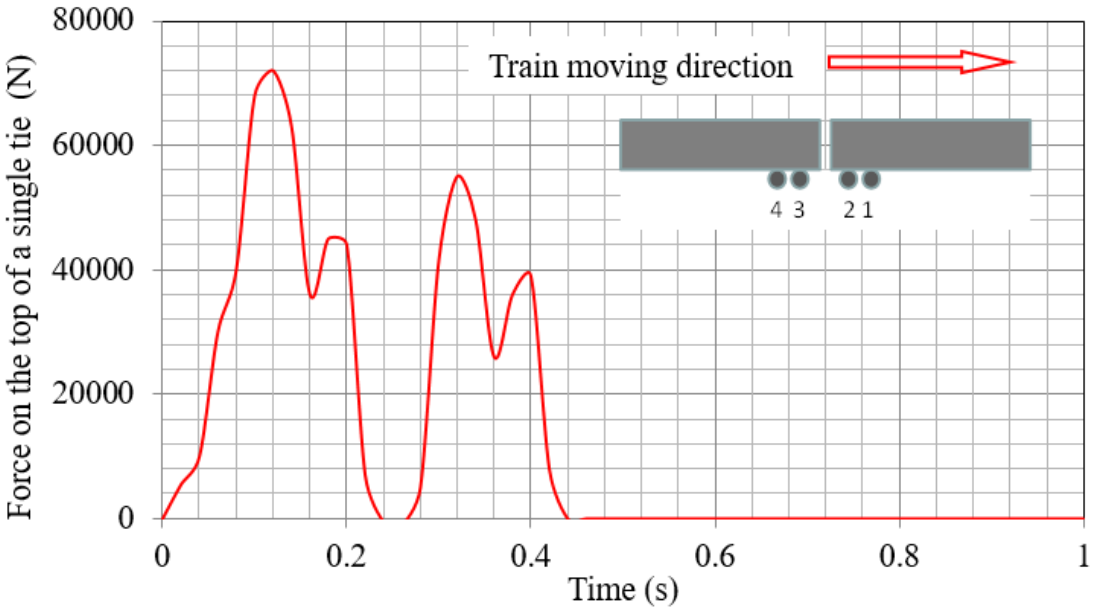

(a) Train moving at 73 km/h (peaks correspond to loads applied by 4 wheels)

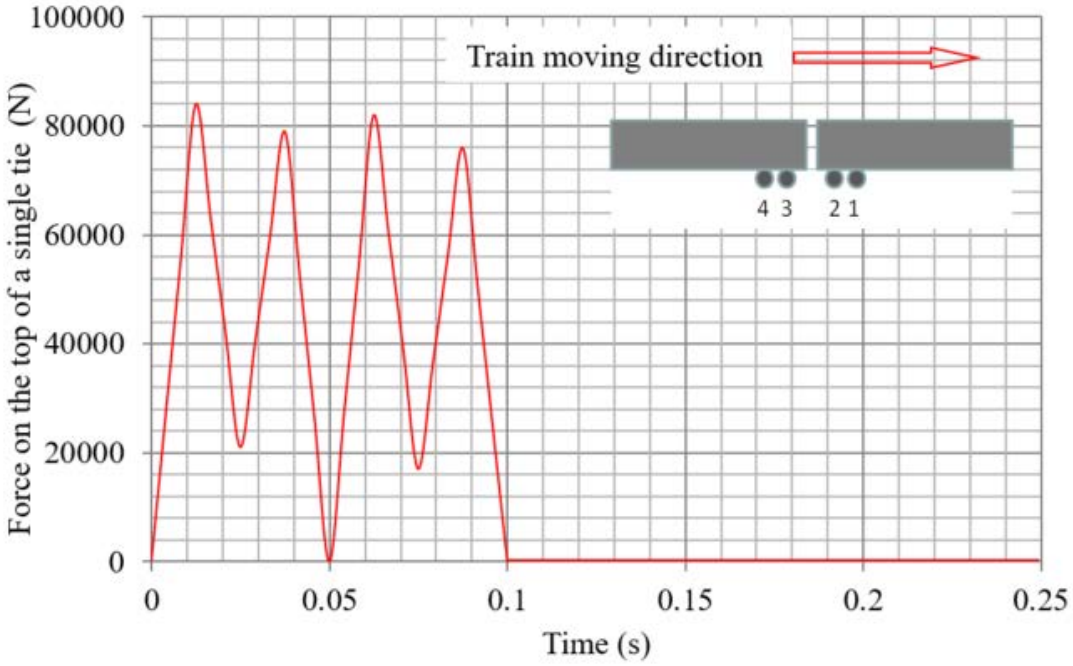

(b) rain moving at 291 km/h (peaks correspond to loads applied by 4 wheels)

Figure 3.2. Load Profile on Top of a Single Tie Under Moving Train Load from 2D "Sandwich Model" (Huang et al., 2010)

For the purposes of this project, a dynamic track model consists of a discretely tie supporting system and a 3D subgrade is introduced and solved by using the numerical Green Function technology. Figure 3.3 shows the 3D dynamic track model, which employs the beam-discrete tie supporting upper structure from previous research and a 3D subgrade which is discretized with a

finite element mesh (Huang et al., 2010). The solution includes computational steps that are outlined in the following subsections.

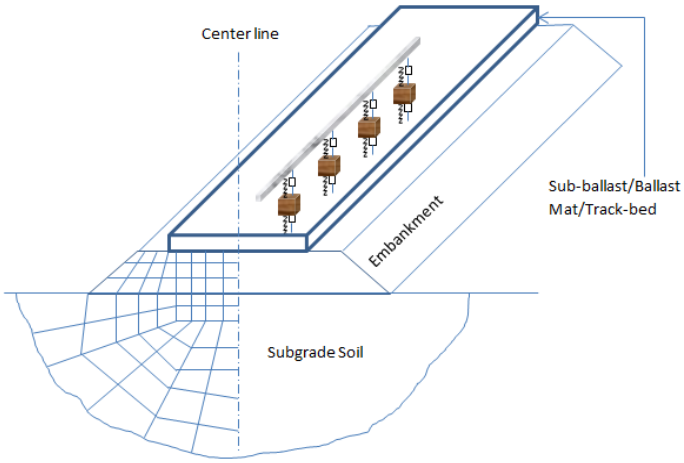

Figure 3.3. 3D Track Model for US Freight and High-Speed Rail Loads

3.1 Discrete Tie Support

Tie discrete tie support is derived using the following set of equations:

$$a_m(t) = \left(U_r(x_m,t) - U_t(x_m,t)\right)K_p(m) + \left(\dot{U}_r(x_m,t) - \dot{U}_t(x_m,t)\right)D_p(m) \quad (1)$$

$$b_m(t) = \left(U_b(x_m,t) - U_a(x_m,t)\right)K_b(m) + \left(\dot{U}_b(x_m,t) - \dot{U}_a(x_m,t)\right)D_b(m) \quad (2)$$

$$\left(U_r(x_m,t) - U_t(x_m,t)\right)K_p(m) + \left(\dot{U}_r(x_m,t) - \dot{U}_t(x_m,t)\right)D_p(m) - \left[\left(U_t(x_m,t) - U_b(x_m,t)\right)K_b(m) + \left(\dot{U}_t(x_m,t) - \dot{U}_b(x_m,t)\right)D_b(m)\right] = M_t(m)\ddot{U}_t(x_m,t) \quad (3)$$

$$\left(U_t(x_m,t) - U_b(x_m,t)\right)K_b(m) + \left(\dot{U}_t(x_m,t) - \dot{U}_b(x_m,t)\right)D_b(m) - \left[\left(U_b(x_m,t) - U_a(x_m,t)\right)K_b(m) + \left(\dot{U}_b(x_m,t) - \dot{U}_a(x_m,t)\right)D_b(m)\right] = M_b(m)\ddot{U}_b(x_m,t) \quad (4)$$

Where:

- $a_m(t)$ is the compression force at the mth tie between rail and support as a function of time
- $b_m(t)$ is the compression force at the mth tie between support and soil foundation as a function of time
- $U_r(x_m,t)$ is the rail deflection at the mth tie as a function of time
- $U_t(x_m,t)$ is the tie deflection at mth tie as a function of time

- $U_b(x_m, t)$ is the ballast deflection (including deformation) at the m[th] tie as a function of time
- $U_a(x_m, t)$ is the soil surface deflection at the m[th] tie as a function of time
- $K_p(m)$ is the stiffness of the m[th] pad
- $D_p(m)$ is the damping of the m[th] pad
- $K_b(m)$ is the stiffness of the ballast at the m[th] tie position
- $D_b(m)$ is the damping of the ballast at the m[th] tie position
- $M_t(m)$ is the mass of the m[th] tie
- $M_b(m)$ is the equivalent mass of ballast underneath the m[th] tie

Perform a Fourier Transform from time to frequency on these equations and express reaction forces in terms of rail and asphalt beam deflections:

$$a_m(\omega) = A_m U_r(x_m, \omega) + B_m U_a(x_m, \omega) \quad (5)$$

$$b_m(\omega) = C_m U_r(x_m, \omega) + D_m U_a(x_m, \omega) \quad (6)$$

Where:

$$A_m = DK_p(m)\left\{1 - \frac{1}{\frac{DK_b(m)^2}{DK_p(m)MK_b(m)} - \frac{MK_t(m)}{DK_p(m)}}\right\};$$

$$B_m = \left\{\frac{1}{1 - \frac{MK_t(m)MK_b(m)}{DK_b(m)^2}}\right\};$$

$$C_m = DK_b(m)\left\{\frac{1}{\frac{MK_t(m)MK_b(m)}{DK_p(m)DK_b(m)} - \frac{DK_b(m)}{DK_p(m)}}\right\};$$

$$D_m = -DK_b(m)\left\{1 + \frac{1}{\frac{MK_b(m)}{DK_b(m)} - \frac{DK_b(m)}{MK_t(m)}}\right\};$$

and: $DK_p(m) = K_p(m) + i\,\omega D_p(m)$; $DK_b(m) = K_b(m) + i\,\omega D_b(m)$; $MK_t(m) = M_t(m)\omega^2 - DK_p(m) - DK_b(m)$; $MK_b(m) = M_b(m)\omega^2 - 2DK_b(m)$.

3.2 Rail Beam

For rail, the governing equation is:

$$EIU_r(x,t)'''' + \rho U_r(\ddot{x},t) + \varepsilon U_r(\dot{x},t) + TU_r(x,t)'' = f(t)\delta(x-vt) - \sum_m a_m(t)\delta(x-x_m) \quad (7)$$

Where: EI is the bending stiffness of rail; $U_r(x,t)$ is the rail deflection as a function of time; ρ is the unit mass of rail; ε is damping of rail itself which will be set to zero for convenience; T is the rail axial force caused by temperature increase; $f(t)$ is the wheel load function; δ is the delta function; x_m is the location of the mth tie; and v is the wheel speed.

Performing Fourier Transform both from time to frequency and from "x" coordinate to wave length on Equation (7) yields

$$K(\lambda,\omega)U_r(\lambda,\omega) = f^t(\lambda v+\omega) - \sum_m a_m(\omega)e^{-ix_m\lambda} \quad (8)$$

Where f^t represents the Fourier Transformation from time to frequency; and $K(\lambda,\omega) = [EI\lambda^4 - T\lambda^2 - \omega^2\rho + i\varepsilon\omega]$.

$$U_r(\lambda,\omega) = \frac{1}{K(\lambda,\omega)}\left[f^t(\lambda v+\omega) - \sum_m a_m(\omega)e^{-ix_m\lambda}\right] \quad (9)$$

By applying Convolution Theorem and Inverse Fourier Transform, one obtains the following:

$$U_r(x,\omega) = \int_{-\infty}^{\infty} inv\left[f^t(\lambda v+\omega) - \sum_m a_m(\omega)e^{-ix_m\lambda}\right] K_r(x-y,\omega)dy \quad (10)$$

Where

$$K_r(x,\omega) = inv\left[\frac{1}{K(\lambda,\omega)}\right]$$

and "inv" is the inverse Fourier transformation from wave length back to "x" coordinate.

Since

$$inv[f^t(\lambda v+\omega)] = \frac{1}{2\pi}\int_{-\infty}^{\infty} f^t(\lambda v+\omega)\, e^{ix\lambda}d\lambda \quad (11)$$

$$inv[f^t(\lambda v+\omega)] = \frac{1}{2\pi}\int_{-\infty}^{\infty} f^t(Y)\frac{1}{v}e^{ixY/v}e^{-i\omega x/v}dY \quad (12)$$

which gives

$$inv[f^t(\lambda v+\omega)] = \frac{1}{v}f\left(\frac{x}{v}\right)e^{-\frac{i\omega x}{v}} \quad (13)$$

Also,

$$inv\left[\sum_m a_m(\omega)e^{-ix_m\lambda}\right] = \sum_m a_m(\omega)\delta(x - x_m) \tag{14}$$

which results in

$$U_r(x,\omega) = \int_{-\infty}^{\infty} \frac{1}{v} f(\frac{y}{v}) e^{-i\omega y/v} K_r(x-y,\omega)dy - \int_{-\infty}^{\infty} \sum_m a_m(\omega)\delta(y - x_m)K_r(x-y,\omega)dy \tag{15}$$

For $K_r(x,\omega)$, the following is used

$$K_r(x,\omega) = \frac{1}{2\pi}\int_{-\infty}^{\infty} \frac{e^{ix\lambda}}{EI\lambda^4 - T\lambda^2 - \omega^2\rho + i\varepsilon\omega} d\lambda \tag{16}$$

Use Residue Theorem and Jordan's Lemma and assume that "ε" becomes zero to solve this integral

For $\omega > 0$:

$$K_r(x,\omega) = -\frac{1}{4EIR\sqrt{R^2 - r^2}}\left(\sqrt{R - r}\, e^{-|x|\sqrt{R+r}} + i\sqrt{R + r}\, e^{-i|x|\sqrt{R-r}}\right) \tag{17}$$

where $R = \sqrt{r^2 + \omega^2 l^2}$; $r = \frac{T}{2EI}$; $l = \sqrt{\frac{\rho}{EI}}$

For $\omega < 0$, $K_r(x,\omega)$ is the complex conjugate of the previous solution.

To further solve this problem, the wheel load function $f(t)$ is assumed to have exponential behavior and have a time period from 0 to l:

$$f(t) = P_0(d - c\cos at); 0 < t < l \tag{18}$$

So, the first term in Equation (15) becomes

$$\int_{-\infty}^{\infty} \frac{1}{v} f\left(\frac{y}{v}\right) e^{-\frac{i\omega y}{v}} K_r(x-y,\omega) = \frac{P_0}{-4EIR\sqrt{R^2 - r^2}} \int_{-\infty}^{\infty} \frac{1}{v}\left(d - \frac{c}{2}e^{\frac{iay}{v}} - \frac{c}{2}e^{-\frac{iay}{v}}\right) e^{-\frac{i|\omega|y}{v}}\left(e^{-|x-y|\sqrt{R+r}} + i\sqrt{R+r}\, e^{-i|x-y|\sqrt{R-r}}\right)dy \tag{19}$$

Further

$$\int_{-\infty}^{\infty} \frac{1}{v} f\left(\frac{y}{v}\right) e^{-\frac{i\omega y}{v}} K_r(x-y,\omega)dy = \frac{P_0}{-4EIR\sqrt{R^2 - r^2}}\left[dg(0) - \frac{c}{2}\, g(a) - \frac{c}{2}\, g(-a)\right] \tag{20}$$

where

$$g(z) = \int_0^{vl} e^{\frac{izy}{v} - \frac{i|\omega|y}{v} - |x-y|\sqrt{R+r}} \sqrt{R-r} + ie^{\frac{izy}{v} - \frac{i|\omega|y}{v} - i|x-y|\sqrt{R-r}} \sqrt{R+r} dy \qquad (21)$$

To take off the "absolute" sign, the relationship between "x" and "y" needs to be discussed based on where "x" is. This process is omitted here in this report. In the end, deflection of rail in the frequency domain can be expressed as:

Where $F(x, w)$ is the result from Equation (20).

3.3 Three-Dimensional Soil

For 3D soil, a similar equation can be established and the 2.5D FEM technique is employed.

$$\{U_a(x_m, \omega)\} = [GS] * \{b_m(\omega)\} \qquad (23)$$

To solve for [GS], the Fourier Transform was only performed in the train moving direction and the transverse and vertical directions were discretized by Plane Stress Quadra-lateral Finite Elements. The stiffness matrix is expressed as:

$$[Ks] = \iint_{-1}^{1} (BN)^* C (BN) |J| d\xi d\eta \qquad (24)$$

Where

$$[B] = \begin{bmatrix} -i\lambda & 0 & 0 \\ 0 & \frac{\partial}{\partial \xi} & 0 \\ 0 & 0 & \frac{\partial}{\partial \eta} \\ \frac{\partial}{\partial \xi} & -i\lambda & 0 \\ 0 & \frac{\partial}{\partial \eta} & \frac{\partial}{\partial \xi} \\ \frac{\partial}{\partial \eta} & 0 & -i\lambda \end{bmatrix};$$

"C" is the Constitutive Matrix and

$$C = \begin{bmatrix} C_{11} & C_{12} & C_{13} & 0 & 0 & 0 \\ & C_{22} & C_{23} & 0 & 0 & 0 \\ & & C_{33} & 0 & 0 & 0 \\ & & & C_{44} & 0 & 0 \\ & sym & & & C_{55} & 0 \\ & & & & & C_{66} \end{bmatrix};$$

"N" is the shape function for a four-node quadratic element, "*" is the "Adjoin Matrix" operator, and "J" is the Jacobian. Therefore, the following FEM equation is obtained

$$([Ks] - (\omega - \lambda v)^2 * [M]) * \left[\overline{dS}\right] = [\bar{F}] \qquad (25)$$

For any frequency "ω," the soil surface deflection in frequency domain can be obtained by conducting discrete wave number Fourier Transform on equation 25. The results will form the matrix [GS] in Equation 23.

3.4 Model Assembling

To finally assemble the model, recall Equations (5), (6), (22) and (23). It can be seen that deflection of rail and asphalt beam at any position are functions of force vectors $\{a_m\}$ and $\{b_m\}$. To solve these two vectors, deflections at each support need to be solved. By substituting deflections at each support to Equation (22) and Equation (23), they are expressed in matrix forms:

$$\begin{Bmatrix} U_r(x_1,\omega) \\ U_r(x_2,\omega) \\ \vdots \\ U_r(x_{m,}\omega) \end{Bmatrix} = \begin{Bmatrix} F(x_1,\omega) \\ F(x_2,\omega) \\ \vdots \\ F(x_m,\omega) \end{Bmatrix} - \begin{bmatrix} A_1K_r(x_1-x_1,\omega) & A_2K_r(x_1-x_2,\omega) & \dots & A_mK_r(x_1-x_m,\omega) \\ A_1K_r(x_2-x_1,\omega) & A_2K_r(x_2-x_2,\omega) & \dots & A_mK_r(x_2-x_m,\omega) \\ \vdots & \vdots & \dots & \vdots \\ A_1K_r(x_m-x_1,\omega) & A_2K_r(x_m-x_2,\omega) & \dots & A_mK_r(x_m-x_m,\omega) \end{bmatrix} \begin{Bmatrix} U_r(x_1,\omega) \\ U_r(x_2,\omega) \\ \vdots \\ U_r(x_{m,}\omega) \end{Bmatrix} - \begin{bmatrix} B_1K_r(x_1-x_1,\omega) & B_2K_r(x_1-x_2,\omega) & \dots & B_mK_r(x_1-x_m,\omega) \\ B_1K_r(x_2-x_1,\omega) & B_2K_r(x_2-x_2,\omega) & \dots & B_mK_r(x_2-x_m,\omega) \\ \vdots & \vdots & \dots & \vdots \\ B_1K_r(x_m-x_1,\omega) & B_2K_r(x_m-x_2,\omega) & \dots & B_mK_r(x_m-x_m,\omega) \end{bmatrix} \begin{Bmatrix} U_a(x_1,\omega) \\ U_a(x_2,\omega) \\ \vdots \\ U_a(x_{m,}\omega) \end{Bmatrix} \qquad (26)$$

and

$$\begin{Bmatrix} U_a(x_1,\omega) \\ U_a(x_2,\omega) \\ \vdots \\ U_a(x_{m,}\omega) \end{Bmatrix} = [GS] * [C] * \begin{Bmatrix} U_r(x_1,\omega) \\ U_r(x_2,\omega) \\ \vdots \\ U_r(x_{m,}\omega) \end{Bmatrix} + [GS] * [D] * \begin{Bmatrix} U_a(x_1,\omega) \\ U_a(x_2,\omega) \\ \vdots \\ U_a(x_{m,}\omega) \end{Bmatrix} \quad (27)$$

They are simplified as:

$$\begin{bmatrix} AK_r + I & BK_r \\ GS * C & GS * D - I \end{bmatrix} \begin{Bmatrix} U_r(x_{1\ldots m},\omega) \\ U_a(x_{1\ldots m},\omega) \end{Bmatrix} = \begin{Bmatrix} F(x_{1\ldots m},\omega) \\ 0 \end{Bmatrix} \quad (28)$$

It is worth noting that the result solved so far are in the frequency domain. Fast Fourier Transform (FFT) needs to be performed to transform the solutions back to time domain.

With this derived solution, a computer program was developed and used to calculate the load profile applied on the top of each individual tie. The test track segment had 30 wood ties spaced at 0.508 m (20 in.). The wheel load had a function of $f(t) = 177187$ [a single wheel load derived from a 141750 kg (315 kip) car] moving at a speed of 17.8 m/s. The rail unit mass is 59 kg/m with a bending stiffness of 4.9 MN/m^2. The pad, tie, and ballast were set to a typical pad stiffness value of 280 MN/m; pad damping value of 63 kNsec/m; ballast stiffness value of 70 MN/m; ballast damping value of 82 kNsec/m; tie mass of 45 kg; and equivalent ballast mass of 420 kg (halftrack).

Figure 3.4 shows the loading profile on the top of a single tie for a train speed of 20 m/s or 73 km/h. It is worth noting that, again, the profile given in Figure 3.4 is the result after superposition of four running wheels which is equivalent to the traffic of one car passing. Figure 3.5 shows the computed rail deflections changing with increasing train speeds from 20 to 50 m/s.

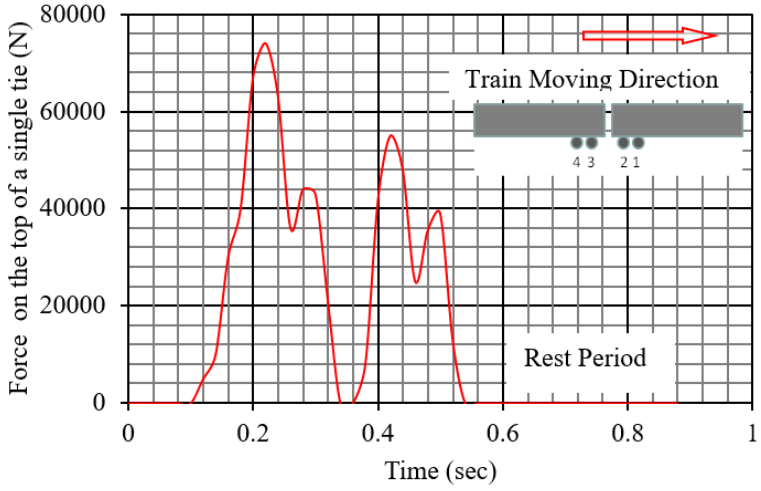

Figure 3.4. Load Profile on Top of a Single Tie Under Moving Train Load

As opposed to continuous load pulses, which are often applied previously by researchers during repeated load triaxial testing of ballast in the laboratory, the 3D dynamic track model presented

in this section considered more realistic moving wheel dynamic loading patterns. Therefore, a load cycle that has been applied on ballast specimens in the laboratory will need to take into account the realistic load pulses and rest periods as dictated by the characteristics of the track, individual car axle spacing, car length, multiple wheel load interaction and train speed.

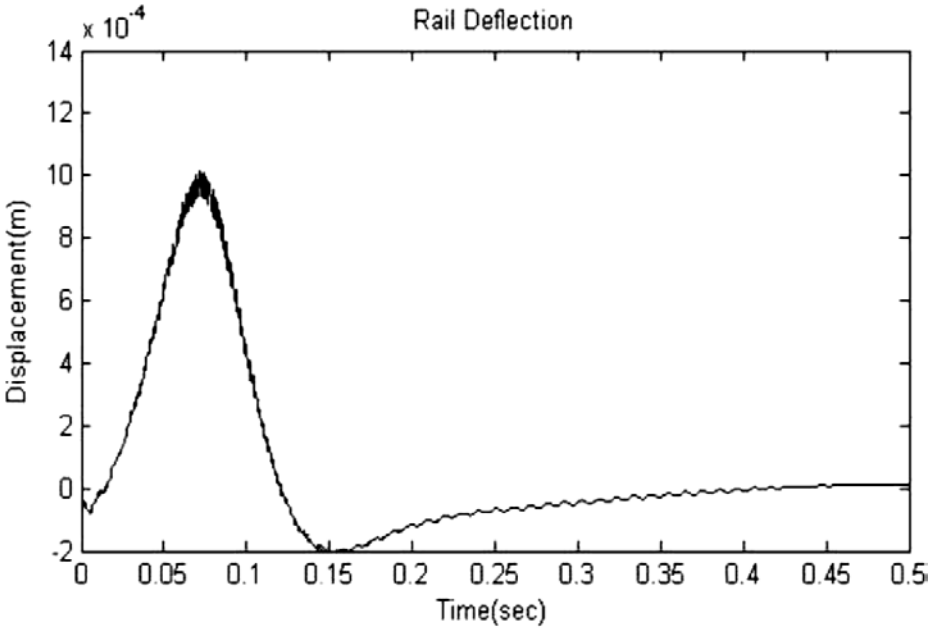

(a) Train speed of 20 m/s

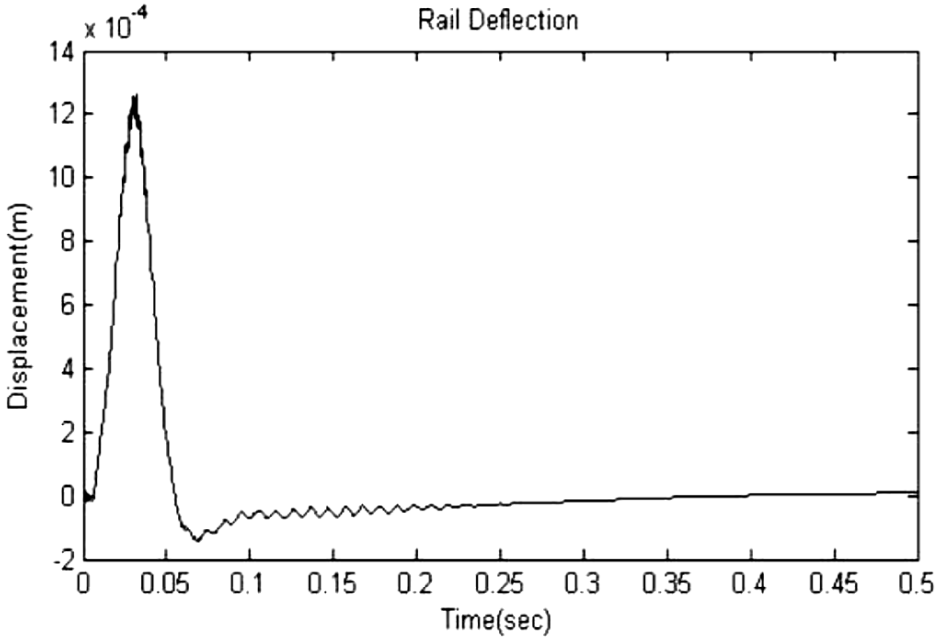

(b) Train speed of 50 m/s

Figure 3.5. Rail Deflections Changing with Increasing Train Speeds from 20 to 50 m/s

4. Study on the Clean Ballast Behavior via Lab Scale Experiments and DEM Simulations

4.1 Introduction to Laboratory Experiments on Ballast Aggregate Materials

To evaluate the field monotonic and repeated loading effects on ballast behavior, a large-scale triaxial test are traditionally performed in the laboratory and simulated by numerical methods. Selig and Waters described a box test that was used to investigate ballast behavior and performance under field condition, and they reported that ballast behavior under repeated loading was non-linear and stress-state dependent (Selig, E. T., and Waters, J. M., 1994). Selig and Waters also described a large-scale triaxial test used in ballast material testing and the test results demonstrated permanent deformation increased in a decreasing rate as number of loadings increased (Selig, E. T., and Waters, J. M., 1994). Han and Selig investigated of the effects of fouling material and degree of fouling on the settlement of a ballast bed in a ballast box developed in University of Massachusetts (Han, X., and Selig, E. T., 1996). The ballast test box had a dimension of 305 mm long, 305 mm wide and 610 mm deep. The test results confirmed fouled ballast yielded higher settlement as compared to clean ballast.

Raymond and Bathurst reported that the average vertical stress at the sleeper-ballast interface was approximately 140 kPa (20 psi) (Bathurst, R. J., and Raymound, G. P., 1994). Raymond investigated reinforced ballast behavior under repeated loading through box testing (Raymond G. P., 2002). The test box was 300 mm x 200 mm x 19 mm thick aluminum plate footing loaded by a 182 cm2 Bellofram piston. The test results demonstrated the benefit of using geosynthetics to reduce ballast settlement.

Suiker et al. did an experimental study on triaxial testing of a ballast material under cyclic loading (Frenkel, R., Selig, E. T., and Suiker, A. S. J., 2005). The nominal height of the cylindrical ballast specimen was equal to H=645 mm and the nominal diameter was equal to D=254 mm. The cyclic tests were performed using a periodic positive full-sine signal with a frequency of 5 Hz. The test results indicated that the ballast had a strong tendency to densify, even if the applied stress level is close to the failure strength under static loading.

Lackenby et al. conducted cyclic triaxial tests on ballast and indicated that the application of cyclic loading could lead to a considerable increase in material stiffness (Indraratna, B., Lackenby, J., and McDowell, G., 2007). Generally, the resilient modulus increased gradually with the number of repeated load applications as the material stiffens. Anderson and Fair conducted a series of large diameter triaxial tests on full sized and layered specimens to evaluate the influence of "stone blowing" (Anderson, W. F., and Fair, P., 2008). The nominal height of the cylindrical ballast specimen was equal to H=455 mm and the nominal diameter was equal to D=236 mm. An approximate square wave axial load-unload cycle in the range of 15 kPa and 250 kPa was applied to the specimen. Once the stones moved into the voids between ballast particles, plastic strain reduced significantly. Aursudkij et al. (2009) conducted another experimental study to investigate ballast behavior under cyclic loading. Using the railway test facility (RTF) at the University of Nottingham, a sinusoidal pulse up to 94 kN load magnitude and 90-degree phase lag was applied between different actuator load cycles.

More recently, Indraratna et al. conducted a large scale cyclic triaxial test to evaluate the influence of frequency on the permanent deformation and degradation behavior of ballast during

cyclic loading (Indraratna, B., Thakur, P. K., and Vinod, J. S., 2010). Cyclic triaxial tests were carried out using the large-scale triaxial equipment. A typical harmonic cyclic load was applied during the test program. The train dynamic loading effects due to different speeds were simply considered by changing the loading frequency and varying the maximum deviator stress due to wheel loading. Accordingly, a confining pressure of 60 kPa was selected for every test. Ebrahimi et al. also conducted large scale triaxial tests in University of Wisconsin-Madison on both clean and fouled ballast materials under cyclic loading, and reported that higher fouling and moisture content resulted in greater plastic strain (Ebrahimi, A., Edil, T. B., and Tinjum, J. M., 2010).

This study was to develop a ballast DEM simulation approach for modeling ballast shear strength and permanent deformation behavior from large scale triaxial tests. For ballast shear strength tests, both traditional slow and rapid shear loading approaches are adopted in the laboratory tests to investigate the effect of loading rate on ballast strength. Furthermore, in accordance with the results of the dynamic track model described in the previous section, a 0.4-second duration haversine loading with a 0.6-second rest period was applied to the specimens in the laboratory tests for investigating ballast permanent deformation behavior under repeated loading for 10,000 applied load cycles.

By utilized DEM to simulate laboratory triaxial tests, an "incremental displacement shearing method" (IDSM) by Hashash et al. was adopted to study the specimen response during the triaxial tests (Hashash, Y. M. A., Lee, S. J., and Nezami, E. G., 2012). The importance and influence of a DEM simulation's initial configuration is also investigated by conducting several DEM simulations with random initial configurations while other modeling parameters remained the same. The importance of sample preparation and compaction in DEM simulation is also studied.

4.1.1 Ballast Material Properties

The primary ballast material in the strength tests was a clean limestone with 100 percent crushed aggregates. Figure 4.1 shows the gradation properties of the ballast material, which met the AREMA No. 24 gradation requirements. Aggregate shape properties beyond the grain size distribution, especially the F&E ratio, the angularity index (AI), and the surface texture (ST) index, are key indices quantified by the recently enhanced University of Illinois Aggregate Image Analyzer (UIAIA). A full bucket of the ballast material was scanned and analyzed using the UIAIA to determine the values of the F&E ratio, AI, and the ST index. Then, these shape indices were used as the essential morphological data to generate ballast aggregate particle shapes as 3D discrete elements in the ballast DEM model (see Figure 4.2). Table 4.1 lists the gradation properties (C_u and C_c) and the average values of the limestone ballast shape indices used in the DEM simulations.

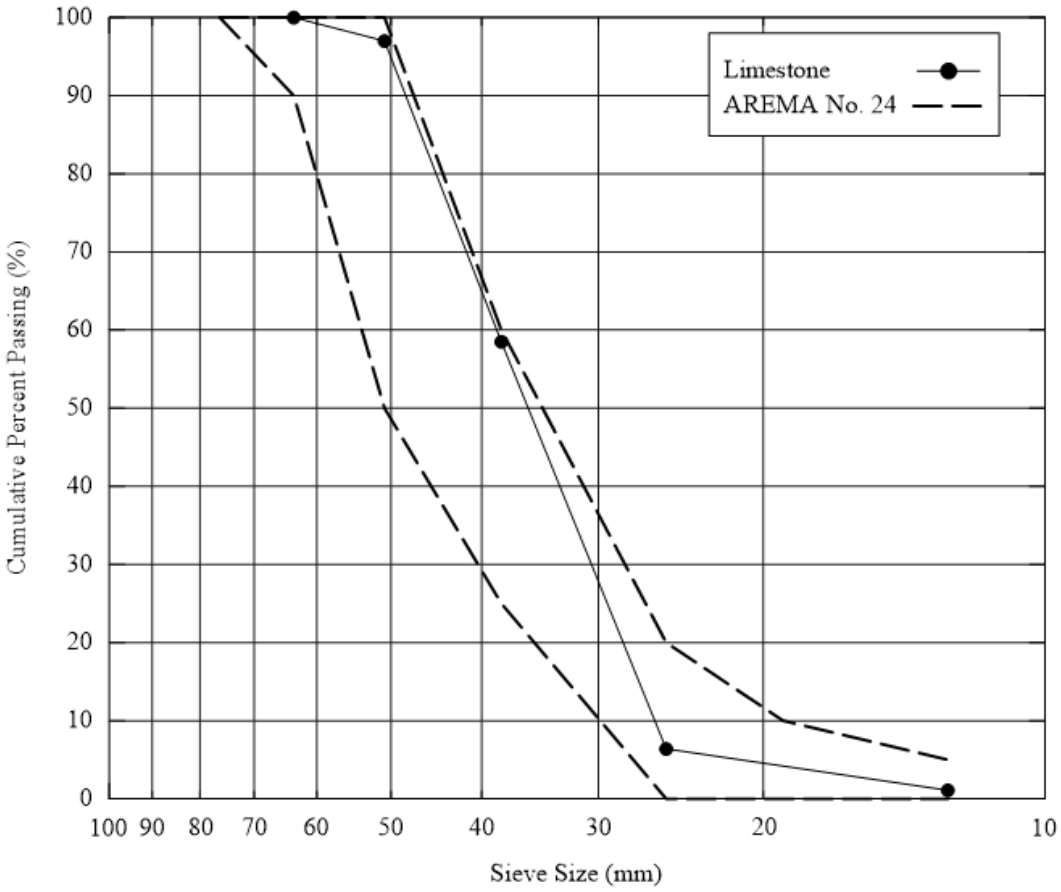

Figure 4.1. Gradation Properties of Limestone Ballast Material

Table 4.1. Properties and UIAIA Based Shape Indices of Ballast Material Tested

Ballast Type	Angularity Index (degrees)	Flat & Elongation Ratio	Surface Texture	C_u	C_c
Limestone	440	2.3	2	1.46	0.97

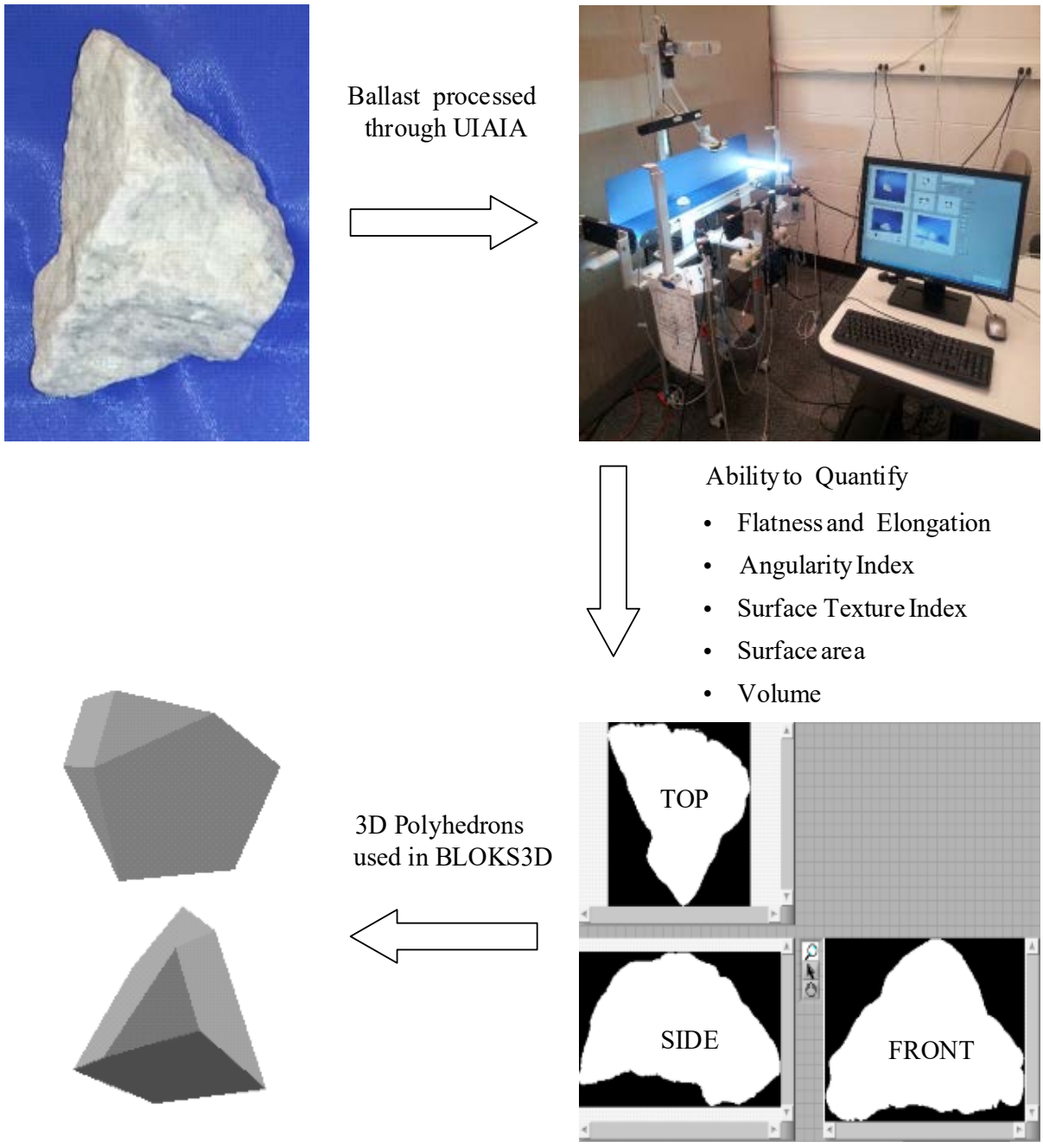

Figure 4.2. Aggregate Imaging Based Railroad Ballast Particle Characterization

4.1.2 Large Scale Triaxial Compression Test Device

A large scale triaxial compression test device (TX-24) has been developed at the University of Illinois specifically design for testing of different in ballast size aggregate materials, also in Gehringer et al. 2013 (see Figure 4.3). The test sample dimensions are 30.5 cm (12 in.) in diameter and 61.0 cm (24 in.) in height. The acrylic test chamber is made of high strength glass fiber with dimensions of 61.0 cm (24 in.) in diameter and 122.0 cm (48 in.) in height. An internal load cell with a capacity of 89 kN (20 kips) is placed on top of the specimen top platen

(Honeywell Model 3174). Three vertical LVDTs are placed around the cylindrical test sample, each at a 120-degrees angle between each other, to measure the vertical deformations of the specimen from three different side locations. Another LVDT can be also mounted on a circumferential chain, which would be wrapped around the specimen at the mid-height, to measure the radial deformation of the test sample (see Figure 4.4).

Figure 4.3. Large Scale Triaxial Test Device in the University of Illinois (TX-24)

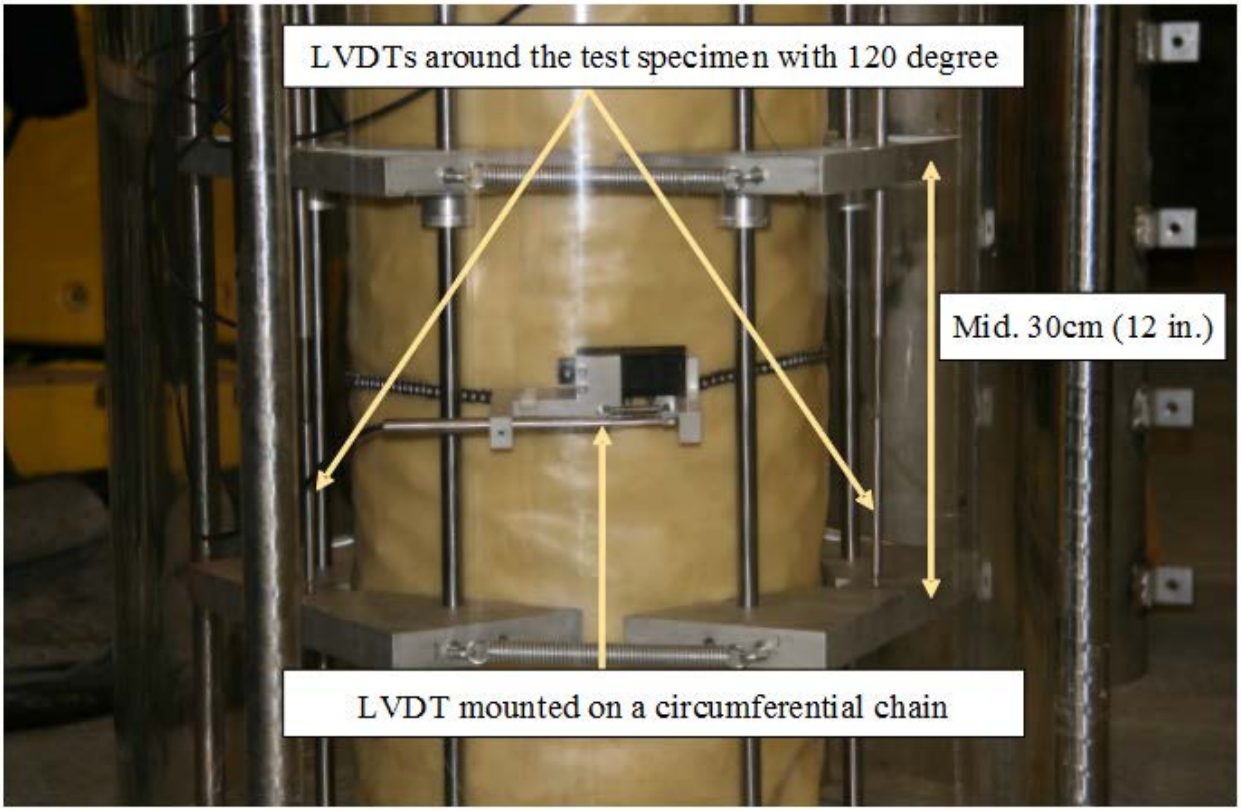

Figure 4.4. LVDTs Installed Around the Test Specimen (Circumferential Chain and the LVDT Mounted on it was Used During Triaxial Compression Test)

4.1.3 Ballast Sample Preparation

An aluminum split mold was used to prepare the ballast test samples. Three layers of a latex membrane, with a total thickness of 2.3 mm, were fixed inside the split mold and held in place with vacuum to prepare each specimen in layers. A thin layer of geotextile was placed on top of the base plate to prevent clogging of the vacuum pump. Approximately 68 to 73 kg (150 to 160 lbs.) of ballast material was poured into the mold evenly in four lifts, each lift constructed approximately 15 cm high (6 in.). The ballast sample was compacted with an electric jack hammer for about a 4 second interval during construction of each lift. After all four lifts were compacted. The test sample was checked for total height and the leveling of the top plate. A uniform compaction effort was applied for building each limestone ballast specimen with an achieved target void ratio of around 0.68. Figure 4.5 shows the aluminum split mold on the left and the compacted ballast sample on the right ready for triaxial testing.

4.1.4 Monotonic Compression Strength Tests

The monotonic-loading triaxial compression tests for the ballast strength were conducted at four different confining pressures arranged at 68.9 kPa (10 psi), 103.3 kPa (15 psi), 137.8 kPa (20 psi), and 206.7 kPa (30 psi) in displacement control mode. The ballast strength tests were conducted at two different loading rates either at slows conventional or rapid-traffic induced. The shearing rate for the slow conventional strength test was 1% strain per minute

(corresponding to 0.1016 mm/s), which is a common triaxial test shearing rate in standard soil mechanics or geotechnical engineering practice. Note that Garg and Thompson evaluated strength properties of granular materials under transportation vehicle loading at rapid monotonic loading rates of the ram, moving up to a maximum displacement of 38 mm (1.5 in.) per second (Garg, N., and Thompson, M. R., 1997). To investigated the influence of higher traffic-induced loading rate on the large-scale triaxial strength test with the results of ballast materials. Laboratory tests were conducted at the rapid shear rate of 5% strain per second and the slow shear rate of 1% strain per minute. Given that the high ballast specimen is 61.0-cm (24-in.), these loading rates correspond to vertical ram movements of 30.5 mm (1.2 in.) per second and 6.1 mm (0.24 in.) per minute, respectively. Since the large vertical movements of the ram caused instant bulging and shearing of ballast specimens, the circumferential chain and the LVDTs were not used during the ballast strength tests.

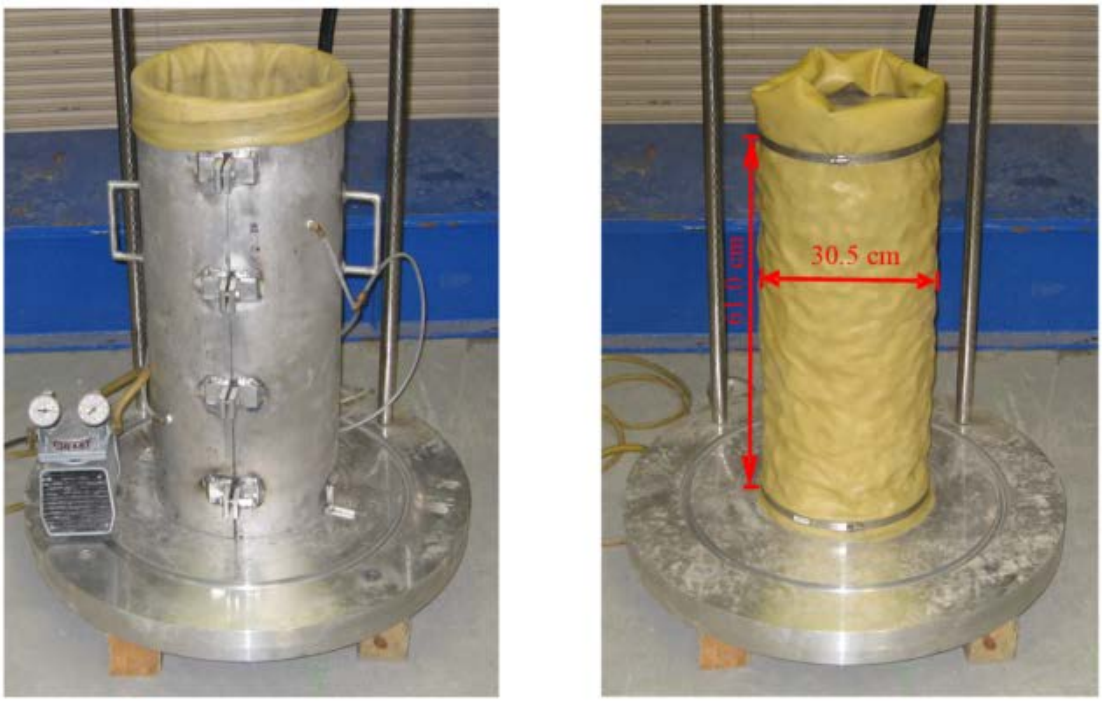

Figure 4.5. Test Specimen Preparation; (a) Aluminum Split Mold (b) Compacted Ballast Specimen (with the Split Mold Detached) for the Large-Scale Triaxial Compression Test

Once the large scale triaxial strength tests were conducted on the limestone ballast specimens and the results presented no significant differences in slow and rapid shearing rates that were adopted (see Figure 4.6). As expected, the maximum deviator stress increased as confining pressure increased, and the test results show the initial slope of stress-strain curve to be similar and consistent for the different confining pressures in both shearing rates. In other words, the rapid shearing rate of 5% strain per second, corresponding to 30.5 mm/s (1.2 in./s), and the slow shearing rate of 1% strain per minute, corresponding to 0.102 mm/s, yielded similar stress-strain curves at 68.9, 103.3 and 137.8 kPa (10, 15 and 20 psi) target confining pressures. Note that the missing slow shearing test in Figure 4.6 (the 206.7 kPa (30 psi) target confining pressure) was not performed. Nevertheless, Figure 4.6 clearly indicates that the shearing rate did not

significantly influence the ballast strength results in these monotonic loading tests. In other words, the ballast strength results from monotonic loading tests are not sensitive to the shearing rate. The rapid shear test was previously introduced to better simulate traffic loading conditions in the field and determine the strength properties (Garg, N., and Thompson, M. R., 1997); however, such a test has less tolerance for specimen misalignment. The rapid test can also raise safety concerns in a laboratory environment and the slow test is more advantageous in that the operator can better control the test boundary conditions.

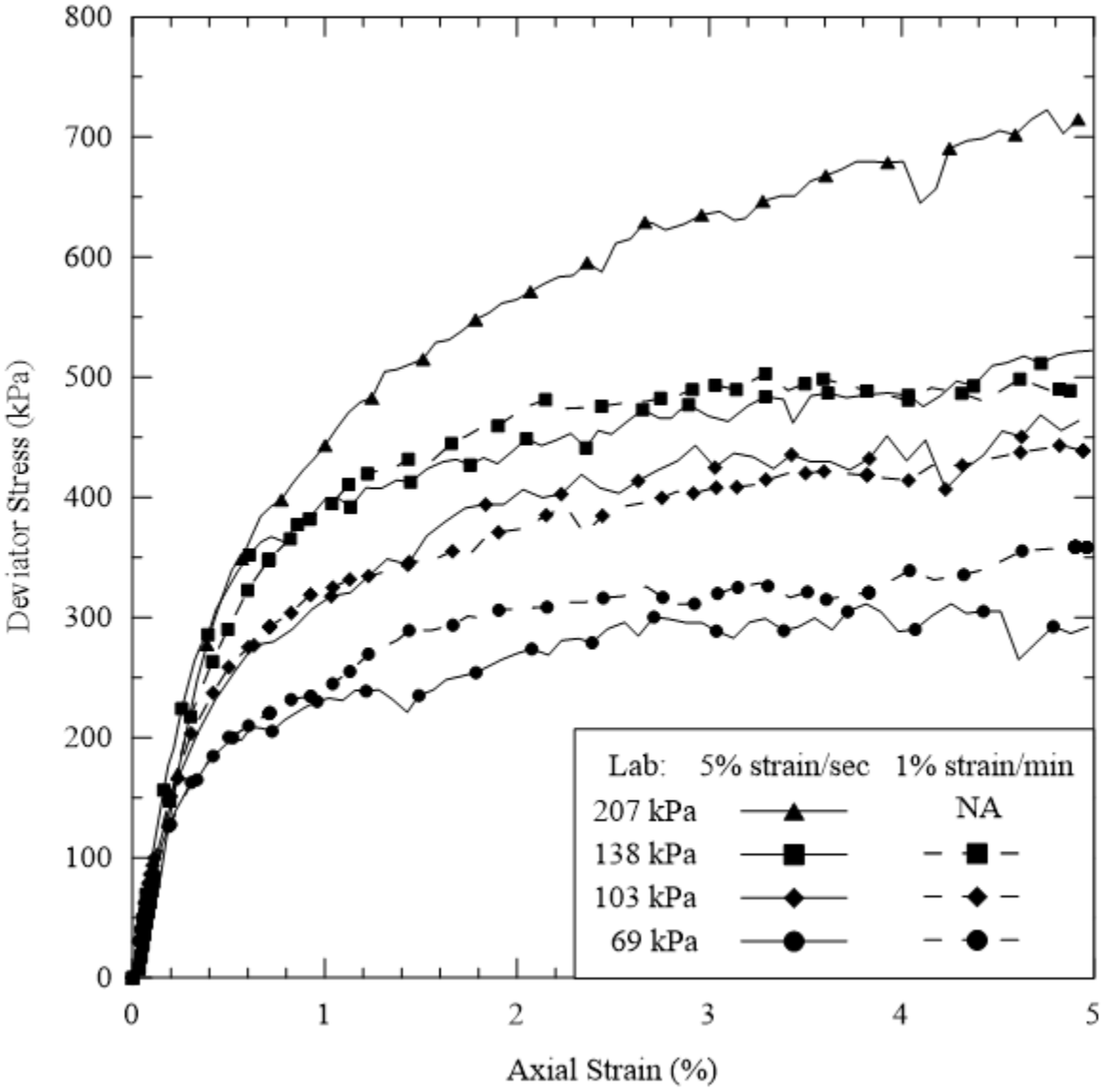

Figure 4.6. Laboratory Ballast Triaxial Compression Test Results

4.1.5 Permanent Deformation Tests with Repeated Loading

To investigate the ballast behavior under repeated loading, triaxial tests with repeated loading were conducted in the laboratory. The loading pulse employed haversine shape loading and the duration of each pulse is 0.4 seconds and 0.6 seconds for the rest period between each two

loading cycles (Figure 4.7). Note that these dynamic loading cycle characteristics were in accordance with the results of the dynamic track model, which realistically considered the effects of moving train loads. The confining pressure was 8 psi (55.1 kPa) and the peak deviator stress was 24 psi (165.4 kPa), which yielded a stress ratio of 4:1. Three specimens were prepared and experienced up to 10,000 cycles of the repeated loading. During each loading cycle, the deformation of the middle part of the specimen also recorded.

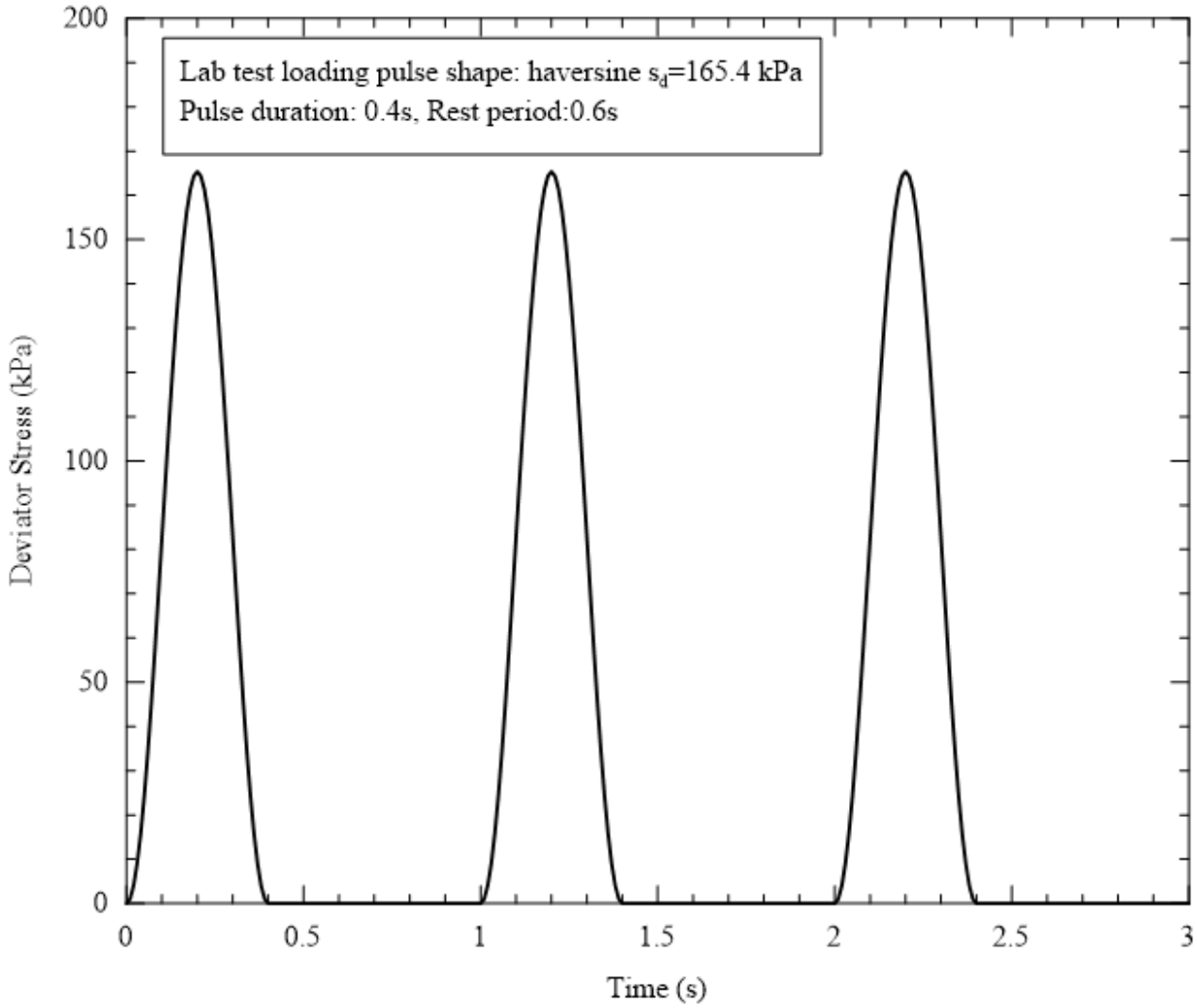

Figure 4.7. Laboratory Loading Pulse Used in Permanent Deformation

Large scale triaxial permanent tests were conducted on the limestone ballast specimens, and the results clearly demonstrated that permanent deformation increased as the number of loading cycles increased, but the rate of increase tends to decreased with the increasing of number of loading cycles. Similar findings were reported in previous studies (Selig, E. T., and Waters, J. M., 1994) (Frenkel, R., Selig, E. T., and Suiker, A. S. J., 2005) (Indraratna, B., Lackenby, J., and McDowell, G., 2007). Permanent deformations accumulated mainly during the first 2,000 cycles and then they increased very slowly and became stable with slight loading magnitude, the permanent strains for three different specimens after 10,000 loading cycles were relatively insignificant and varied from 0.5 percent to 1.3 percent (see Figure 4.8). The difference was

probably due to the settlement during initial configuration of the particle when comparing with the maximum ballast particle size over 50 mm and D50 of the gradation around 30 mm typically and 1% axial strain was only 3 mm.

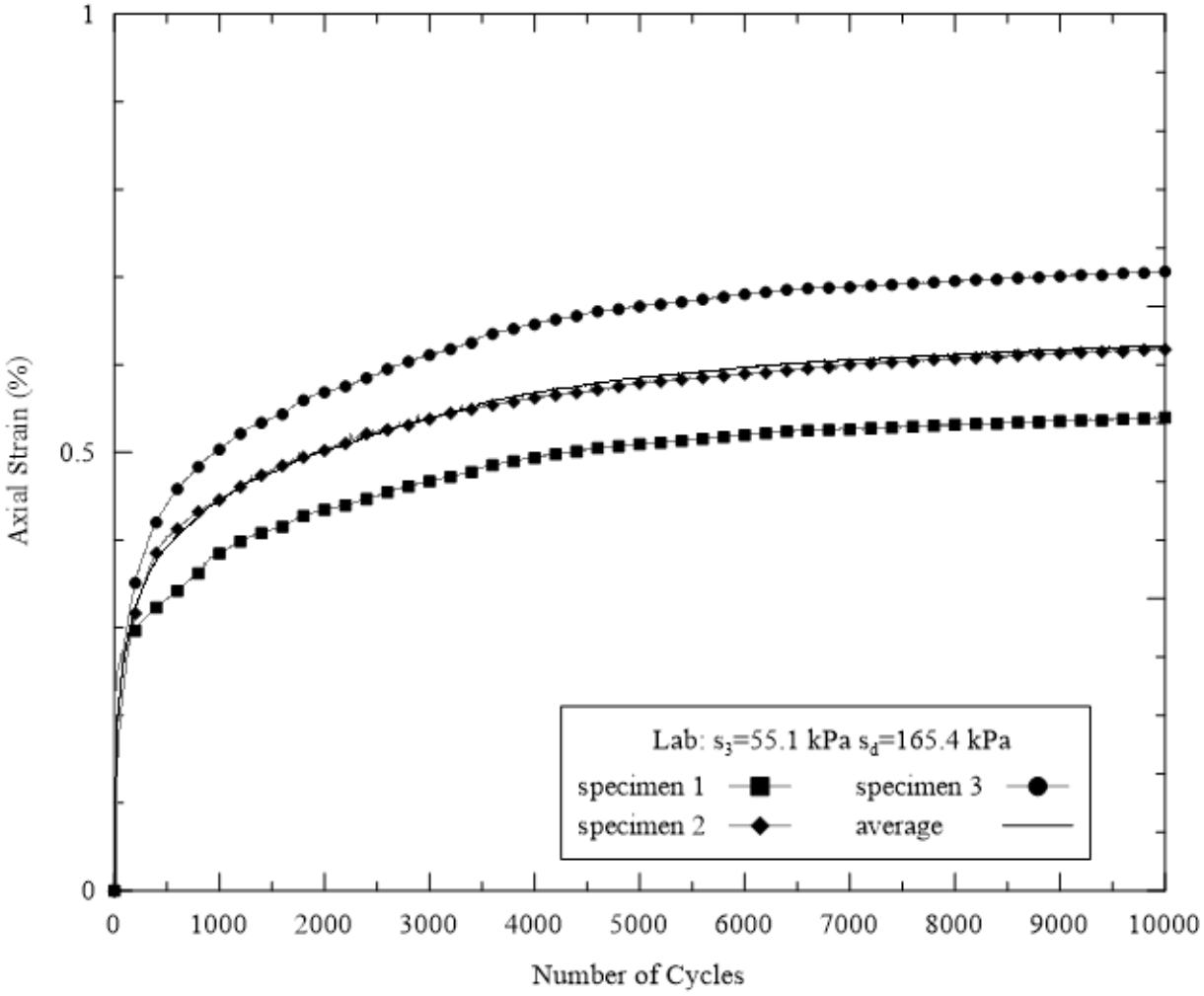

Figure 4.8. Laboratory Ballast Triaxial Permanent Deformation Test Results

4.2 DEM Simulations of the Laboratory Triaxial Tests

The following sections discuss various laboratory strength and deformation simulation tests that were conducted as part of the research effort.

4.2.1 Simulations of Clean Ballast Strength Tests

Flexible Membrane with Polyhedron Particles Simulation Technique

To properly simulate a laboratory triaxial test with DEM, the flexible membrane (i.e., specimen latex membranes) surrounding the ballast specimen must be modeled. Previous research efforts used chains of circular or spherical particles to simulate the membrane (Bardet, J. P., 1994) (Iwashita, K., and Oda, M., 2000) (Kacianauskas, R., and Markauskas, D., 2006) (Tonon, F., and

Wang, Y., 2009). Hashash et al. developed a variation of this approach for polyhedral DEM simulation, in which rigid rectangular cuboid discrete elements were positioned in a cylindrical arrangement to simulate the flexible membrane (Hashash et al., 2012). The Hashash et al. modeling approach was adopted by this study.

A cylindrical membrane chamber composed of 96 rigid rectangular cuboid discrete elements (in eight-layers) was used to confine the ballast specimen (as shown in Figure 4.9). Each layer had 12 equal sized elements and the dimension of each single element was 20.32 cm (8 in.) long, 10.16 cm (4 in.) wide, and 7.62 cm (3 in.) high. These elements were only allowed to move in a radial direction. Rotations and translations in the other directions were restricted to replicate membrane deformation. Note that these elements were required to have certain thickness to avoid gaps between vertically adjacent layers when differential radial displacements between them are relatively large. Similarly, the elements were also allowed to have sufficient lengths so horizontally adjacent elements overlap and keep the circular chamber closed during simulation of triaxial tests. No contact detection was made between these elements so each element allows moving freely, independent of neighboring elements. The friction between the membrane elements and the ballast particles was ignored by the DEM simulations. This is simply an approximation adopted in the simulation when friction between membrane and soil particles is assumed that it does not play an important role in the complex triaxial response.

After the membrane was formed, around 500 particles were poured into the cylinder and the top platen was placed on top of the sample. In order to achieve the target density, a technique of compact the specimen was required, as was done in the experiment for each test specimen and commensurate confining pressure. Once the DEM ballast sample preparation was done, the shear loading could be performed by vertically moving a top platen. The ballast particles in the DEM simulation were randomly generated in BLOKS3D, according the gradation and shape library defined, so the initial configuration was different from one simulation to another. Therefore, the DEM simulations were repeated three times for each test scenario and an average value of the three simulations was taken to reduce the initial configuration effect. The details of the model parameters in the DEM simulations are in Table 4.2.

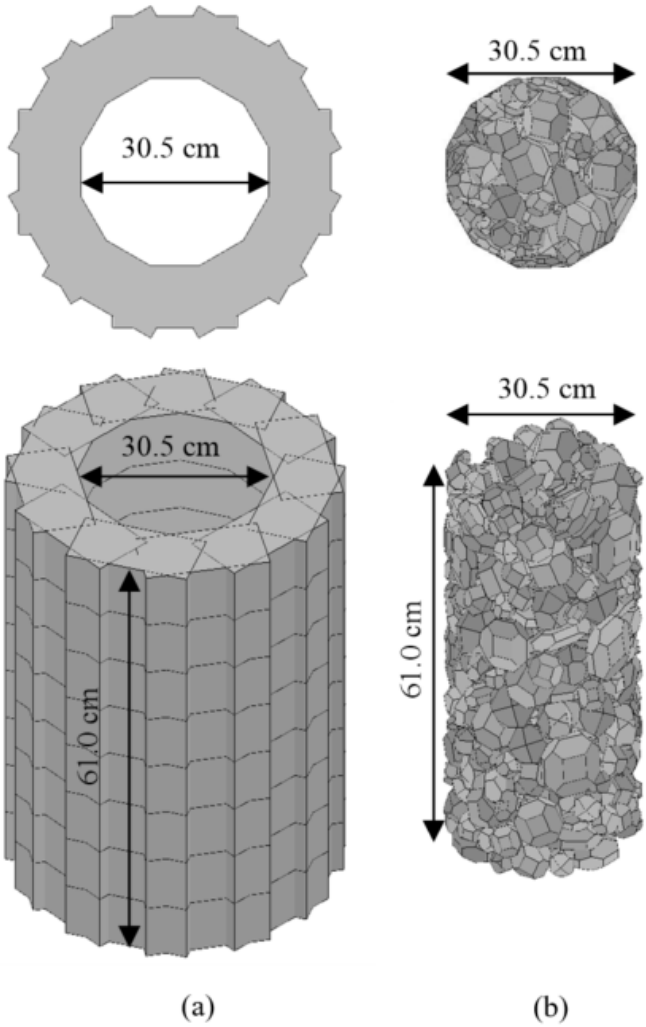

Figure 4.9. Ballast Specimen Used in the DEM Simulation; (a) Flexible Membrane (b) Confined Ballast Specimen in the Triaxial Compression Test Chamber

Incremental Displacement Shear Method

In the case of slow loading tests, each ballast sample was sheared at a rate of 0.102 mm/s, and it only took 5 minutes to reach the targeted 5 percent of axial strain in the laboratory. For the DEM simulations, 2.70×10^{-6} seconds of time step Δt was taken, resulting in as many as 1.11×108 time steps required to reproduce a triaxial test. Accordingly, it took around 15 days to complete a single DEM simulation, which means it is not practical to repeat DEM simulations and get meaningful averaged values of the results. Therefore, an alternative approach was adopted, known in this report as the "incremental displacement" shearing method (IDSM), that can mimic a quasi-static loading scheme while saving a sizable amount of CPU computational resources and run time. Although Hashash et al. did not refer IDSM specifically, it was successfully employed by the team to simulate triaxial compression tests of sand (Hashash et al., 2012). In Hashash et al., the top platen was allowed to move incrementally to shear the sand specimen, rather than moving it continuously, and the stresses and strains were calculated after the test specimen reached equilibrium under the new boundary condition (Hashash et al., 2012). This

dynamic relaxation scheme could shorten the run-time to simulate quasi-static problems. Similar approaches taken by DEM simulations of triaxial tests can also be found in other past studies (Iwashita, K., and Oda, M., 2000) (Tonon, F., and Wang, Y., 2009).

Table 4.2. Model Parameters Used in Ballast DEM Triaxial Test Simulations

DEM Model Parameter	Value
Inter-particle Friction Angle	31°
Normal Contact Stiffness	20 MN/m
Shear Contact Stiffness	10 MN/m
Global Damping	0.06
Contact Damping	0.03
Time Step	2.70×10^{-6} sec
Ballast Material Density	2.65×10^{3} kg/m^3

In this study, the 5% total axial strain (30.5 mm) was reached after 500 incremental displacement stages. At each stage, the top platen moved by 6.096×10-4 mm and then the simulation was continued while the whole system was re-equilibrated before the next incremental displacement was applied. The "incremental displacement" shearing method can reduce the CPU time for each triaxial test simulation, given that the host computer is a typical desktop PC, to around 30 hours (which generates significant savings in computational resources). To perform the same experiment in laboratory, it would take at least one business day and two technicians to prepare and perform the test, including the following tasks: sieving ballast material, engineering gradation, mixing testing materials, preparing the test specimen, assembling test setup, and operating test equipment.

Figure 4.10 shows the particle arrangement in DEM at different stages of the strength test and Figure 4.11 illustrates the bulging of the laboratory test specimen and the prediction of the DEM simulation at 10 percent strain. Figure 4.12 presents the results of the DEM simulations obtained using the "incremental displacement" shearing method and compares them with the test results from the experimental study. It is clear that DEM predictions obtained from IDSM match closely with the experimental results. Applying quasi-static loading schemes instead of quick loading in the DEM simulations could still capture the same deformation trends from the actual test sample loaded under rapid shear conditions in the laboratory. This implies the loading rate has insignificant effect on ballast strength measured and DEM can reproduce these inherent characteristics. Figure 4.13 presents the stress paths traced in the laboratory tests with both rapid and slow shear strain rate and the corresponding DEM simulation predictions from the "incremental displacement" shearing method and the continuous shearing method with slow shear strain rate. The friction angles, which are calculated from the peak deviator stresses for each test, are given in Table 4.3. It is clear that the friction angles decrease when the confining pressure increases in the laboratory tests, and DEM simulations captured this trend. The calculated friction angles from DEM simulation predictions are reasonably similar with the values calculated from the laboratory test results. A friction angle of 42 degrees was obtained based on the envelope of the stress path as showed in Figure 4.13.

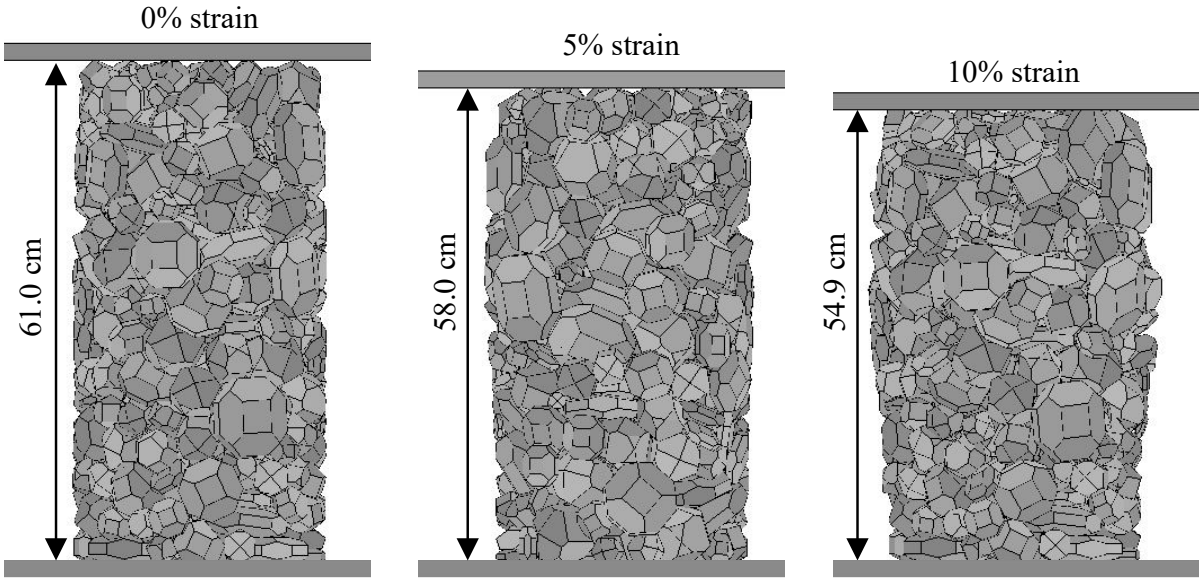

Figure 4.10. DEM Simulation of Ballast Sample Shown at Different Axial Strains

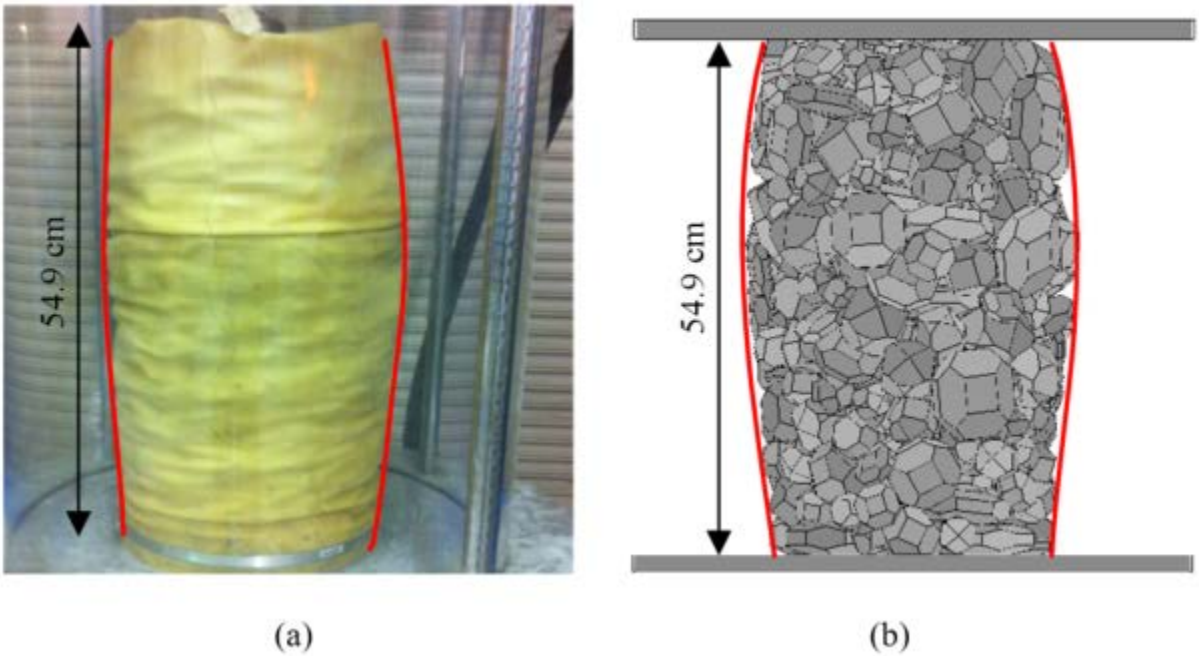

Figure 4.11. Deformed Ballast Sample Configuration with 69 kPa Confining Pressure; (a) Laboratory Test (b) DEM Simulation

Table 4.3. Calculated Friction Angles from Laboratory Tests and DEM Simulations

Confining Pressure (kPa)	Friction Angle (degree)			
	Laboratory Test		DEM Simulation	
	Rapid Shear	Slow Shear	IDSM	Continuous
68.9	44	45	43	43
103.3	43	44	42	42
137.8	41	40	41	40
206.7	40	--	40	39

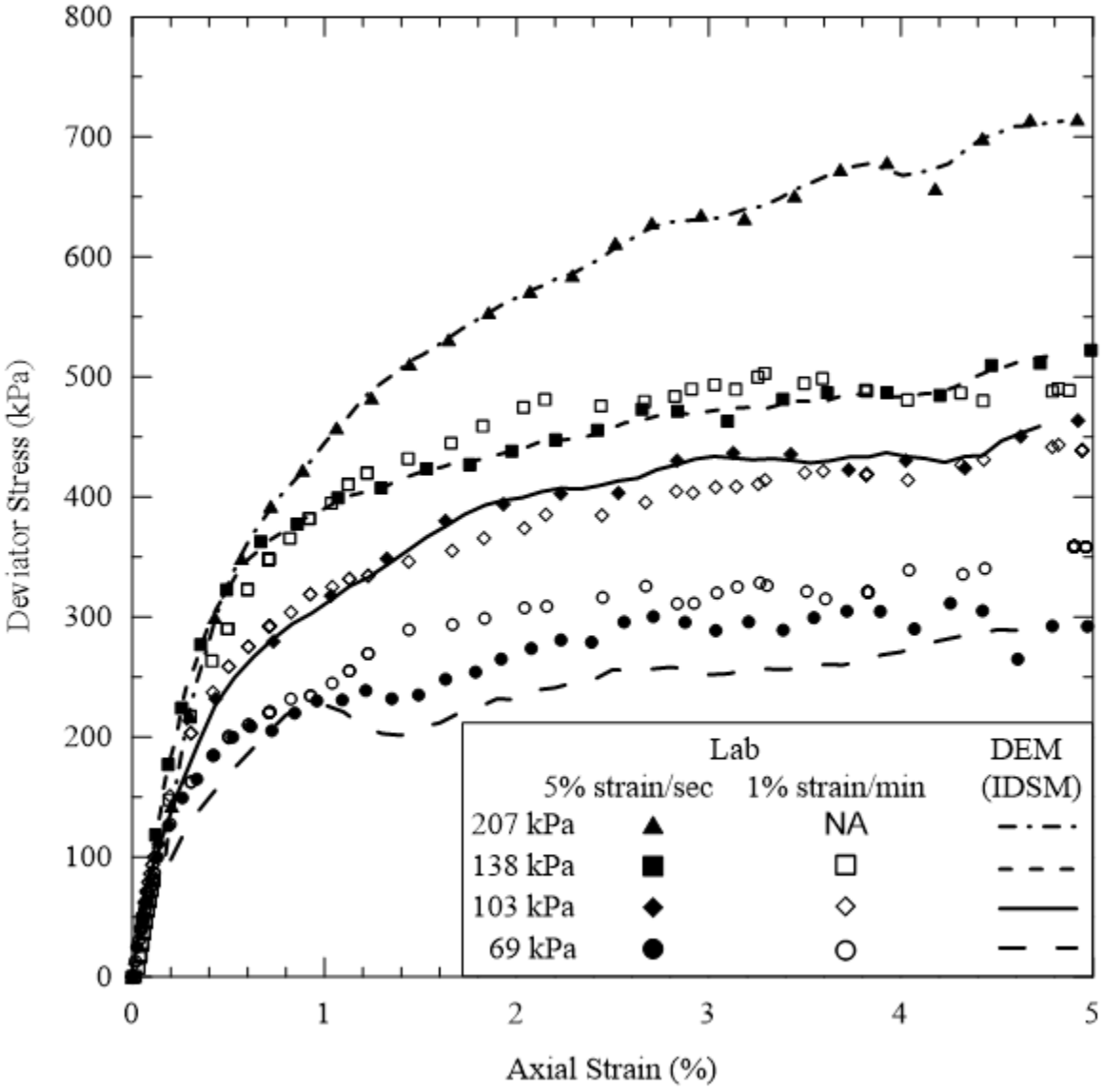

Figure 4.12. Comparison of DEM Predictions and Triaxial Compression Test Results

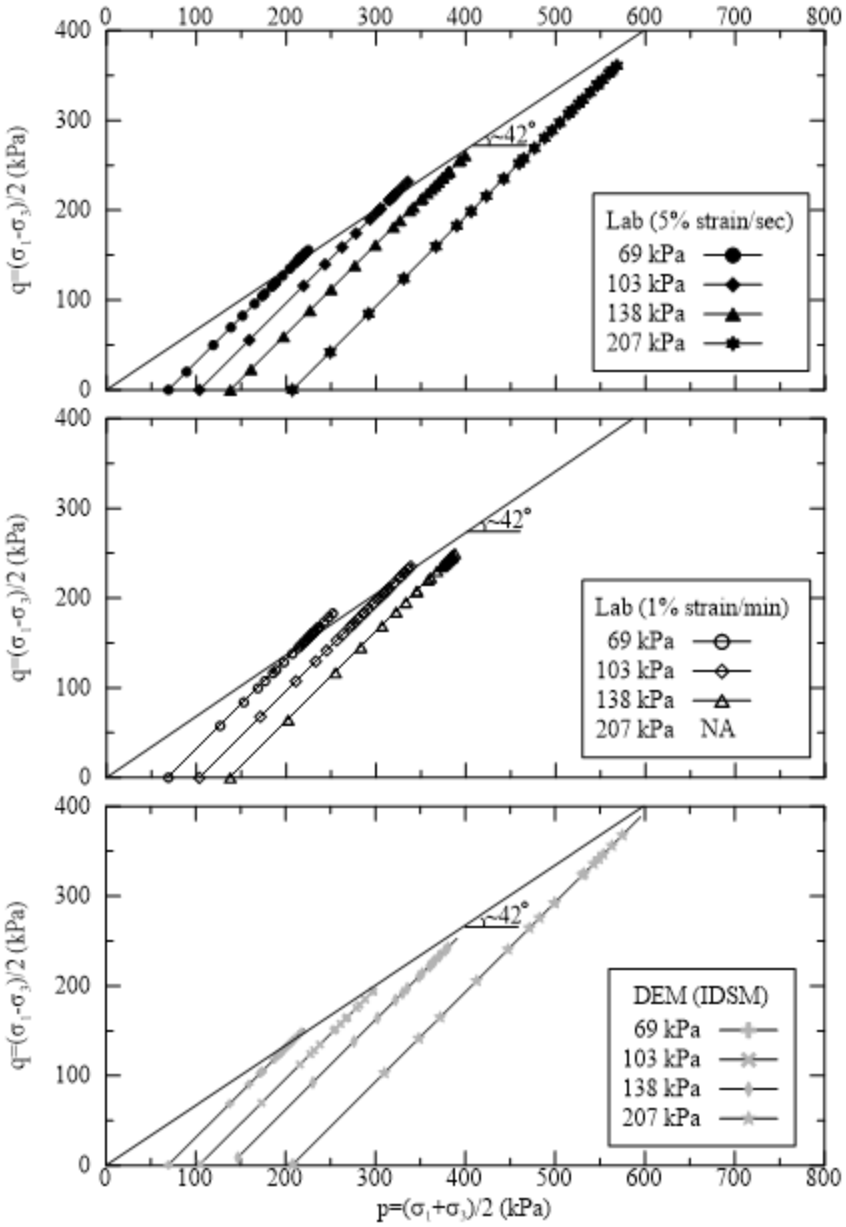

Figure 4.13. Stress Paths of Triaxial Rapid Shear Compression Tests and DEM Simulations

Importance of Initial Configuration

Due to the particulate nature of ballast aggregates, each particle is in different shape and size. In field conditions and laboratory experiments, the ballast particles have been randomly arranged, which leads to random initial configurations of ballast. For a given amount of ballast aggregates used in the laboratory, the initial configuration of ballast particle assembly also varies from one specimen to the other. However, it is difficult to study the effect of initial configurations in the laboratory because it requires an extensive amount of human power, time and equipment.

The DEM simulations in this study generated ballast particles randomly, according to the gradation and the shape libraries defined, so the initial configuration was also different from one simulation to another, similar to the conditions of laboratory specimens tested. However, the effect of initial configuration variation has not been investigated thoroughly yet. As discussed earlier, the DEM simulation with continuous shearing method took up to 15 days to complete one single simulation, which was not practical to repeat for several DEM simulations to study the effect of initial configurations. Accordingly, the "incremental displacement" shearing method, which was used in this study significantly reduced the CPU time to around 30 hours to complete each triaxial test simulation. This is a significant saving in computational resources and giving more time to investigate the impact of initial configurations with the limited resources available.

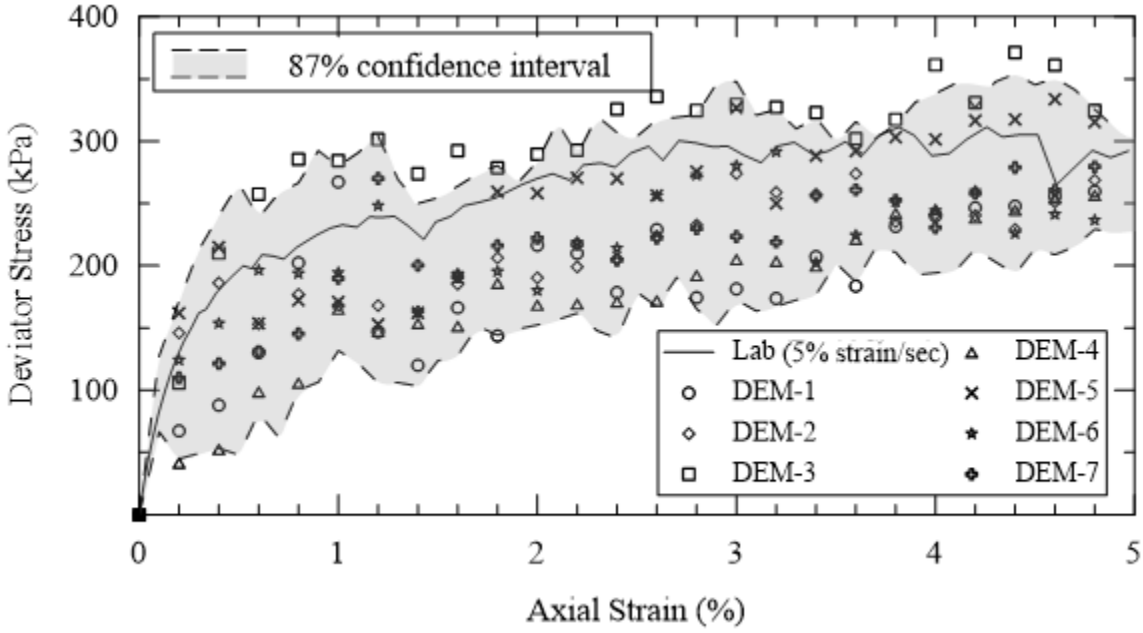

Figure 4.14. DEM Simulation Results from Seven Different Initial Conditions at 69 kPa Confining Pressure

Figure 4.14 compares DEM simulation predictions from seven different initial configurations with the "incremental displacement" shearing method with laboratory results obtained from the single rapid shear tests. Each simulation had exactly the same conditions except the initial particle arrangement, which was randomly generated to mimic real-life situations. This implies the principal source of the deviations from the experimental measurements originate in the initial configuration. The DEM simulation predictions indicate that the different initial configurations yielded different stress-strain curves. In Figure 4.15 compares laboratory results and the average values from different numbers of DEM simulations (average values of simulations with three, five and seven different initial configurations, respectively). It is clear that the discrepancy caused by different initial configurations can be successfully reduced by taking the average values of several DEM predictions. Thus, a minimum of three repetitions is required.

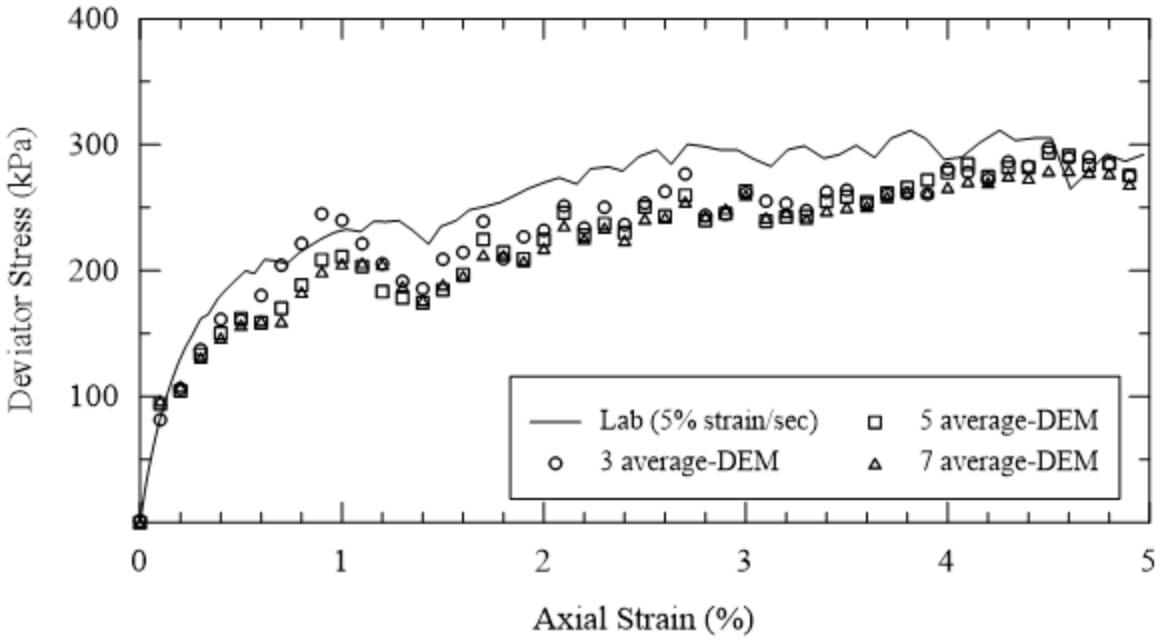

Figure 4.15. Averaged DEM Simulation Results from Different Initial Conditions at 69 kPa Confining Pressure

4.2.2 Simulation of Clean Ballast Permanent Deformation Tests

Simulating Repeated Loading by IDSM

The permanent deformation test is conducted with repeated loading and takes much duration to complete in the laboratory than the monotonic loading strength test, and similarly, the DEM simulation is longer. However, a sufficient number of loading cycles manageable in the simulation within a limited time can help predict field ballast settlement trends after many load applications often associated with hundreds of million gross tons of freight usage (Tutumluer et al., 2013). It would be best to apply the same repeated loading patterns that were applied inside the laboratory to the DEM simulation, especially a realistic moving train loading profile that has been derived from the dynamic track model that was previously presented.

In triaxial tests, a continuous sinusoidal load pulse is applied on the ballast samples and the permanent deformation behavior or ballast settlement is evaluated at different frequencies to represent different train speeds. This approach is often deemed sufficient since in-situ measurements indicate that greater ballast settlement is observed as the train speed increases, say from 150 km/h to 300 km/h as in the study by Hu and Kempfert (1999). DEM-related modeling research has focused on conducting numerical simulations of the tested samples as aggregate particle assemblies to investigate ballast behavior under continuous cyclic loading patterns (Indraratna, B., Thakur, P. K., and Vinod, J. S., 2010) (Lu, M., and McDowell, G. R., 2010). The actual dynamic loading, as opposed to a continuous sinusoidal load pulse often applied in cyclic triaxial tests, may have different loading patterns of varying pulse shapes with rest periods according to axle spacing and car length. These pulse shapes could directly affect the vibration

and deformation trends caused by a moving train at low, intermediate and high speeds (Huang, H., Shen, S., and Tutumluer, E., 2010).

In the laboratory test results of large scale triaxial strength tests, the shear strength was shown in previous section to be insensitive to the shearing rate. This is why incremental displacement method can be used to simulate the strength tests. Hicks stated that loading frequency was not an important factor in the permanent deformation behavior of ballast materials (Hicks, R. G., 1970). In Shenton, a series of cyclic loading tests were conducted on ballast specimens at various loading frequencies from 0.1 to 30 Hz with loading amplitude, confining pressure, and other test conditions remaining the same (Shenton, M. J., 1975). The paper concluded that the frequency of cyclic loading did not affect the ballast permanent deformation behavior significantly. A large permanent deformation observed in the field is explained by a higher dynamic force that is associated with increasing speed. The high loading amplitude instead of high loading frequency is the main reason to cause high permanent deformation (Shenton, M. J., 1975). Therefore, the permanent deformation behavior of ballast is also not sensitive to loading rate. It is possible that the incremental displacement method can be used to simulate the repeated loading test.

In strength tests, the target strain level is commonly established. In repeated loading tests, however, the target stress is given by the form of applied loading pattern and the resulting permanent strain level is unknown. Thus, in order to simulate the loading pattern in DEM, the top platen was first allowed to move downward by 6.096×10^{-4} mm and then, the simulation was continued while the whole system was re-equilibrated and checked if the stress on top of the specimen reached target stress level (165 kPa in this study) or not. If the stress applied on top of the specimen was less than the target stress, the top platen would be allowed to move downward by another 6.096×10^{-4} mm and provided the system to re-equilibrate. This way, the top platen kept moving downward step by step until the target stress was reached. After the target stress was reached, the top platen would be allowed to move upward by 6.096×10^{-4} mm and then, the simulation was continued until the whole system was re-equilibrated. The top platen was moved upward step by step to simulate the unload stage of the repeated loading as well. The movement of top platen in each incremental step should be sufficiently lesser and it was determined to be 6.096×10^{-4} mm (same as the strength test simulation) to avoid increasing or decreasing pressure too rapidly on the top platen by a single movement. Figure 4.16 presents' stress-strain curves of the first 10 loading cycles from the laboratory experiment and the DEM simulation, respectively.

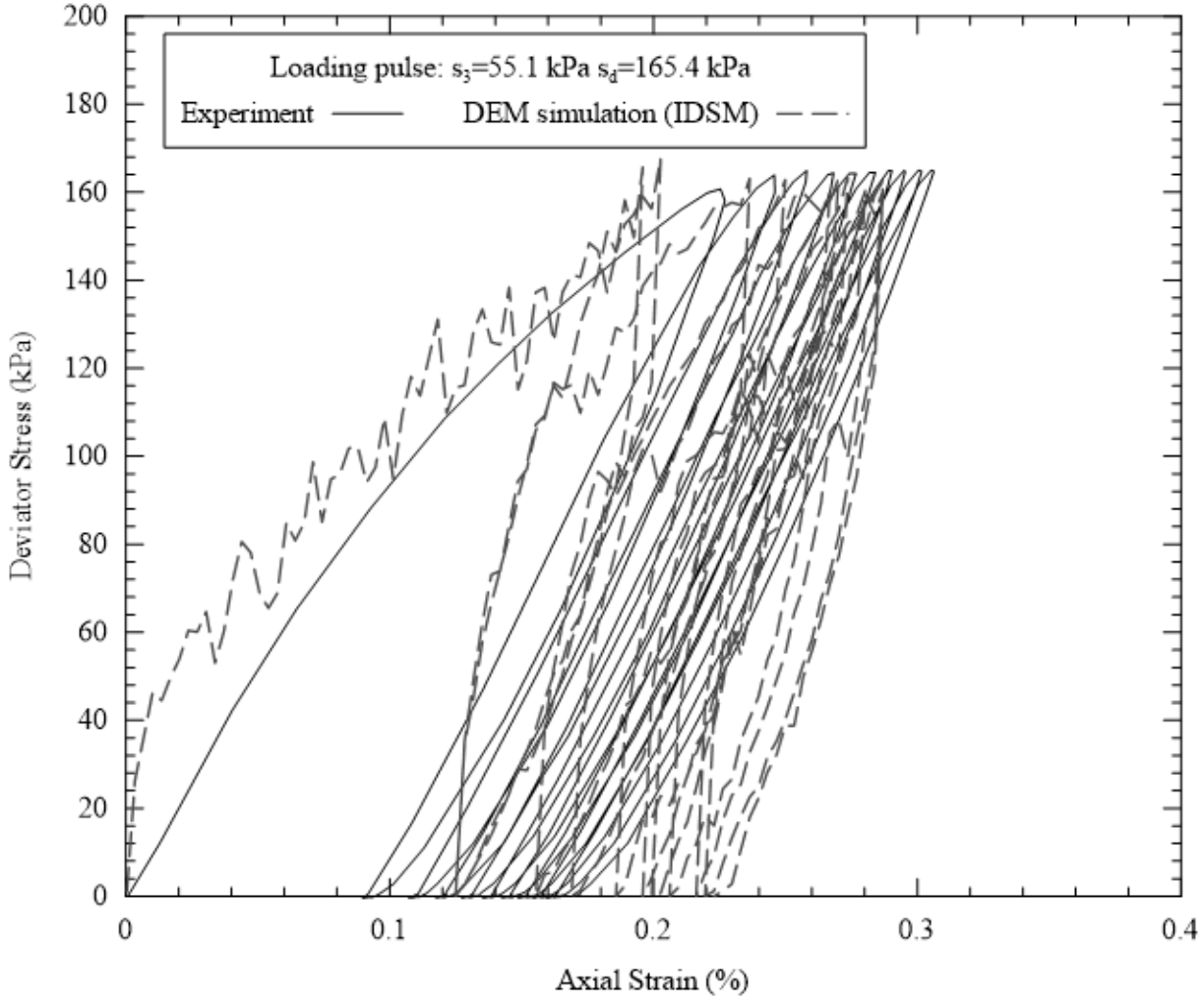

Figure 4.16. Comparison of Loading Cycles Used in Experimental Study and DEM Simulation with IDSM *(Incremental Displacement Shearing Method*)

Importance of Compaction in DEM Simulations

After successfully simulating the large scale triaxial strength test with a flexible membrane assembled by rigid rectangular cuboid discrete elements and polyhedron particles, the same technique was adopted to simulate the large scale triaxial permanent deformation tests (Hashash et al., 2012). After the membrane was formed, ballast particles were poured into the cylinder and the top platen was placed on top of the specimen. In this way, around 500 particles were used to fill in the chamber. The specimen was compacted in the DEM simulation with cyclic loading similar to the specimen compaction in the laboratory experiment. However, by selecting appropriate height to let particles fall down under gravity, the specimen able to achieve the required density. Thus, it is necessary to investigate further to determine whether the compaction in DEM simulation is necessary.

Brown and Thom concluded that permanent strain depended on compaction besides gradation (Brown, S. F., and Thom, N. H., 1988). Dawson et al. explained the loading history effect was a

result of the specimen gradually stiffening after each cycle of loading and that was the reason the permanent deformation accumulated in decreasing rate (Dawson, A., Isacsson, U., and Lekarp, F., 2000). Diyaljee investigated the stress history effect on ballast behavior through laboratory cyclic loading tests and concluded that the plastic strain would significantly decrease if the specimen experienced more than 50 percent of the current applied deviator stress in the previous stress history (Diyaljee, V. A., 1987).

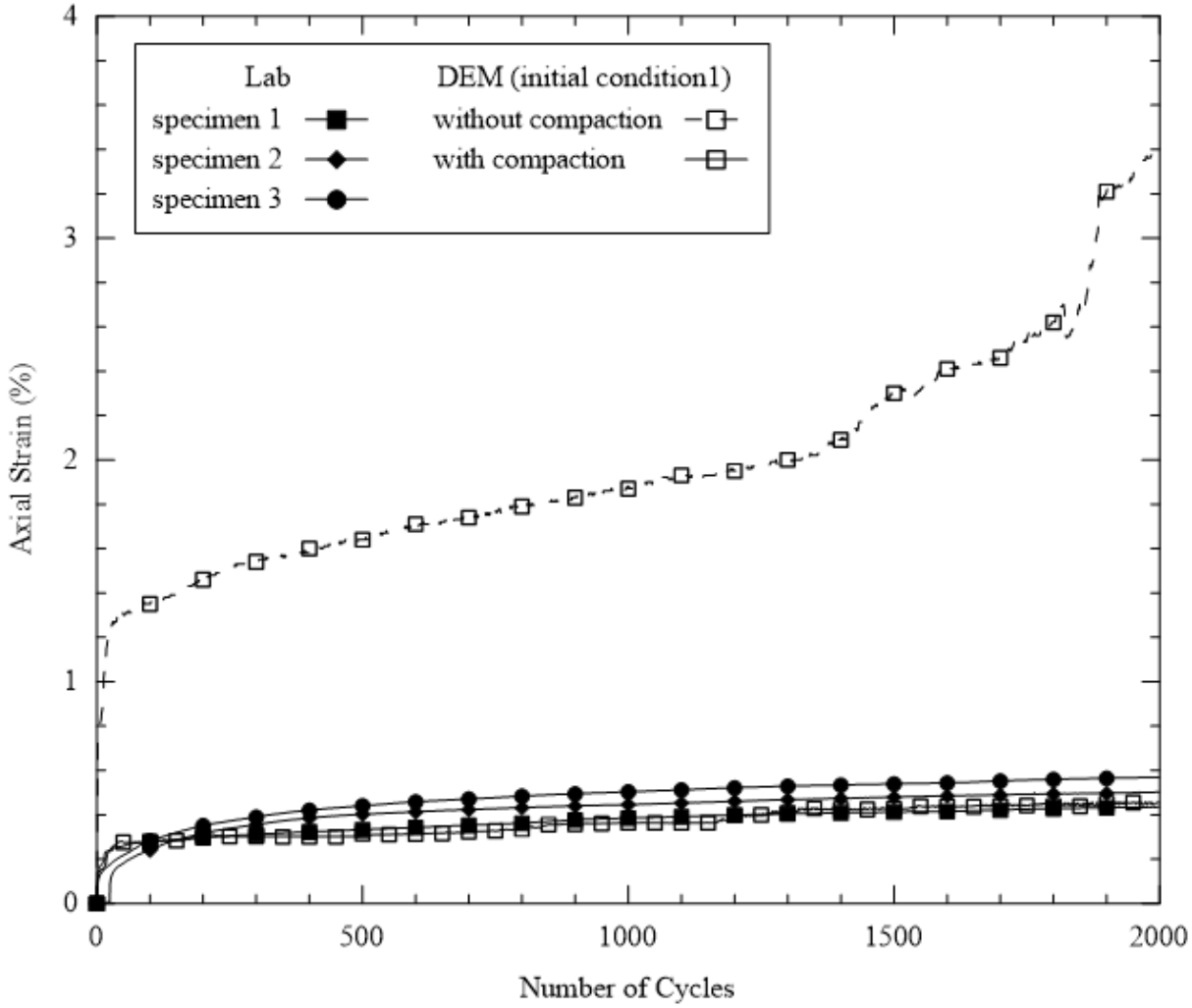

Figure 4.17. Comparison of DEM Predictions with or Without Compaction and Triaxial Permanent Deformation Test Results

To investigate the importance of compaction or stress history effects in DEM modeling, two simulations were performed with exactly the same initial configuration (denoted as "initial condition 1"), while the only difference was that the first simulation experienced repeated loading without compaction after achieving the target density by free falling and the second simulation was compacted for approximately 16 seconds (same as laboratory condition) even if the target density was achieved by free falling particles. Due to the high computational expense, the two simulations were conducted only up to 2,000 loading cycles as shown in Figure 4.17. Compared with the laboratory experimental results, the two simulations with and without compaction phase resulted in reasonably predicted trends of permanent deformation

accumulation. The DEM simulation with compaction predicted reasonable permanent axial strain values when compared to the experimental results. However, the DEM simulation without compaction yielded much higher permanent axial strains, although the density was similar (as shown in Table 4.4). Both the experimental results and DEM predictions clearly indicated that the permanent deformation primarily accumulated in the initial dozens of loading cycles and then increased with a relatively stable rate, and this rate was similar for all the DEM predictions and experimental results (which also validated the DEM simulation). The DEM simulation with compaction yielded much less permanent axial strain as compared with the DEM simulation without compaction. However, most of the differential strain happened in the initial loading cycles. Earlier research studies shown similar trends in laboratory experiments and confirmed compaction aided to increase the resilient modulus of granular materials (Hicks, R. G. and Monismith, C. L., 1971) (Selig, E. T., and Waters, J. M., 1994). Indraratna et al. also indicated that critical stage of ballast service life occurred immediately after the track construction or maintenance, when ballast was in less compacted state (Indraratna, B., Ionescu, D., and Christie, H. D., 1998).

Table 4.4. Void Ratios of DEM Simulation Samples Before and After Compaction

	Void Ratio	
Experiment	0.68	
DEM (IDSM)	before compaction	after compaction
initial condition 1	0.682	0.679
initial condition 2	0.678	0.677
initial condition 3	0.679	0.675

The two simulations agreed with previous research efforts and have confirmed that compaction is indeed very important (Hicks, R. G. and Monismith, C. L., 1971) (Selig, E. T., and Waters, J. M., 1994) (Indraratna, B., Ionescu, D., and Christie, H. D., 1998). In some cases when compaction does not increase density significantly, it still impacts the particle packing structure. The test specimens will yield less permanent strain with appropriate compaction because better particle packing is achieved during initial compaction. However, this compaction effect will mainly affect the initial permanent strain under repeated loading. Upon increasing the number of loading cycles, the rate of permanent strain accumulation decreases and becomes stable after a certain number of load cycles. The compaction effect becomes less pronounced when relatively stable particle packing arrangement is gradually achieved with an increase in the number of load cycles, and the rate of permanent strain accumulation becomes similar for both the compacted and uncompacted specimens. This is because initial particle arrangement has a significant influence on initial permanent strain accumulation rate, but when a relatively stable particle arrangement is achieved, the permanent strain accumulation rate is governed by material properties, such as gradation, angularity, F&E ratio, surface texture, and fill material.

Source of Permanent Deformation

Ballast permanent deformation or settlement can come from many sources, such as particle rearrangement, abrasion, particle breakage, densification, etc. To check the ballast breakage

condition, sieve analysis was performed before and after the permanent deformation tests in the laboratory and no significant gradation change was found. Table 4.5 lists the changes in gradation of ballast material in the experimental study. It is interesting to note that the difference between the gradations before and after the test is insignificantly. In other words, the ballast particles in this study did not experience noticeable breakage under the repeated loading used, and particle breakage was not the main reason to cause permanent deformation in this studied.

Table 4.5. Limestone Gradation Check After 10,000 Cycles on Permanent Deformation Test

	Percentage Retained (%)	
Sieve size (mm)	Before test	After test
63.5	1.01	0.97
50.8	5.49	4.59
38.1	51.98	52.92
25.4	38.45	38.72
12.7	3.06	2.80
Pan	0.0	0.0

DEM Simulation Results of Permanent Deformation Tests

By adopting the "incremental displacement" shearing method in DEM computations, it is possible to simulate many more loading cycles and reduced CPU computational requirement. Three DEM predictions of permanent strain with different initial configurations up to 2,000 loading cycles are given in Figure 4.18. Table 4.4 lists the corresponding void ratios for each initial condition before and after compaction, and experimental results are also presented to compare with the DEM simulation results. Following the same procedure for specimen preparation in laboratory experiments, the DEM simulations captured the permanent strain accumulation trends and magnitudes. With different initial configurations, the magnitude for different laboratory tests or DEM simulations can vary but within a limited range. All the experimental results and DEM predictions showed that the permanent axial strain increased in a decreasing rate. Firstly, the permanent strains rapidly accumulated and then increased gradually when a relatively stable ballast deformation condition was reached. In order appropriately consider the effects of different initial configurations, the average response of permanent strain were also evaluated as shown in Figure 4.18. The DEM simulations, which predicted permanent deformations for up to 2,000 loading cycles, are reasonably accurate when considering the 1 percent of the axial strain is only 6 mm while the particle sizes could be as large as 60 mm. The sudden increase in DEM simulation with initial configuration #2 was actually only about 1 mm, considering the specimen height was 610 mm. However, this type of deviation will be averaged out if more simulations are performed to reduce the initial configuration effect.

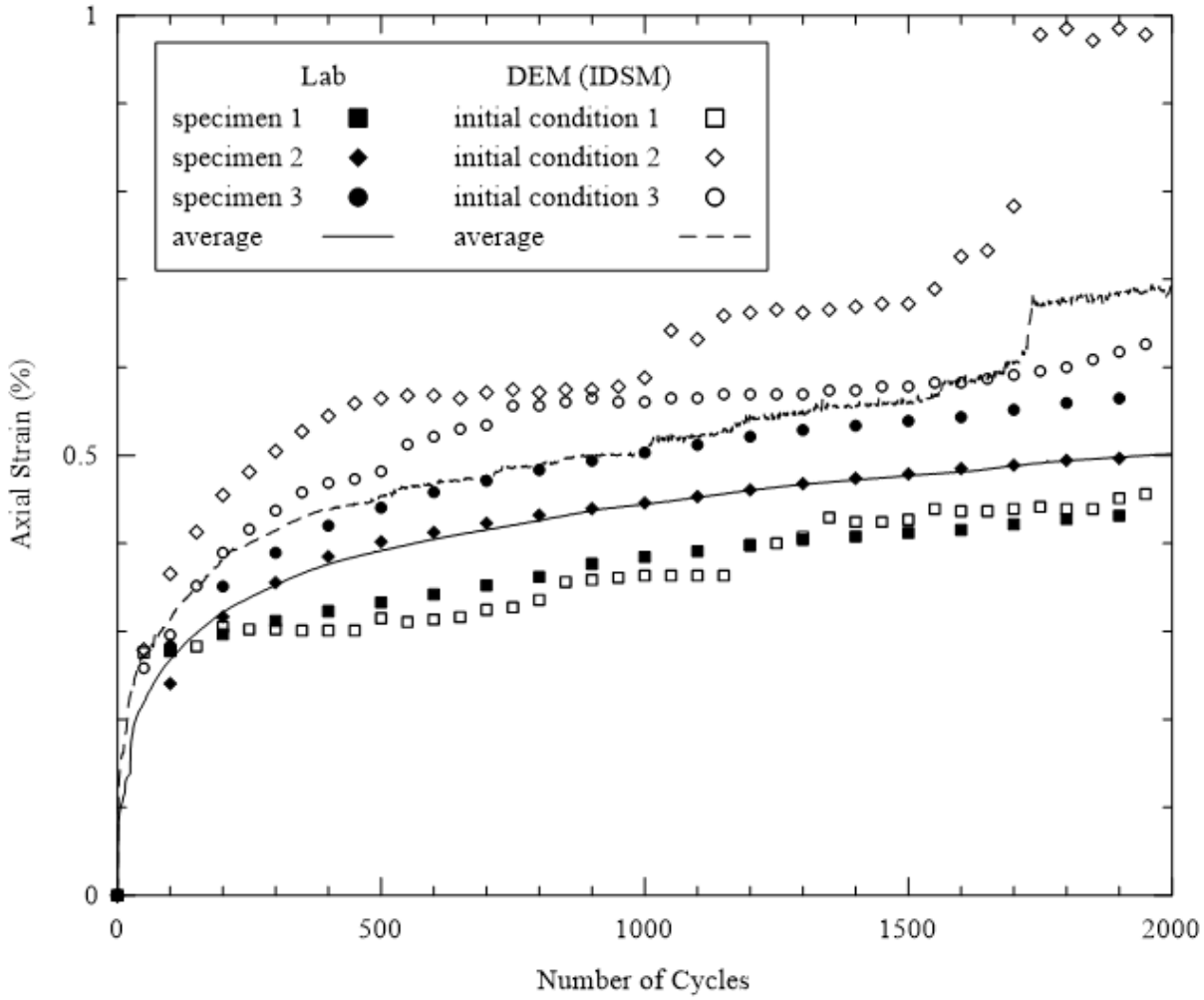

Figure 4.18. Comparison of DEM Predictions and Triaxial Permanent Deformation Test Results up to 2,000 Cycles

In Figure 4.19 presents detailed laboratory results of the permanent strain accumulating with number of load applications for the first 100 cycles of repeated loading. The experimental data clearly shows that the permanent strain did not accumulate evenly with the increasing load cycles. Relatively "large" strain levels can accumulate very quickly within few cycles. This is probably because of sudden particle reorientation, rearrangement, or abrasion. Note the DEM code used in this study, BLOKS3D, employed true polyhedron but rigid particles, thus, the similar sudden permanent strain accumulation behavior was also captured by the DEM simulations as indicated in Figure 4.19. In summary, at relatively small stress levels, particle breakage may not be the main reason that contributing to permanent deformation of ballast test specimens. Particle reorientation, rearrangement, and abrasion may cause sudden permanent strain accumulation.

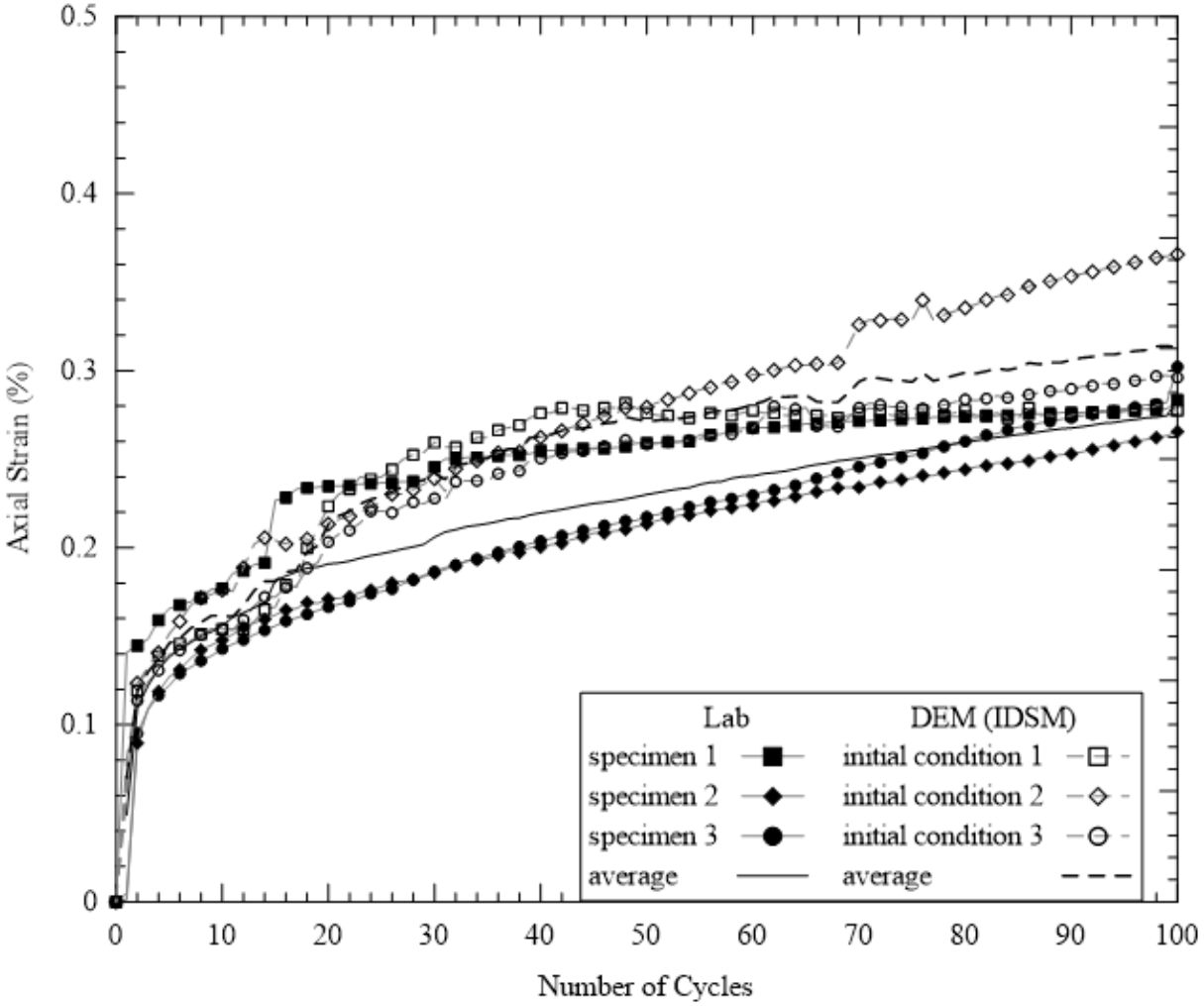

Figure 4.19. Comparison of DEM Predictions and Triaxial Permanent Deformation Test Results for the First 100 Cycles

5. Characterization of Ballast Degradation with LA Abrasion test

5.1 Introduction to Ballast Fouling

As ballast ages, it is progressively fouled. Fouling refers to the condition of railroad ballast when voids in the unbound aggregate layer are filled with relatively finer materials, such as fouling agents commonly found in the ballast aggregate breakdown, outside contamination such as coal dust from coal trains, and materials from subgrade soil intrusion. Ballast fouling or degradation is associated with railroad track performance are very concerning, such as poor drainage, rapid and excessive settlement and reduced lateral strength. It is considered unfavorable and routinely dealt with by cleaning ballast and performing undercutting-type track maintenance. According to previous research studies, the main cause of ballast fouling is the degradation and breakdown of uniformly-graded large ballast particles under repeated traffic loading (Boucher, D. L., and Selig, E. T., 1990). Selig and Waters concluded that up to 76 percent of the ballast fouling was due to ballast breakdown, in other words, ballast self-degradation (Selig, E. T., and Waters, J. M., 1994).

To quantify ballast fouling conditions, Selig and Waters proposed two indices (Selig, E. T., and Waters, J. M., 1994): (i) Fouling Index (FI), and (ii) Percentage Fouling. FI is the summation of percentage by weight of ballast sample passing the 4.75 mm (No. 4) sieve and the percentage passing the 0.075 mm (No. 200) sieve. Percentage fouling is the ratio of the dry weight of material passing the 9.5 mm (3/8 in.) sieve to the dry weight of the total sample. In the context of this report section, fine materials are those with particle sizes smaller than 9.5 mm or passing 3/8-in. sieve. Significantly higher ballast settlements were reported when the amount of outside fouling material in ballast increased (Han, X., and Selig, E. T., 1996) (Huang, H., Dombrow, W., and Tutumluer, E., 2009) (Indraratna et al., 2012).

Although it is important to better understand the effects of such fouling agents that causes track degradation. A large portion of the railway track system's annual operating budget goes toward the maintenance and renewal of ballast, which is fouled in 76 percent of the cases due to ballast breakdown or self-degradation (Selig, E. T., and Waters, J. M., 1994).

In previous studies, several laboratory tests were proposed to generate fouled ballast with ballast degradation, such as the Los Angeles (LA) abrasion test, the mill abrasion test, the Deval abrasion test, and the Micro-Deval abrasion test. Different test methods showed good correlation with different materials and test conditions.

The LA abrasion test was found to correlate well with actual material breakdown, especially ballast breakdown in large-scale triaxial tests under dry test conditions (Lim, W. L., 2004) (Armitage et al., 2005) (Aursudkij, B., 2005) (Horvli, I., Noålsund, R., and Tutumluer, E., 2013). To better understand ballast performance associated with its usage and life cycle degradation due to particle abrasion and breakage, a series of LA abrasion tests were performed in the controlled laboratory environment to break down a commonly used granite ballast material and limestone type ballast aggregate. The experimental work undertaken in this research study revealed quite important linkages between ballast fouling and degradation trends quantified by imaging based characterization of particle size and shape properties.

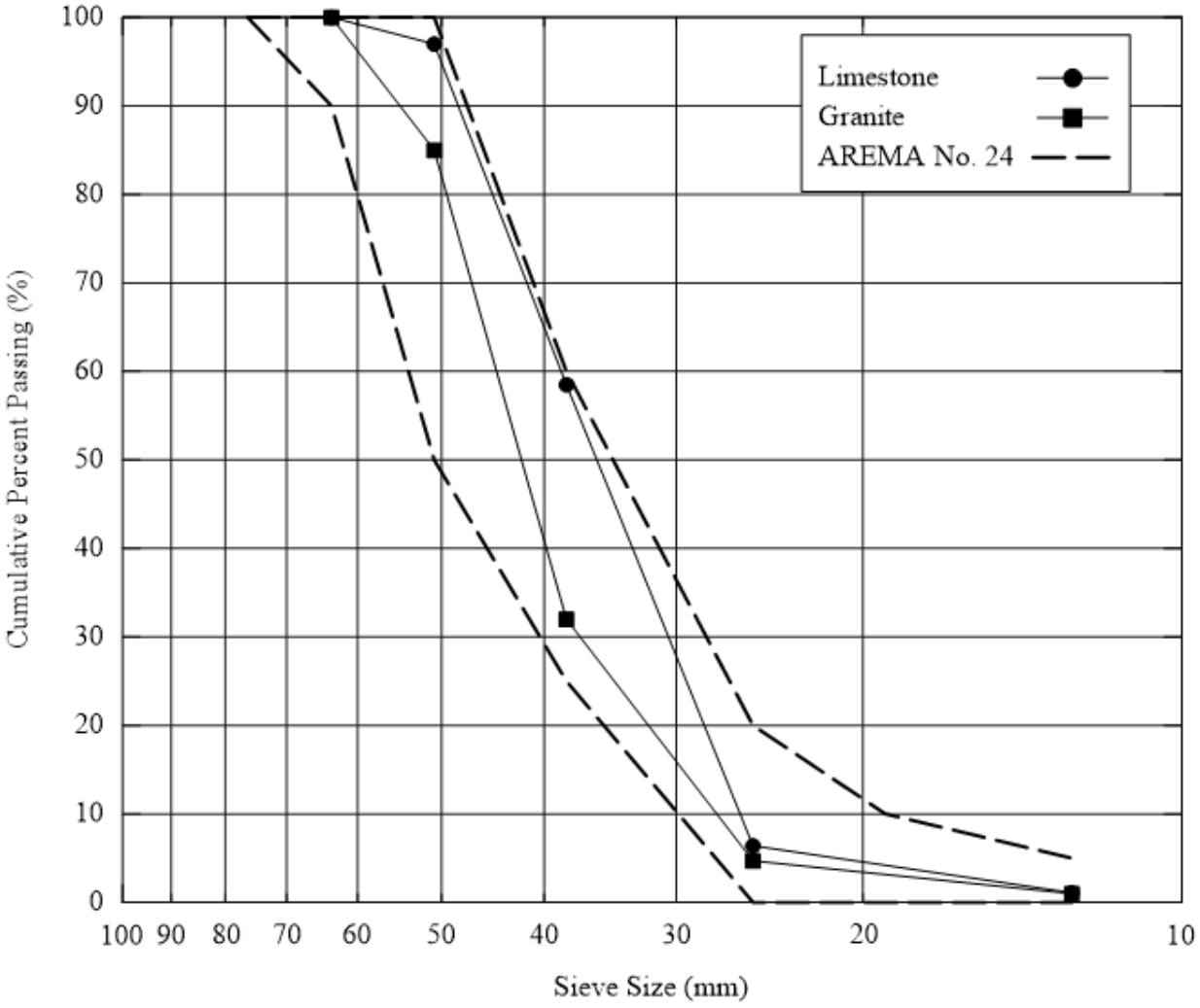

Figure 5.1. Gradation Properties of Ballast Material Used in LA Abrasion Test

5.2 Generating Fouled Ballast Materials in the Laboratory

The ballast materials studied in the laboratory were 100 percent crushed limestone and granite aggregate, which adequately met AREMA No. 24 gradation requirements as shown in Figure 5.1. The test procedure involved placing 10 kilograms of new ballast material in the LA abrasion drum together with 12 steel balls (see Figure 5.2). The drum was set to rotate on the average at 50 turns per minute and for each run the drum rotated 125 times for limestone and 250 times for granite specimens to evaluate degradation trends step by step in a controlled laboratory study. After finishing each test, the drum was allowed to stand still for about 10 minutes to let dust settle down before the tested material was poured out. In order to minimize loss of fine materials, both inside the drum and steel balls were carefully hand brushed after each test. All particles above 25.4 mm or 1.0 in. sieve were also brushed to collect dust and fine material before sieving. The rest of the degraded materials that passing through the 25.4 mm/1.0 in. sieve were carefully sieved using a DuraShake™ type rotation aggregate sifter so that loss of fine materials was minimized. Materials passing each sieve size were then collected and placed on a blue tarp placed on the floor to take high resolution photographs. In addition, aggregate particles

larger than 9.5 mm or passing 3/8-in. sieve size were hand collected and capture for image analysis. In this step taken before all materials are mixed together for the next LA abrasion run need to determine the image-based quantifications of particle size and shape indices after each test. The outlined procedure was repeated until the specimen reached FI of 40, which corresponded to a heavily fouled ballast condition certainly requiring maintenance activities in the track. Note that the same specimen was always used in LA abrasion testing, which required several individual runs at 125/250-turn intervals of each of the LA drum. In order for granite to reach an exact FI of 40, an additional 125 turns of the drum was needed it to complete the test at 2,125 drum turns.

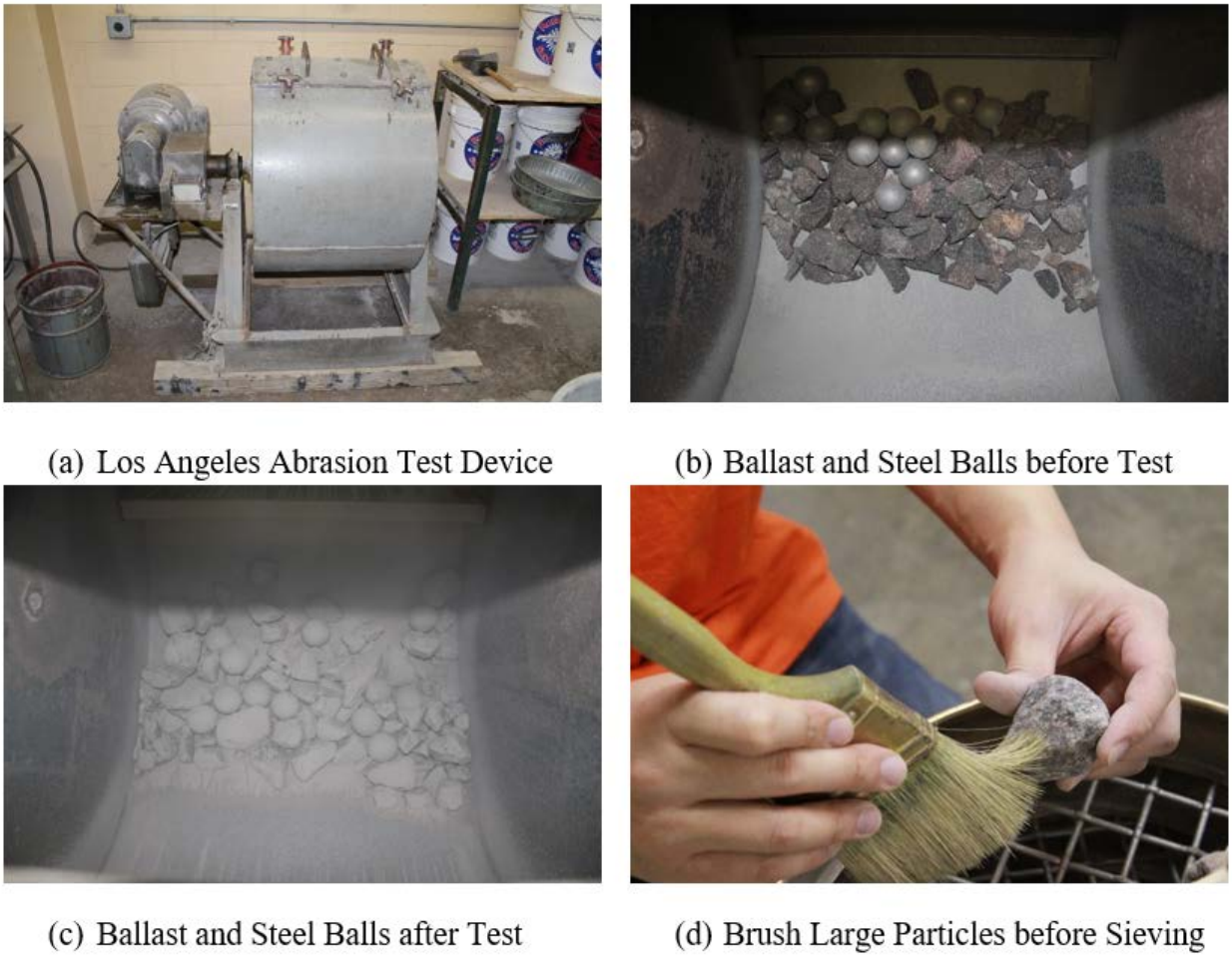

(a) Los Angeles Abrasion Test Device

(b) Ballast and Steel Balls before Test

(c) Ballast and Steel Balls after Test

(d) Brush Large Particles before Sieving

Figure 5.2. Photos Showing LA Abrasion Test Equipment and Specimen

5.3 Key Observations from LA Abrasion Test

In both Figure 5.3 and Figure 5.4 shown the limestone and granite specimen gradation curves obtained from the results of sieve analysis tests that were performed with 1,500 and 2,125 turns of the LA abrasion drum, respectively. These figures also present the FI values calculated for each gradation curve. As the number of turns increased in the LA abrasion tests, the ballast specimens changed gradually from "uniformly" graded to more "well" graded type of a material. This is also indicated by the rapidly increasing FI values corresponding to the first few LA

abrasion runs followed by a slower rate for each additional 125/250 turns as shown in Figure 5.3 and Figure 5.4. No doubt, the clean ballast material was more susceptible to the abrading sharp corners and edges of the crushed particles. Generally, breakage of the large sized particles occurred in the early stages of the experiment as well. With the number of turns increasing in LA abrasion runs, those particles that did not break due to the impact loads eventually became much more rounded due to the sharp corners chipping away and the surface abrasion smooth out the edge textures. The overall gradation variation trends generally agreed with previous research on field ballast degradation trends (Selig, E. T., and Waters, J. M., 1994).

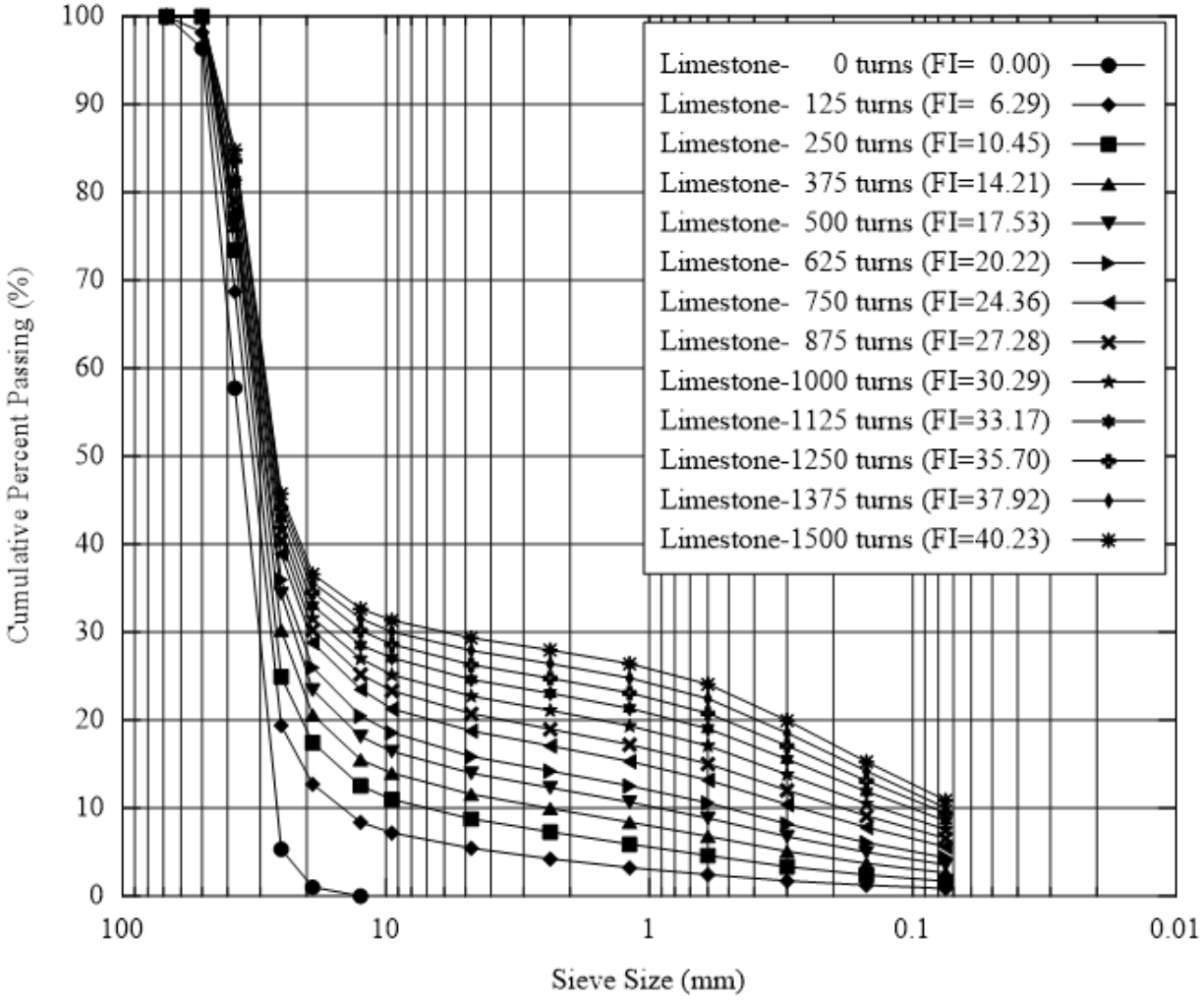

Figure 5.3. Gradation Change of Limestone During LA Abrasion Test

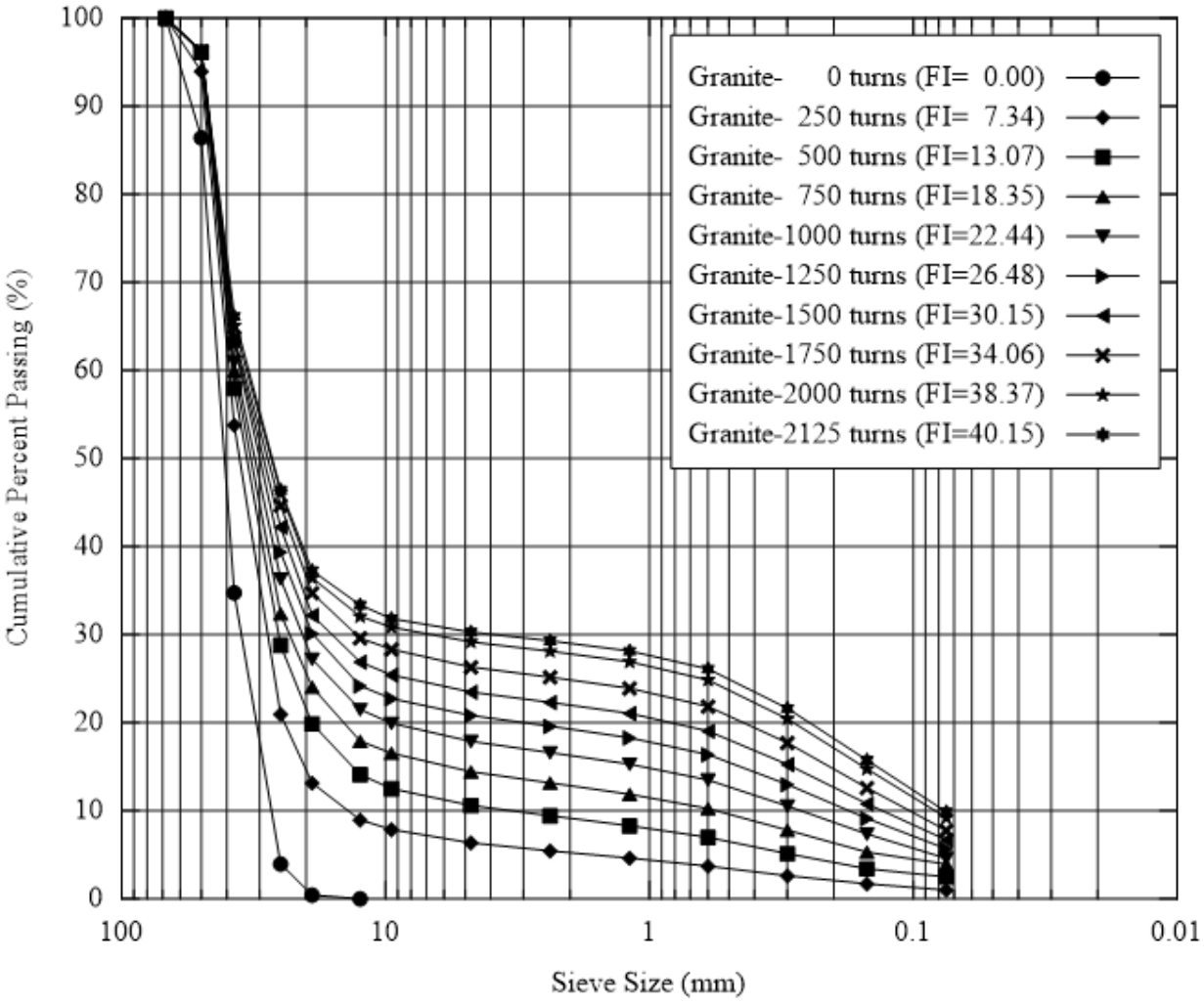

Figure 5.4. Gradation Change of Granite During LA Abrasion Test

The overall particle size degradation trends and the changes in proportion to the original particle sizes are visualized in Figure 5.5 (limestone up to 1,500 LA abrasion drum turns) and in Figure 5.6 (granite up to 2,125 LA abrasion drum turns). For the first 250 turns with granite, the specimen rapidly degraded from the original clean ballast, which had particle size distribution captured by only 5 sieve sizes, to fouled ballast with a condition FI value of 7 and gradation represented by many more sieve sizes. The initial abrasion and breakage of the large particles immediately produced both smaller particles as well as fine materials, i.e., particles less than 9.5 mm or passing 3/8-in. sieve size, as shown in Figure 5.6. In the case of the original clean ballast specimen, there were seven particles retained on the 50-mm sieve and 37 particles retained on the 37.5-mm sieve, respectively. After the granite received 2,125 LA abrasions drum turns, these particle counts decreased to 2 and 25 for particles retained on the 50 mm and 37.5 mm sieves, respectively. This means several of these particles were broken into smaller sizes. It is also interesting to note that for some sieve sizes, e.g., 12.5 mm, the number of particles generated throughout the experiment increased initially and decreased subsequently. In this case, additional particles were created as resulted from the larger sizes broken down and consequently

these 12.5-mm sized particles were again broken into more smaller sizes afterward when the number of drum turns further increased.

At the later stages of the experiment (as discussed earlier), FI increased with a decreasing rate, which implies that particles became not only smaller but also smoother and more rounded, which made them more resistant to abrasion and breakage. For example, Figure 5.6 provides visual evidence about how those particles retained on the 37.5-mm sieve indeed became smoother and rounded after 500 turns and did not break or change much the particle number count. Since no new particles were introduced from breaking the particles retained on the 50-mm sieve as shown in Figure 5.6. More detailed analyses of the degradation trends, including particle shape indices quantified from the image analysis approach, will confirm such changes in shape properties (which will be discussed later in this report).

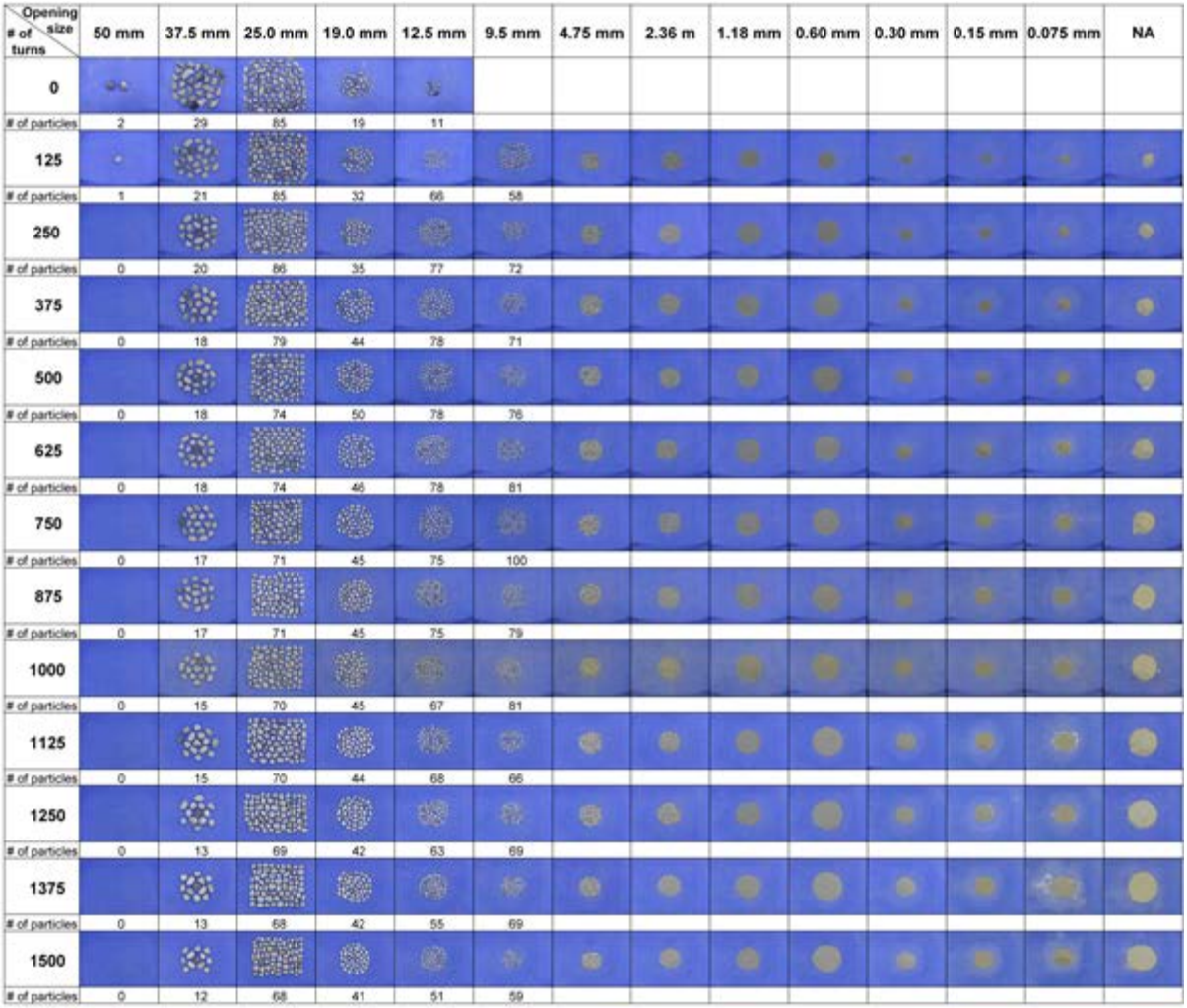

Figure 5.5. Photos of Limestone Particle Size Degradation Trends with LA Abrasion Drum Turns

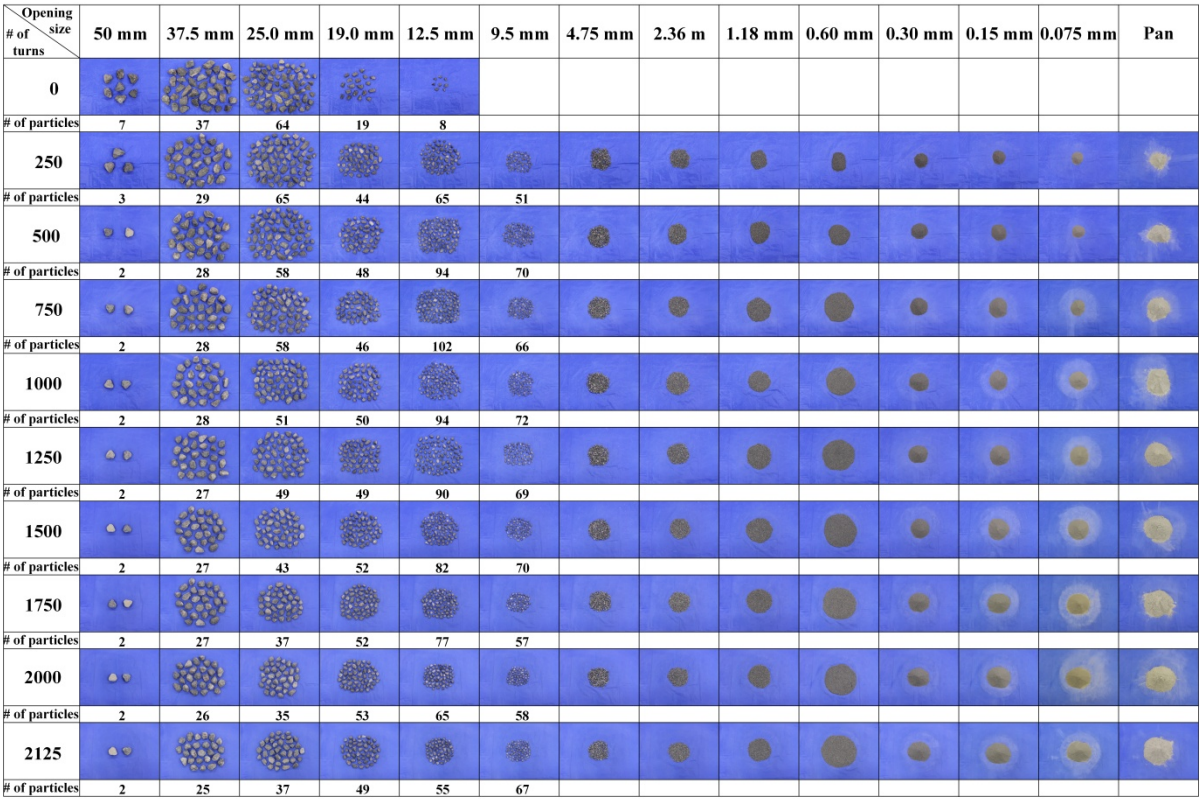

Figure 5.6. Photos of Granite Particle Size Degradation Trends with LA Abrasion Drum Turns

Gradation curves and visualizations of individual particle sizes at different LA abrasion turns provide valuable information about ballast aggregate compositions at different fouling levels. However, it is not obvious how to relate these degradation trends to the ballast layer's functional characteristics and the governing mechanisms that would impact field ballast layer structural and drainage behavior. A better basic understanding could be gained by visualizing how material would pack, how much void space would be left, and whether or not there would be individually contacting larger particles (i.e., a load carrying aggregate skeleton, left in ballast layer associated with different levels of fouling).

To investigate particle contact and particle packing characteristics, the test specimens collected after each 125/250 turns of LA abrasion run was poured into an acrylic chamber with dimensions of 25.4 cm (10.0 in.) in diameter and 25.4 cm (10.0 in.) in height. In both Figure 5.7 and Figure 5.8 presented the side and top views of aggregate packing photos taken at the different number of LA abrasion drum turns with the corresponding FI values. Due to the continuous abrasion and breakage of particles throughout the test, the total height of test specimens decreased substantially after 1,500/2,125 drum turns with less void space left among particles; one can easily visualize this phenomenon in Figure 5.7 and Figure 5.8. The fine materials accumulate from the bottom to fill all the voids created by now fewer large particles, all the way to the top when FI values of 40 are finally reached. This was suggested by Selig and Waters as the limit of fouled ballast, which indicates such heavily fouled ballast (FI=40) should no longer be used in the field (Selig, E. T., and Waters, J. M., 1994). The images also present the aggregate packing with and without fine materials, respectively.

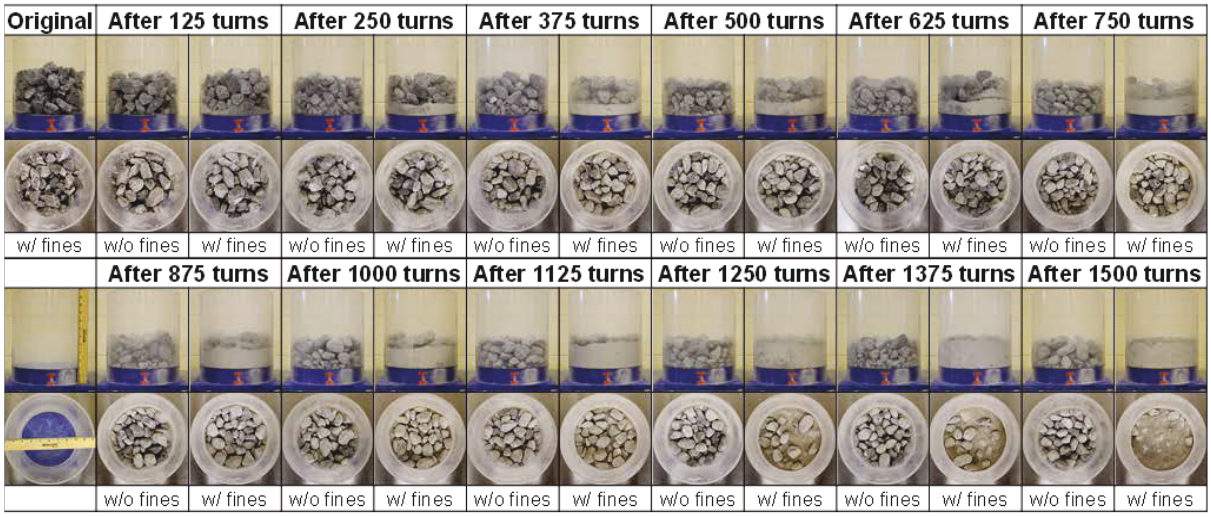

Figure 5.7. Side and Top Views of Plexiglas Cylinder Indicating Particle Packing of Limestone

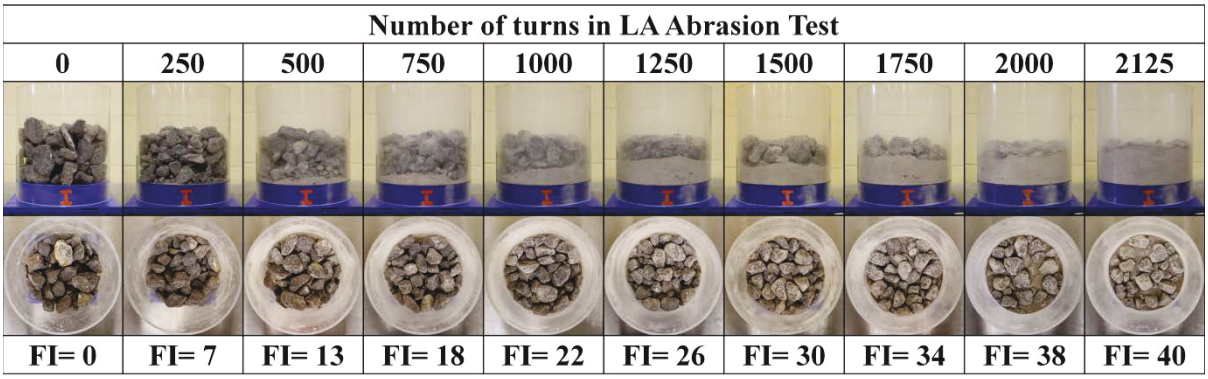

Figure 5.8. Side and Top Views of Plexiglas Cylinder Indicating Particle Packing of Granite

5.4 Image Analyses of Fouled Ballast Materials from LA Abrasion Tests

In Table 5.1 and Table 5.2 lists the average values of the imaging based F&E ratio, AI, and the ST index determined for particles retained on different sieve sizes above 9.5 mm or 3/8 in. for the limestone and granite after the appropriate number of drum turns. There are two clear and interesting trends can be observed as follow:

1. For a certain particle size, the shape properties, AI and ST index, commonly decrease as the number of drum turns increases (as shown in Table 5.1 and Table 5.2 from left to right). This trend, which is from the quantitative imaging based indices, confirms that the same particles tend to be smoother and more rounded after LA abrasion testing.
2. For a certain number of drum turns, the AI and ST indexes generally increase as particle size decreases as shown an individual columns from top to bottom in Table 5.1 and Table

5.2. Initially, smaller particles created from the breakage of larger particles have more crushed faces and thus they are more angular and rougher textured when compared to the larger particles that often experience abrasion only.

Also from both Table 5.1 and Table 5.2, the total number of particles above 9.5 mm (3/8 in.) initially increased from 146 or 135 to 308 or 302 rapidly and then decreased to 231 or 235 as FI values increased all the way up to 40 for limestone and granite, respectively. These quantified particle counts and imaging based shape indices clearly capture the primary degradation trend observed. The large particles were more likely to break in the beginning and as such, the smaller particles that were created quickly tended to become more resistant to abrasion and breakage later on. A recent field imaging study, which was focused on collecting and analyzing aggregate samples from various ballast depths in a mainline freight railroad track can be deploy successfully to detect the gradual decrease in the aggregate size along with ballast depth associated with higher rate of degradation and particle breakdown on top of the ballast layer and the increased AI and ST index values measured at greater depths (Ahuja et al., 2013).

In Figure 5.9 through Figure 5.14 presented the distributions of shape indices, AI, ST index, and F&E ratio for all the particles scanned by the Enhanced University of Illinois Aggregate Image Analyzer (E-UIAIA). Each value of an imaging based shape index was determined from scanning a particle after every $125^{th}/250^{th}$ drum turn of the LA abrasion equipment and sorted according to magnitude for plotting with the cumulative number of aggregate particles passing as a percentile value. Similar to the grain size distribution concept as shown in Figure 5.9 through Figure 5.14 presented the overall degradation trends of a certain aggregate shape property in time with the increasing number of LA abrasion drum turns for limestone and granite.

Figure 5.9 shows AI distributions for the limestone ballast material. Each data point represents the AI value for a particle with each curve corresponding to the AI distribution of all the particles after a certain number of drum turns. The gap between any two curves implies how much the AI changed in between different number of turns. Clearly, the AI decreases at a slower rate when moving away from the original curve (0 turn). Accordingly, the distribution curves tend to get closer to each other as they shift towards left, representing a higher number of drum turns.

Figure 5.10 shows ST index distributions for the limestone ballast material and similar patterns are also observed as in the case of AI presented in Figure 5.9. Further, Figure 5.11 presents the F&E ratio distributions for limestone in the same manner. Different from the AI and ST index trends, the F&E ratio distributions change from an initial wider range to much narrower range values. This means that particles generally tend to converge to a certain shape, and often become more flatten, as some of the originally F&E particles are degraded due to abrasion and breakage. Figure 5.12 to Figure 5.14 show the imaging based shape properties of the granite ballast material. Similar degradation trends are observed for granite when compared those of the limestone presented in previously in Figure 5.9 to Figure 5.11.

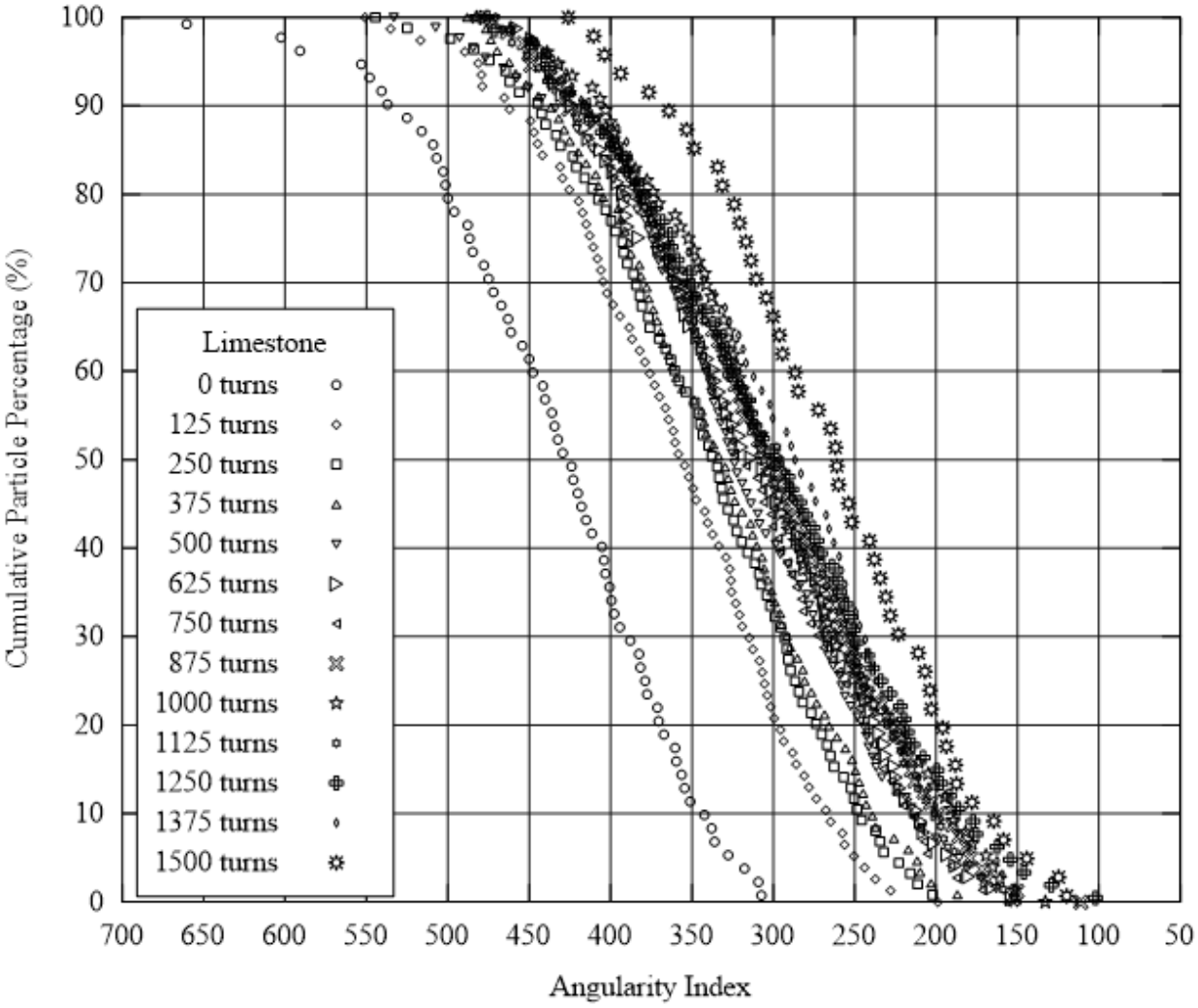

Figure 5.9. Angularity Index Change of Limestone During LA Abrasion Test

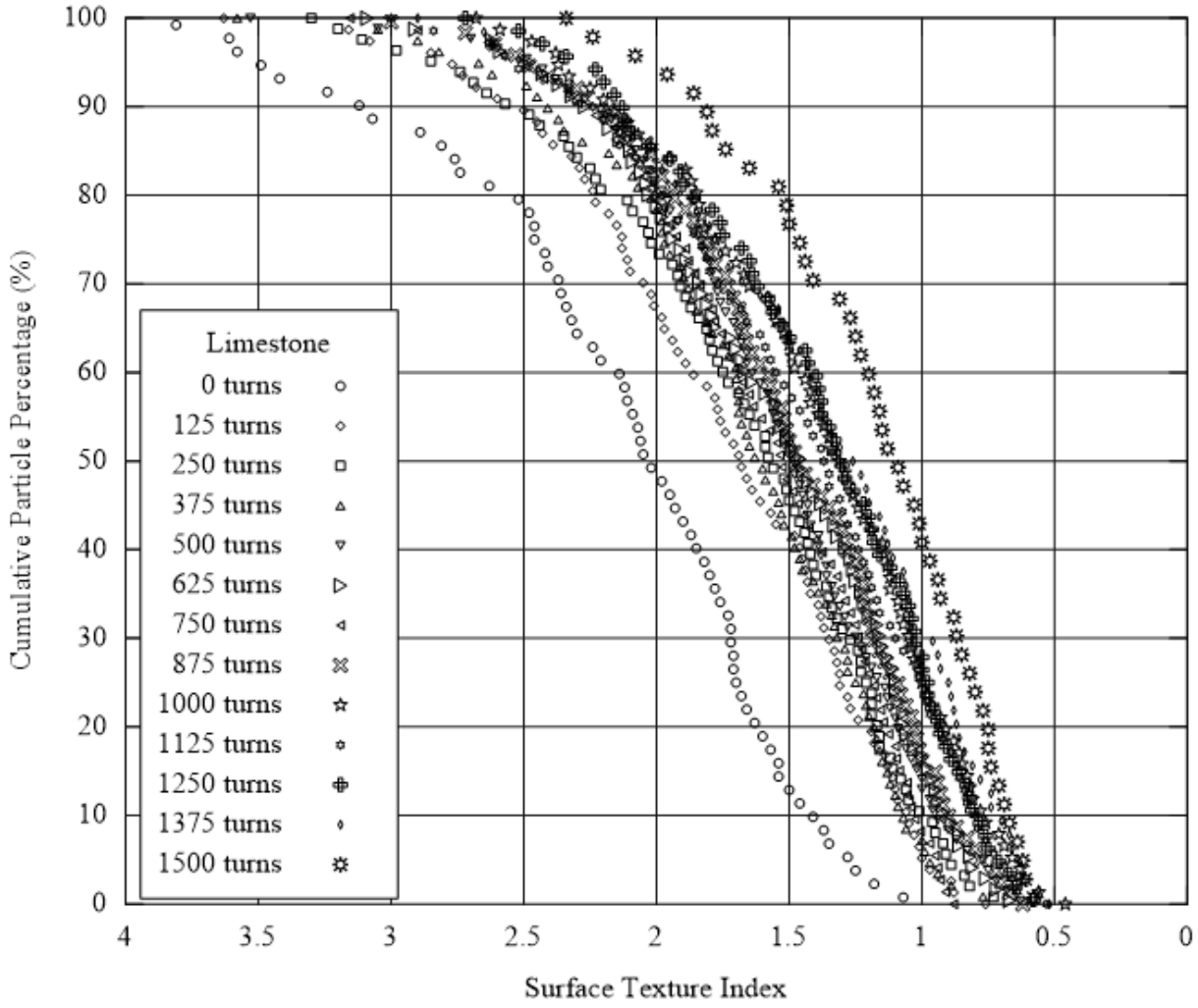

Figure 5.10. Surface Texture Index Change of Limestone During LA Abrasion Test

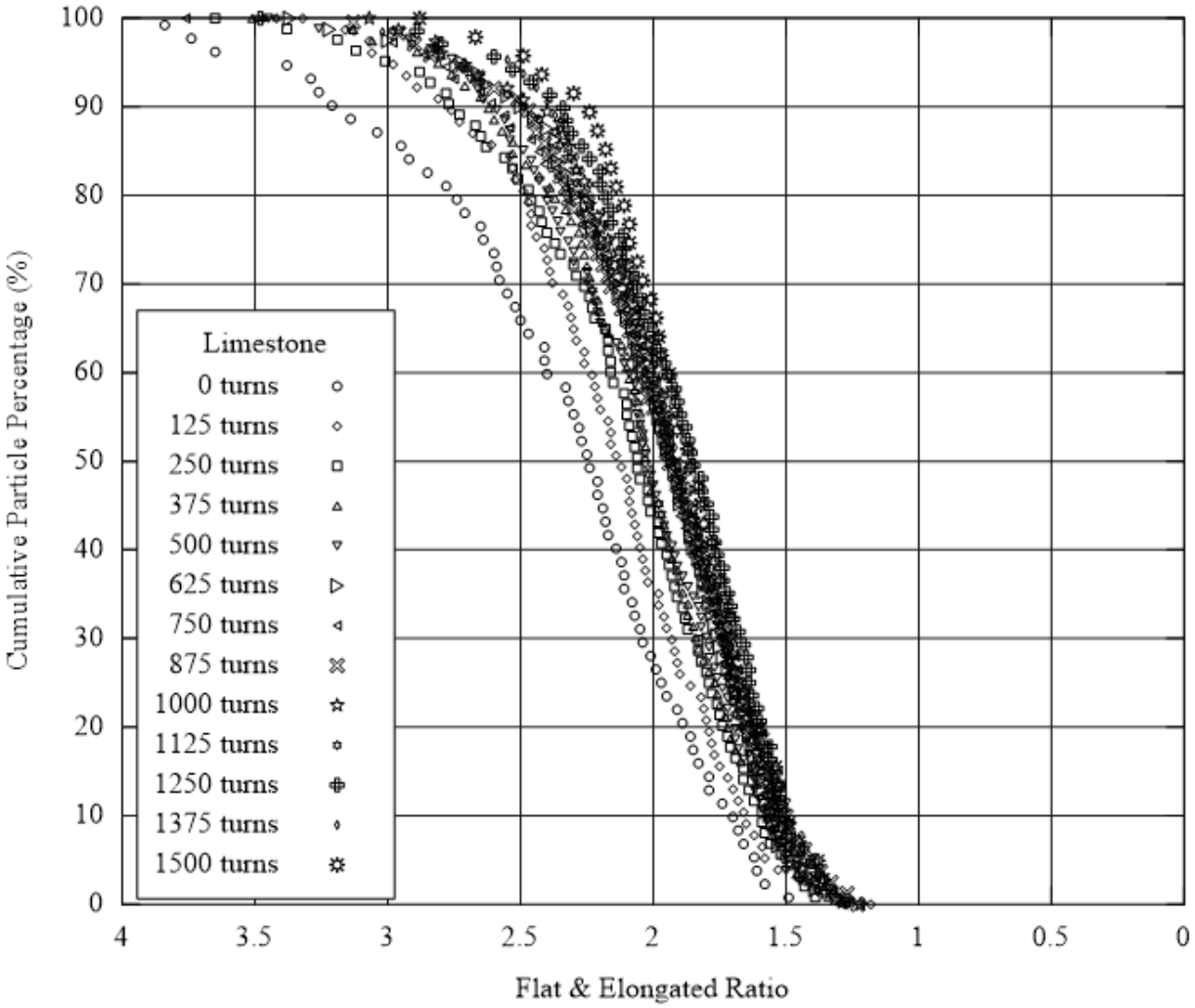

Figure 5.11. Flat and Elongated Ratio Change of Limestone During LA Abrasion Test

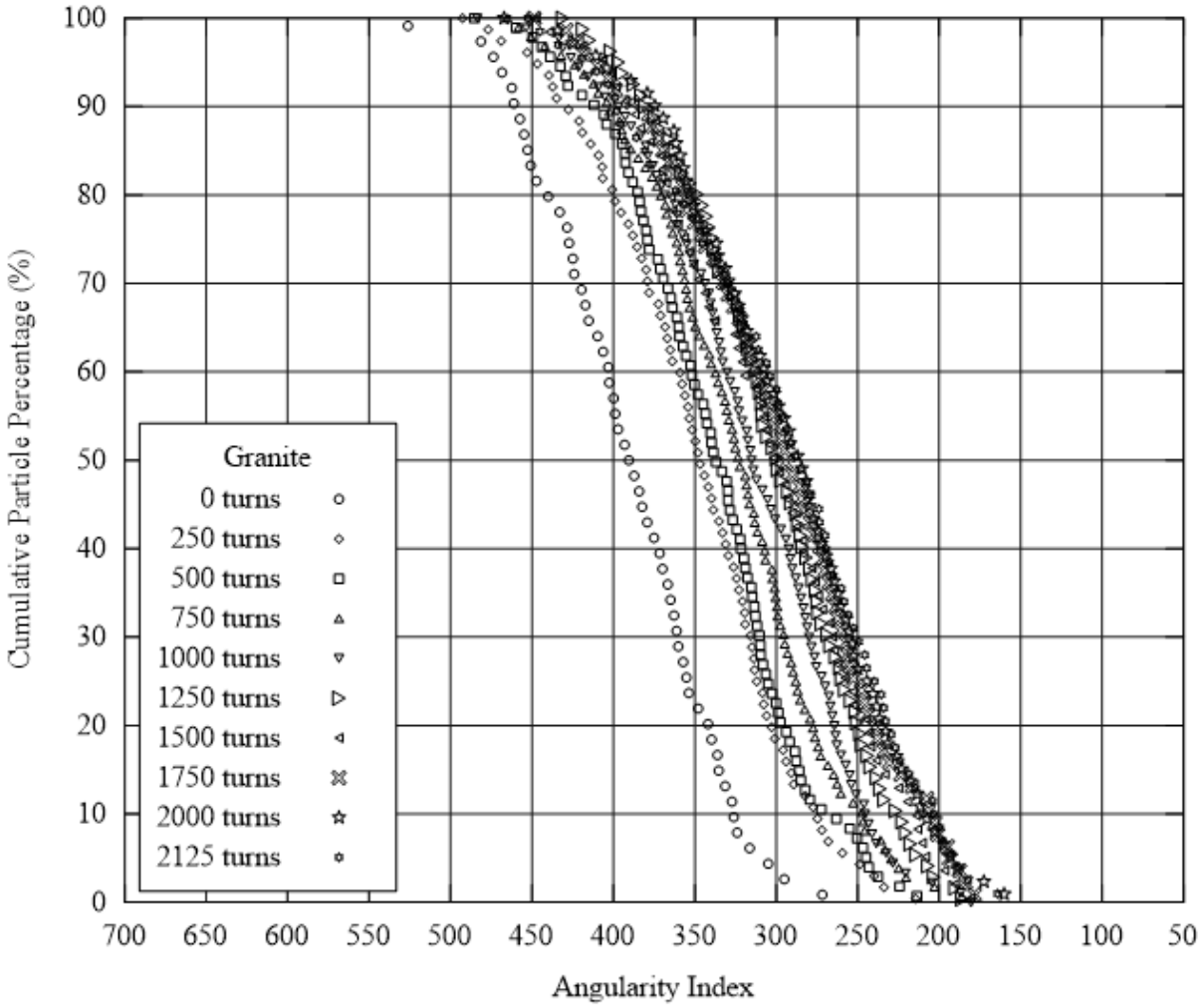

Figure 5.12. Angularity Index Change of Granite During LA Abrasion Test

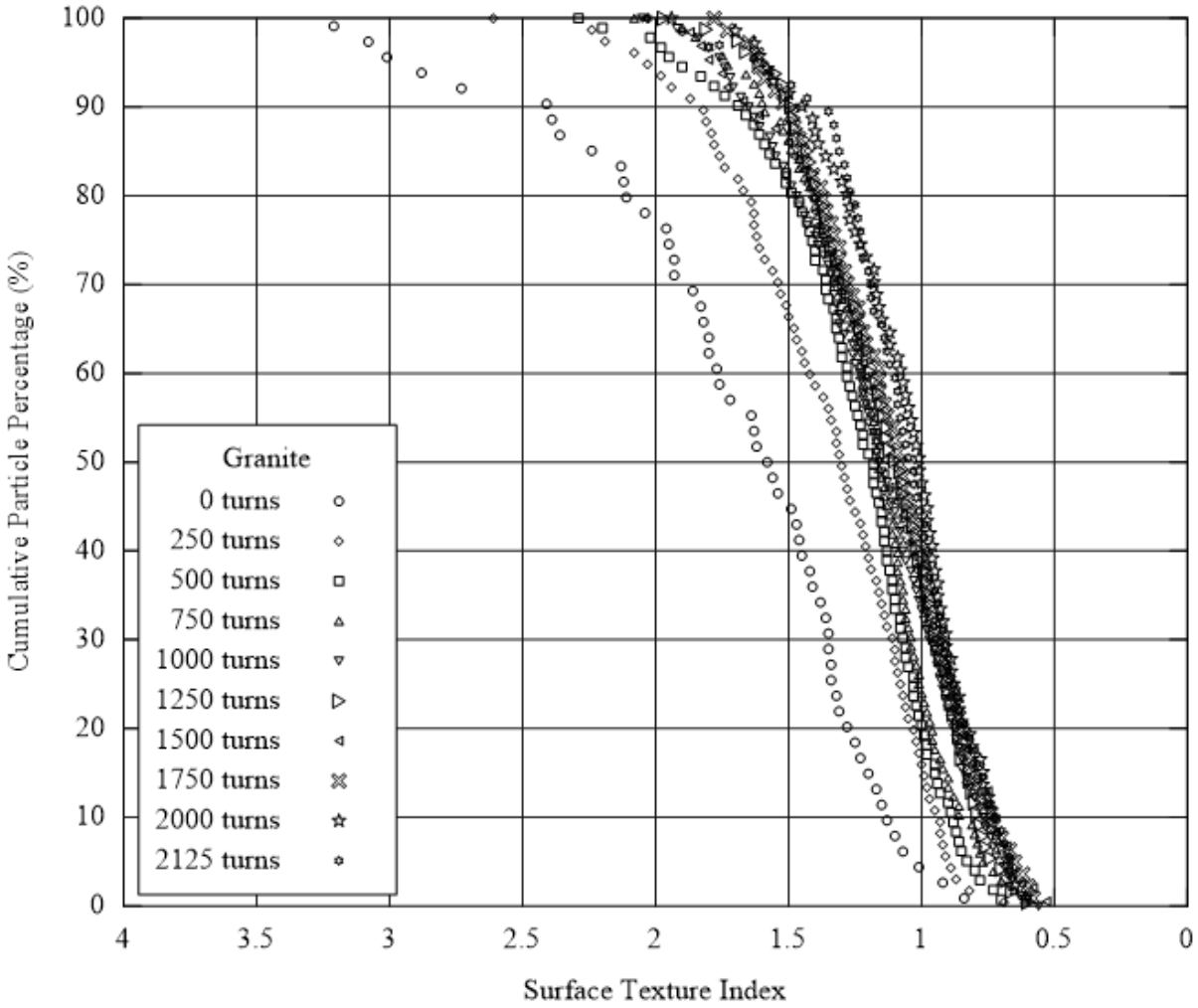

Figure 5.13. Surface Texture Index Change of Granite During LA Abrasion Test

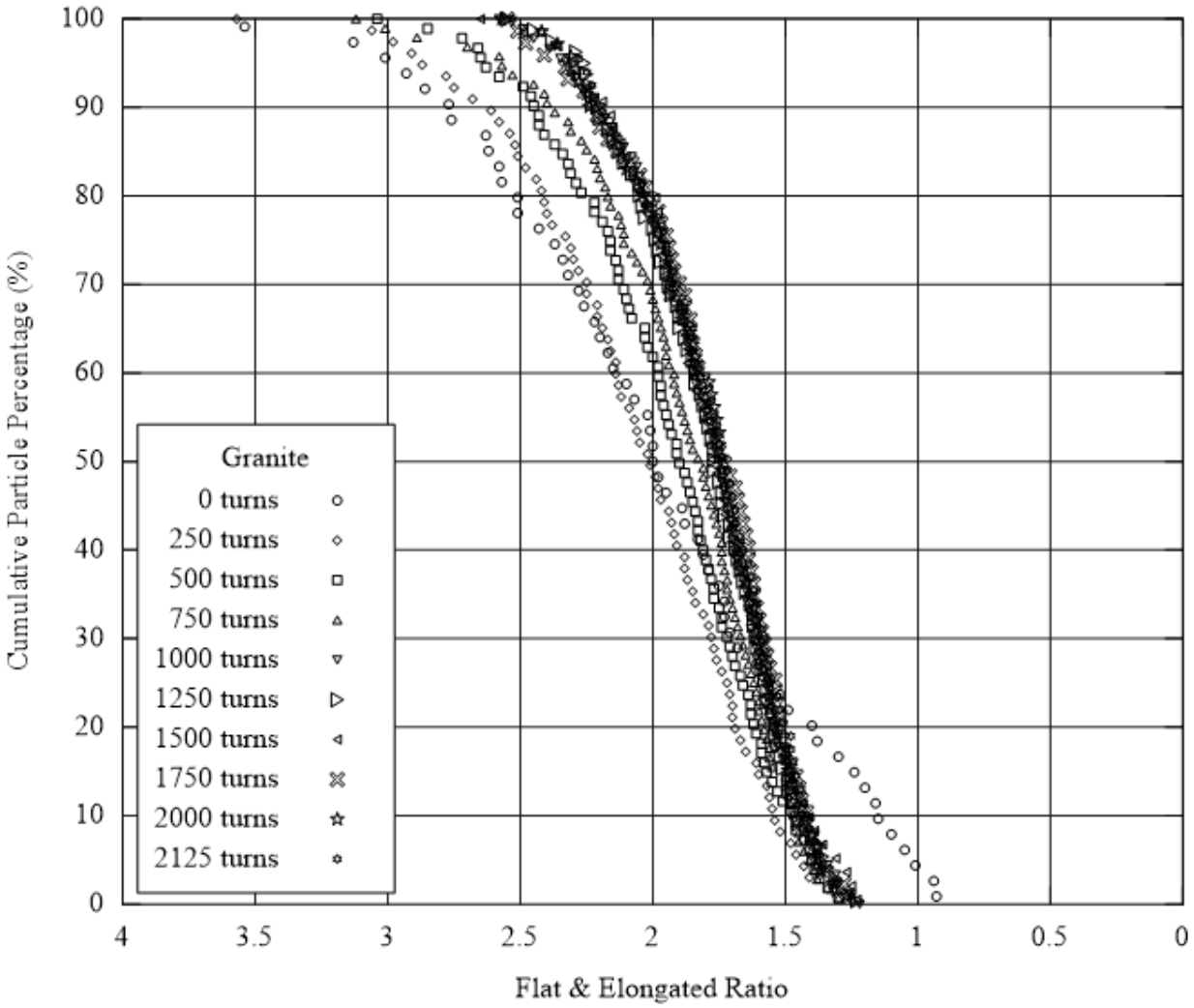

Figure 5.14. Flat & Elongated Ratio Change of Granite During LA Abrasion Test

Table 5.1. E-UIAIA Based Shape Indices of the Limestone Specimen Tested

Opening size (mm) \ No. of turns		0	125	250	375	500	625	750	875	1000	1125	1250	1375	1500
50	AI	359	281	--	--	--	--	--	--	--	--	--	--	--
37.5		400	285	267	289	212	211	211	210	210	227	201	212	182
25.0		436	331	300	290	271	267	267	257	239	242	228	225	228
19.0		443	336	333	310	306	293	295	291	284	287	284	284	274
12.5		526	385	383	366	345	345	335	335	331	343	332	329	329
9.5		--	409	380	387	379	372	371	373	371	378	378	369	378
average		433	338	332	328	304	298	296	292	287	295	284	284	278
50	F&E Ratio	1.5	1.4	--	--	--	--	--	--	--	--	--	--	--
37.5		2.2	1.9	1.9	1.8	1.9	1.9	1.9	1.9	1.8	1.9	1.8	1.8	1.8
25.0		2.4	2.1	2.1	2.0	2.0	1.9	1.9	1.9	1.9	1.9	1.8	1.8	1.8
19.0		2.7	2.1	2.1	2.2	2.0	2.0	2.1	2.1	2.1	2.1	2.1	2.1	2.0
12.5		2.3	2.2	2.1	2.1	2.0	1.9	1.9	1.9	1.8	1.9	1.8	1.9	1.9
9.5		--	2.3	2.3	2.2	2.2	2.1	2.1	2.1	2.1	2.1	2.0	2.1	1.9
average		2.2	2.0	2.0	2.0	2.0	2.0	2.0	2.0	1.9	2.0	1.9	1.9	1.9
50	ST index	1.3	1.0	--	--	--	--	--	--	--	--	--	--	--
37.5		1.8	0.9	0.9	1.3	0.8	0.9	0.8	0.9	0.8	0.9	0.8	0.8	0.8
25.0		2.1	1.4	1.3	1.3	1.2	1.1	1.2	1.1	0.9	1.0	1.0	0.9	0.9
19.0		2.5	1.5	1.5	1.5	1.5	1.4	1.4	1.4	1.3	1.4	1.2	1.2	1.3
12.5		3.1	2.0	2.0	1.9	1.7	1.7	1.7	1.6	1.6	1.7	1.6	1.6	1.6
9.5		--	2.4	2.1	2.1	1.9	2.1	2.1	2.0	1.9	2.1	1.9	1.9	2.0
average		2.1	1.5	1.6	1.6	1.4	1.4	1.5	1.4	1.3	1.4	1.3	1.3	1.3
Total number of particles		146	263	290	290	296	298	308	287	278	263	256	249	231

Table 5.2. E-UIAIA Based Shape Indices of the Granite Specimen Tested

Opening size (mm) \ No. of turns		0	250	500	750	1000	1250	1500	1750	2000	2125
50	AI	388	326	301	280	222	245	213	199	214	224
37.5		377	295	299	272	258	243	230	226	208	211
25.0		384	337	310	292	274	262	254	253	248	241
19.0		416	337	312	310	292	281	274	274	274	267
12.5		441	367	354	346	338	321	322	312	309	312
9.5		--	383	378	356	363	351	350	370	364	369
average		401	341	326	309	291	284	274	274	269	271
50	F&E Ratio	2.2	2.0	1.9	2.0	2.0	2.0	1.9	1.9	1.9	1.9
37.5		2.3	2.0	1.9	1.9	1.8	1.9	1.8	1.8	1.8	1.8
25.0		2.2	2.0	2.0	1.9	1.8	1.9	1.8	1.8	1.7	1.7
19.0		2.4	2.1	1.9	1.8	1.8	1.7	1.8	1.8	1.8	1.8
12.5		2.4	2.0	1.9	1.9	1.8	1.8	1.8	1.7	1.7	1.7
9.5		--	2.1	2.0	1.9	1.8	1.8	1.8	1.8	1.8	1.8
average		2.3	2.0	1.9	1.9	1.8	1.8	1.8	1.8	1.8	1.8
50	ST index	1.3	0.9	0.9	0.8	0.9	0.9	0.9	0.7	0.7	0.6
37.5		1.3	1.0	0.9	0.9	0.8	0.8	0.8	0.8	0.8	0.8
25.0		1.4	1.2	1.1	1.0	0.9	0.9	0.8	0.9	0.9	0.9
19.0		1.6	1.3	1.1	1.1	1.1	1.0	1.1	1.1	1.0	1.0
12.5		2.0	1.5	1.3	1.3	1.3	1.2	1.2	1.2	1.0	1.0
9.5		--	1.7	1.5	1.4	1.5	1.4	1.4	1.4	1.4	1.4
average		1.5	1.3	1.1	1.1	1.1	1.0	1.0	1.0	1.0	1.0
Total number of particles		135	257	300	302	297	286	277	253	239	235

As clearly seen in Figure 5.7 and Figure 5.8, FI by Selig and Waters is a good indicator of ballast fouling condition, since it adequately relates to reduced void space and increased particle packing in this well-graded and smaller top-sized fouled ballast layer composition (Selig, E. T., and Waters, J. M., 1994). Because both ballast fouling and shape property changes are due to particle abrasion and breakage from LA abrasion drum turns, the next step was to investigate how the change in FI values would correlate to changes in aggregate particle shape indices as

quantified by the E-UIAIA. Indeed, Figure 5.15 shows a strong correlation between the percent change in average AI values and FI with a coefficient of determination (R^2) of 87 percent and 92 percent for limestone and granite, respectively. Similarly, Figure 5.16 also presents another strong correlation between the percent change in average ST indices and FI this time with a coefficient of determination (R^2) of 81 percent and 90 percent for limestone and granite, respectively. Such trends shown in both Figure 5.15 and Figure 5.16 suggest that there is a definite correlation between ballast fouling and the overall reduced angularity and surface texture properties of ballast aggregate particles, which is also highlighted recently from field degradation trends by Ahuja et al. (2013). Understanding such relationships between ballast fouling levels and degradation in ballast size and shape properties could improve DEM ballast modeling efforts to simulate realistic ballast behavior at different fouling levels and utilize field imaging techniques to determine field ballast serviceability. There is certainly more to learn by linking these findings to field degradation trends to capture both spatial property variability and property changes within the ballast layer depth to establish field usage and ballast life cycle under revenue service loading.

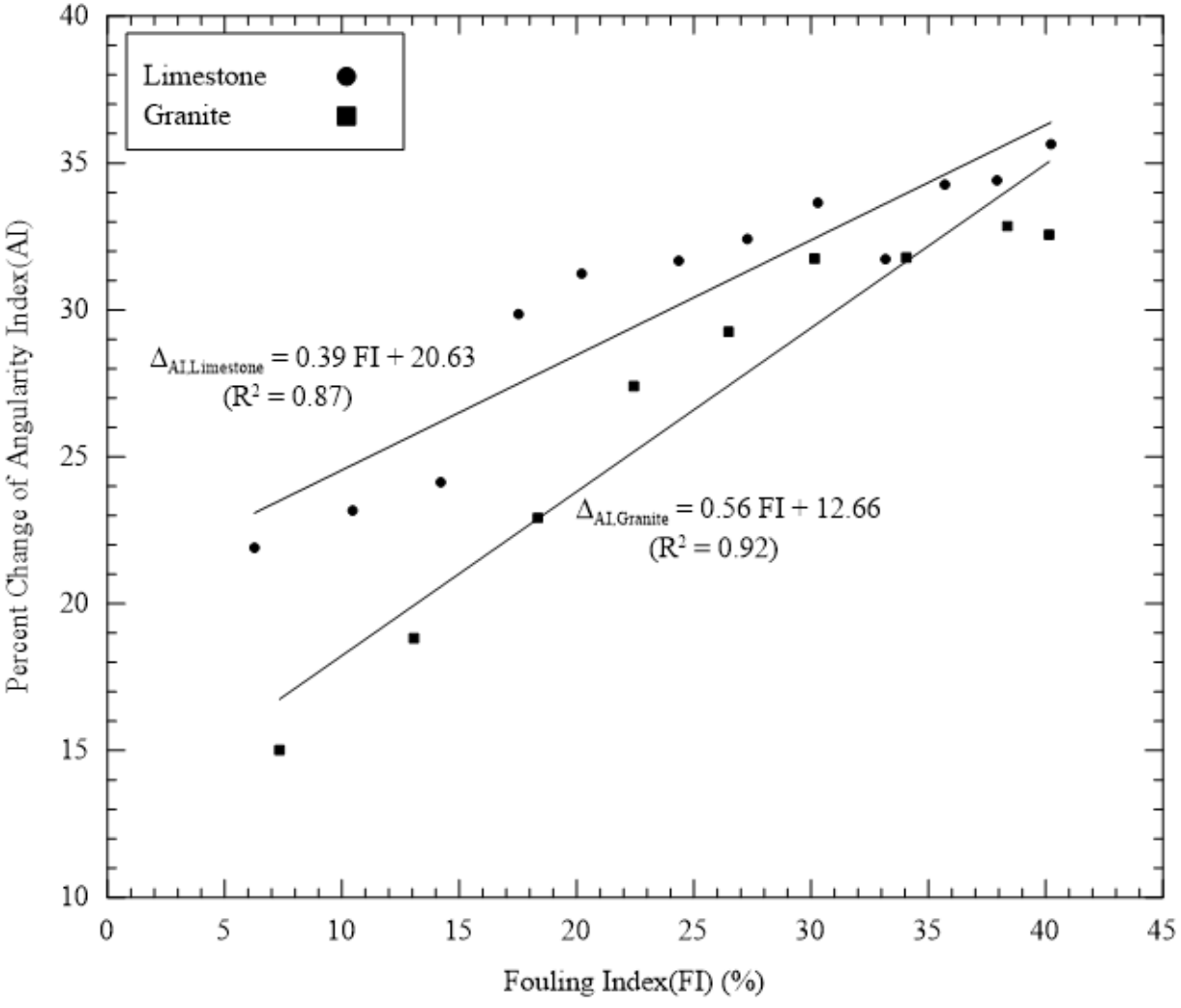

Figure 5.15. Angularity Index Change with Fouling Index During LA Abrasion Test

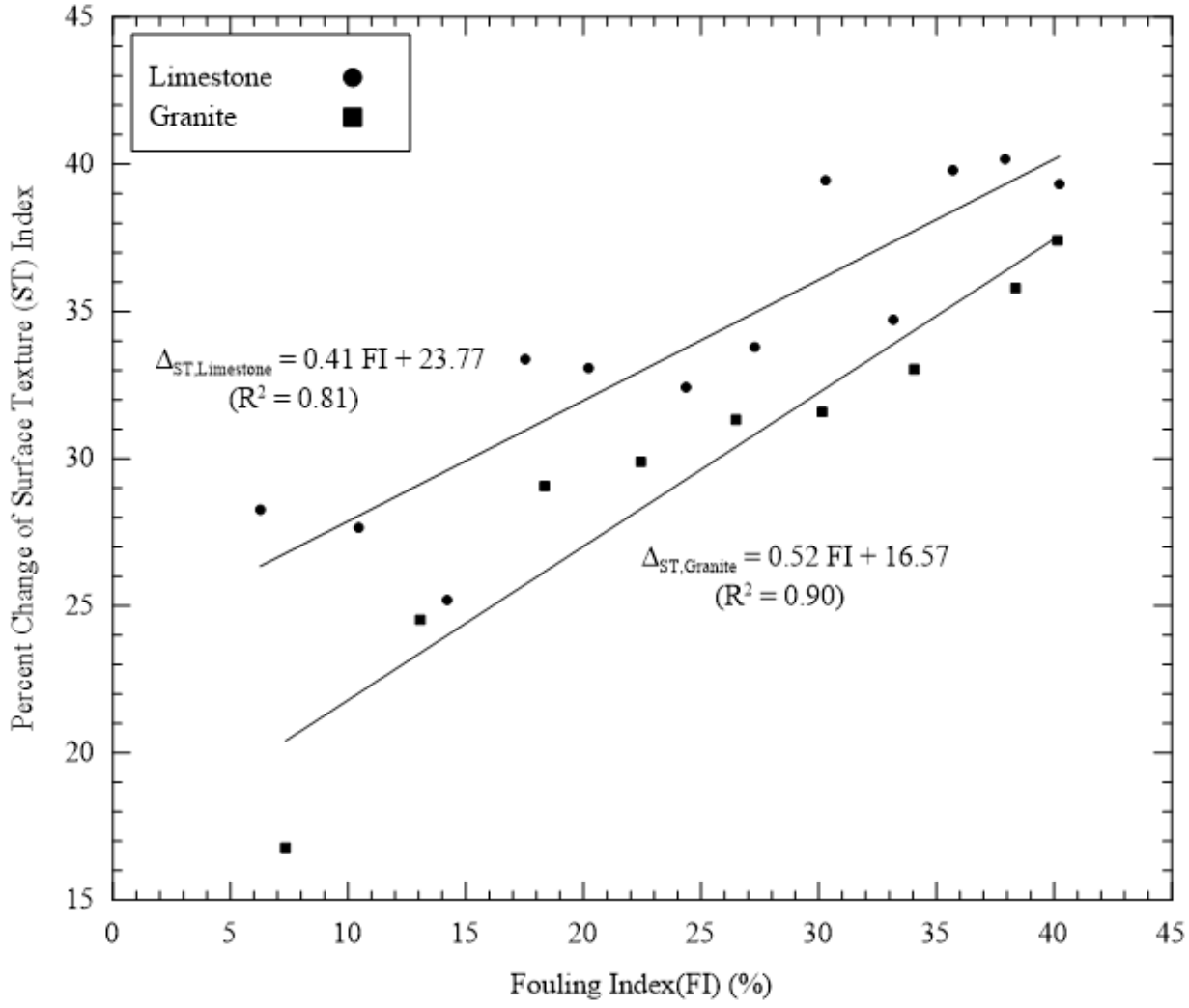

Figure 5.16. Surface Texture Index Change with Fouling Index During LA Abrasion Test

6. Study on the Fouled Ballast Behavior via Lab Scale Experiments and DEM Simulations

6.1 Laboratory Experiments with the Generated Fouled Ballast Materials

Ballast fouling or degradation is considered unfavorable and routinely railroads carry out maintenance by cleaning ballast and performing undercutting-type track activities. Previous studies report that fouling can significantly reduce ballast strength. Huang et al. conducted a series of large scale direct shear tests that used ballast mixed with different fouling agents including coal dust and fine-grained cohesive subgrade soil (Huang, H., Dombrow, W., and Tutumluer, E., 2009). Indraratna et al. recently performed large scale triaxial tests on ballast fouled with different proportions of clay (Indraratna et al., 2013). However, the mechanics behavior of clean ballast and fouled ballast due to degradation of the same particles has not been compared and fully understand

This section presents the results of the large scale triaxial tests that were conducted on the fouled ballast materials generated by the project's LA abrasion testing (described previously). The permanent deformation tests utilized the same triaxial test device and the same realistic field pulse loading, i.e., 0.4-second duration haversine loading with a 0.6-second rest period (explained in the next section), was applied on the fouled ballast specimens up to 10,000 loading cycles. The permanent deformation tests were then simulated using the DEM approach.

Table 6.1. Comparison of Test Conditions of Different Ballast Materials

Ballast Type	Specimen Weight	Void Ratio	Compaction Time	Fouling Index
Limestone	70 kg	0.68	16 s	0
Fouled Limestone (Only 3/8''+)	73 kg	0.61	16 s	0
Fouled Limestone	94 kg	0.25	16s	40

The first ballast material tested was fully fouled limestone with a FI of 40. Both the strength tests and permanent deformation tests were conducted on this heavily fouled limestone material. To adequately model the aggregate skeleton of this heavily fouled ballast and perform DEM simulations, fine material smaller than 9.5 mm (3/8 in.) in particle size was sieved out and not included in the triaxial tests. Figure 6.1 shows the gradation properties of the clean and fouled ballast material, and the scalped gradation or coarse aggregate fraction (sizes above 9.5 mm or 3/8 in.). The specimen preparation steps and procedures, which were described earlier, were followed for testing the heavily fouled and scalped gradation ballast specimens similar to the clean ballast. Table 6.1 summarizes the similarities and differences of testing conditions and properties of the fouled ballast and clean ballast specimens.

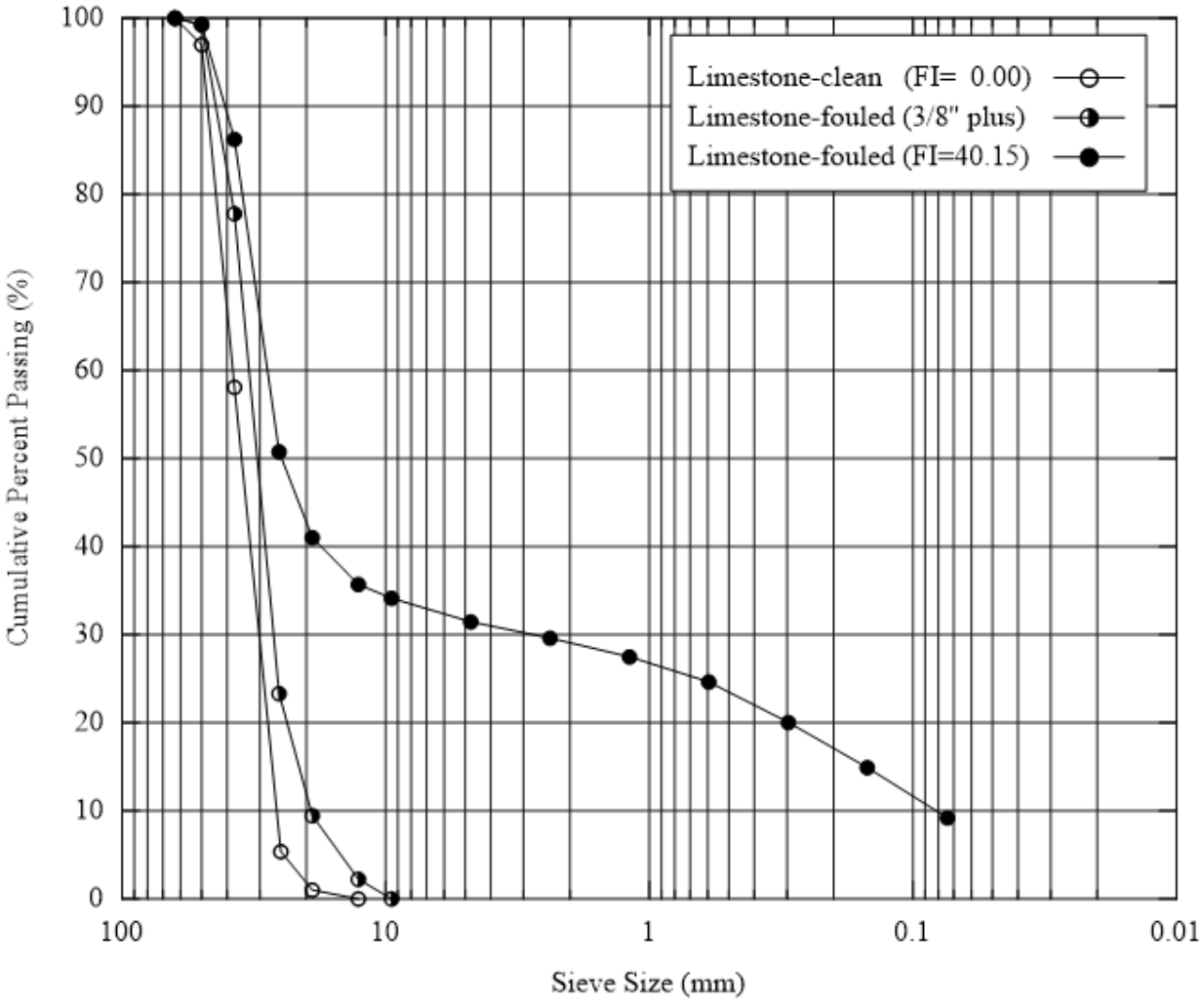

Figure 6.1. Limestone Gradation at Different Fouling Conditions During Laboratory Triaxial Permanent Deformation Test

6.1.1 Permanent Deformation Tests with Repeated Loading

To investigate the ballast permanent deformation behavior, triaxial tests with repeated loading were conducted in the laboratory. The loading pulse employed was the same haversine shape loading used in tests with clean ballast at 0.4-second load duration and 0.6-second rest period between the two load cycles as shown previously in Figure 4.7. The applied confining pressure and deviator stress pairs were the same as they were in the tests of the clean ballast specimens. Three specimens were prepared and tested in repeated loading up to 10,000 cycles. The deformation of the middle part of the specimen was recorded during each loading cycle.

In Figure 6.2 presents the permanent deformation test results up to 10,000 cycles for the three different limestone samples: (1) clean ballast, (2) heavily fouled ballast (FI=40), and (3) scalped gradation, or coarse aggregate fraction (sizes above 9.5 mm or 3/8 in.), obtained from the fouled ballast material. Three replicate permanent deformation tests were conducted on each material. This required carefully collecting and remixing the same sample for using in the next test and

thus eliminating the effect of any sample variability and contamination in material composition. Gradation was also checked after the permanent deformation tests to confirm that no significant change was encountered in particle size distribution.

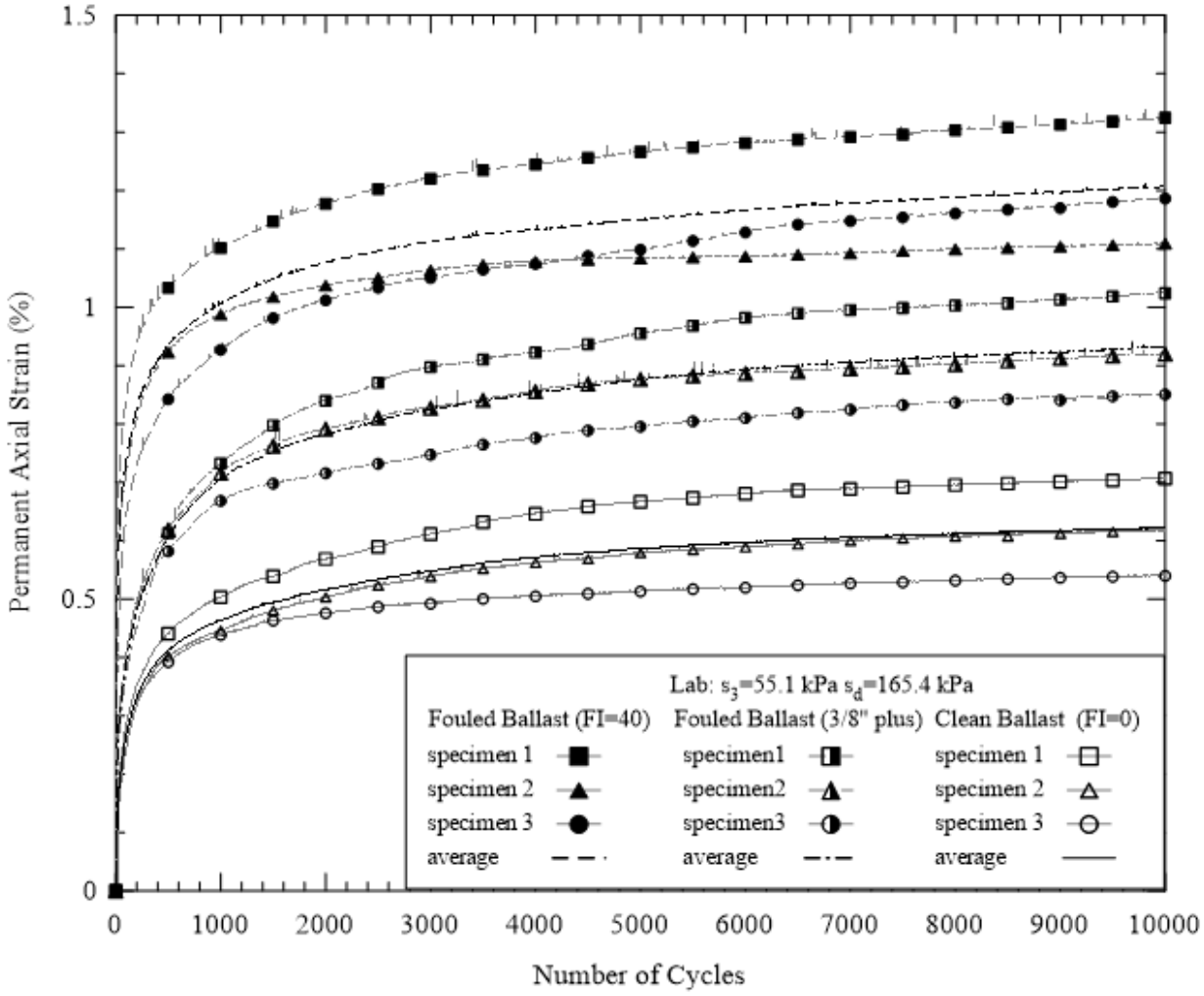

Figure 6.2. Laboratory Ballast Triaxial Permanent Deformation Test Results with Limestone at Different Fouling Conditions

Again, as shown in Figure 6.2 the results of the permanent deformation tests. The heavily fouled ballast specimens clearly resulted in the highest permanent axial strains measured. After 10,000 load cycles, the clean ballast specimens had an average permanent strain of 0.62 percent, while the heavily fouled ballast specimens yielded an average permanent strain of 1.21 percent. The scalped gradation or the coarse aggregates fraction of the fouled ballast had permanent axial strain values in between the clean ballast and heavily fouled ballast with an average permanent axial strain value of 0.93 percent. The difference between the clean ballast and coarse aggregates fraction of the fouled ballast is again due to the differences in gradation and the particle shape properties. In other words, no fine fouling materials, i.e., particles smaller than 9.5 mm (3/8 in.), were present in the samples of these two materials. The scalped gradation had much smaller particles (still larger than 9.5 mm), also indicated by the gradation curve shown in

the Figure 6.1. Also, the aggregate particles were smoother with lower imaging based AI and ST index values given in Table 6.2.

Table 6.2. Properties and UIAIA Based Shape Indices of Ballast Material Tested

Ballast Type	Angularity Index (degrees)	Flat & Elongation Ratio	Surface Texture	C_u	C_c
Limestone	440	2.3	2	1.46	0.97
Fouled Limestone (Only 3/8''+)	278	1.9	1.3	1.79	1.13

The heavily fouled ballast specimens had the highest permanent axial strain among the three different ballast materials with an average permanent axial strain of 1.21 percent after 10,000 cycles of loading. Note that the difference between the heavily fouled ballast and the scalped gradation of the coarse aggregates fraction was the fouling fine material (particles smaller than 9.5 mm or 3/8 in.) due to the ballast self-degradation from the LA abrasion tests. These fine materials not only filled the voids but caused loss of contact between large particles in the heavily fouled ballast aggregate skeleton shown in Figure 6.3.

Figure 6.3. Fouled Ballast Specimen (FI=40) After Laboratory Permanent Deformation Testing

6.1.2 DEM Simulations of Permanent Deformation Tests on Coarse Aggregates Fraction of the Fouled Ballast

Simulating Repeated Loading by IDSM

The results of the large scale triaxial permanent tests on the limestone ballast specimens clearly show that permanent deformations in general increase with the number of load cycles but at a decreasing rate of accumulation. Different ballast materials, i.e., the clean ballast, heavily fouled ballast, and the scalped gradation of the coarse aggregate fraction (larger than 9.5 mm or 3/8 in. size) of the heavily fouled ballast showed typical trends of permanent deformation accumulation. There are two important observations: 1) when the uniform ballast gradation changes from coarse to fine (see Figure 6.1 for clean and fouled with 3/8-in. plus), the accumulation of permanent deformations increases, and 2) when fine materials (smaller than 9.5 mm or 3/8 in. size) are present, typically in a heavily fouled ballast sample, there is a significant increase in the accumulation of permanent deformations.

Note that permanent deformations mainly accumulated during the first 2,000 cycles for all the limestone samples tested, then increased slowly and eventually became somewhat stable. Because the main difference between clean ballast and the scalped gradation of the coarse aggregate fraction (larger than 9.5 mm or 3/8 in. size) of the heavily fouled ballast is the gradation and particle shape properties, the same approach to simulating the clean ballast permanent deformation behavior can be used to simulate the permanent deformation behavior of the scalped gradations. However, as discussed before, the particle contact mechanism of the heavily fouled ballast is significantly different than the contact mechanism of the clean ballast. Nevertheless, due to limits on available computation time and CPU speed, it is not feasible and practical to consider the full gradation of the heavily fouled ballast sample in DEM simulations—which would require taking into account so many fine particles, smaller than 9.5 mm or 3/8 in. size.

DEM Simulation Results of Permanent Deformation Tests

In Figure 6.4 presents the permanent deformation test results and the DEM simulation predictions of the scalped gradation samples of the heavily fouled ballast for up to 2,000 loading cycles. Similar to the previous DEM simulations of clean ballast material, the "incremental displacement" shearing method was used to simulate the scalped gradation samples as referred to here as the large aggregate fraction of the fouled ballast. Both the experimental results and DEM simulation predictions of the clean ballast are also provided in Figure 6.4 for comparison. The average DEM predictions from three different initial conditions show in general good agreement with the developing trend of the permanent deformation with the experimental results. The permanent deformation for both clean ballast and the scalped gradation ballast accumulate rapidly at the initial stage and increase asymptotically. The scalped gradation ballast had higher permanent deformation at the initial stage but a similar increase rate at later stages when compared with clean ballast. By accounting for the random variability of the initial particle packing conditions, the DEM predictions can vary considerably within a certain range. Finally, the DEM simulations predicted the permanent deformations for up to 2,000 loading cycles reasonably accurately.

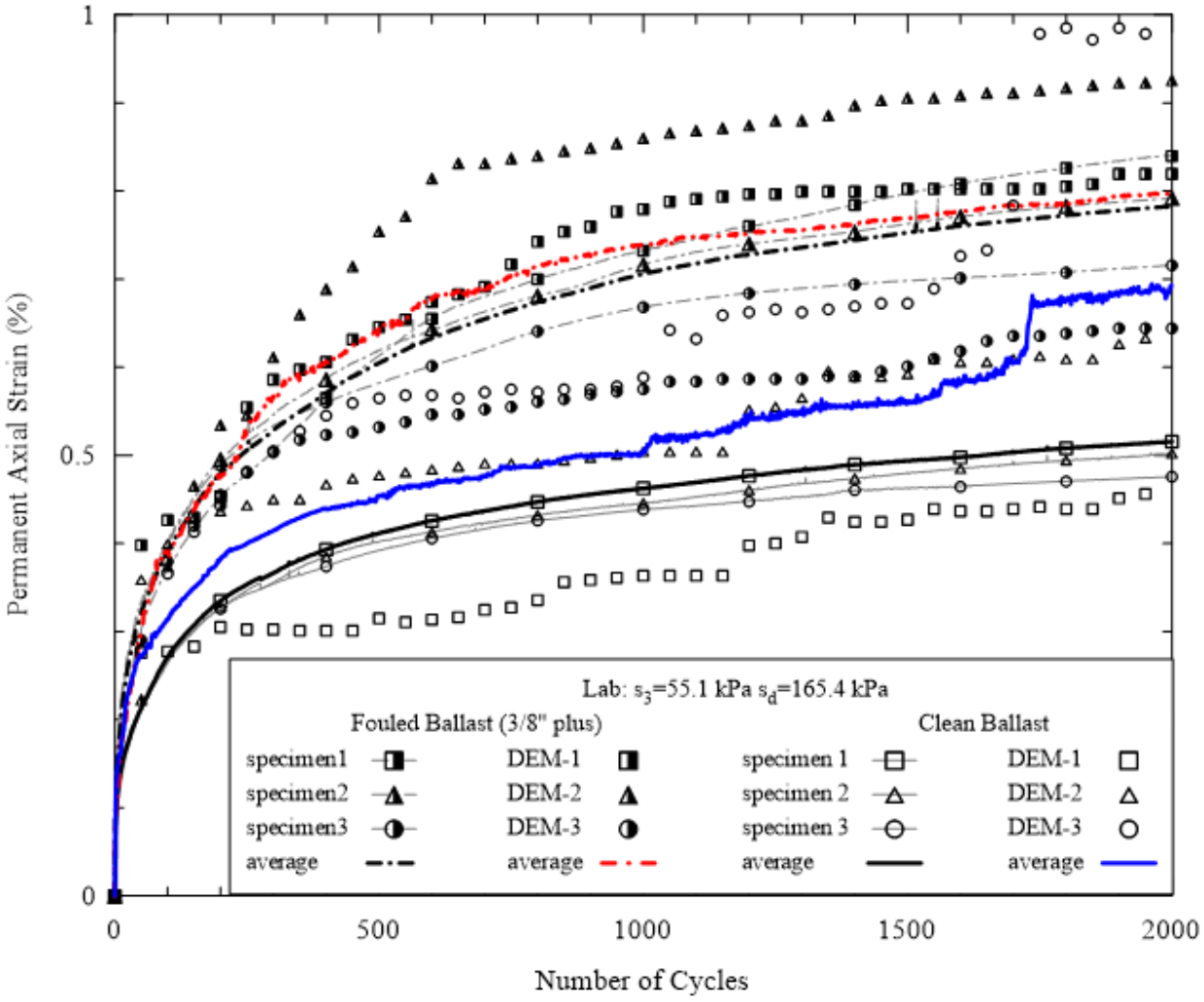

Figure 6.4. Comparison of DEM Predictions and Permanent Deformation Test Results up to 2,000 Cycles for Clean Ballast and Large Aggregate Fraction of Fouled Ballast

7. Development of Software to Support Ballast DEM Model

7.1 Overview of the Graphical User Interface

A graphical user interface (GUI) has been developed to provide an easy and straightforward for user access to the DEM model as a quantitative track performance tool. The integrated software package of the GUI and the DEM analysis module provide a complete user experience of modeling, simulation and quantitative estimation of the complex behavior of the railroad ballast materials under diverse loading scenarios. To help users with modeling ballast material behavior correctly and without receiving error messages, the GUI employs a modeling procedure that guides users through the appropriate steps and also along with modeling templates for specific types of problems, such as triaxial tests and track modeling as shown in Figure 7.1. Some of these steps allow users to interactively generate configurations by using the mouse to zoom, rotate, and pan in the built-in 3D graphical interactive view.

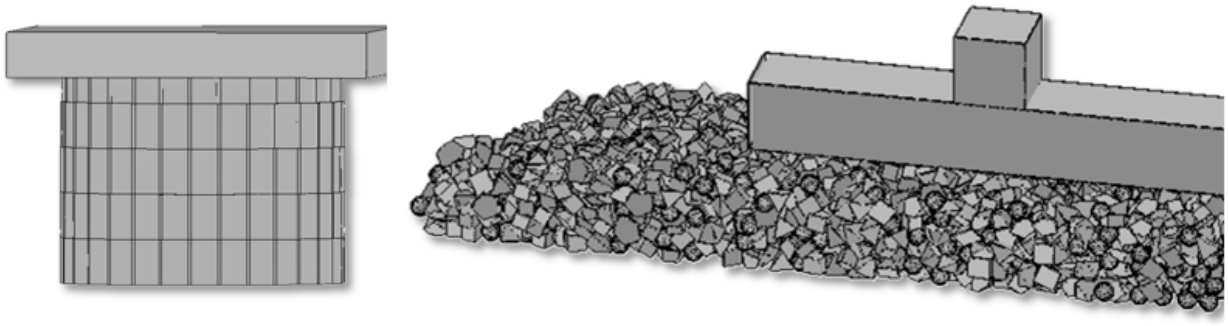

Figure 7.1. Modeled Configuration from the User Interface; (a) Triaxial Compression; (b) Field Half-Track Settlement Simulation

The GUI is designed to provide the modeling capability for the systematic multi-scale approach used in the DEM modeling research on railroad ballast materials (as discussed in previous sections). Therefore, the GUI provides the multi-scale discrete element modeling framework to relate fundamental mechanisms at all scales in the simulation, such that users can systematically model the grain scale properties such as particle shapes and sizes of ballast granular material system of interest, and then applied loading characteristics to simulated field condition and estimating ballast behavior.

The following sections present the structure of the software (Section 7.2) and the features available in each modeling step (Section 7.3).

7.2 Structure of BALLAST-BLOKS3D

BALLAST-BLOKS3D is the complete software package consisting of the GUI and the DEM analysis for railroad ballast materials. The development effort on the pre-processing and post-processing are well defined and the BALLAST-BLOKS3D program comprised of three parts:

- Pre-processor: BALLAST-BLOKS3D.app
- Analysis module: BALLAST-BLOKS3D.anl

- Post-processor: BALLAST-BLOKS3D.post

The pre-processor generates input files for the analysis module, which reads the input file and particle library file and generates the plot file. With the plot file and particle library file, the post processor displays the output in a graphical format. The schematic structure is shown in Figure 7.2.

Each component of BALLAST-BLOKS3D communicates through text files exchange. Each file shown in Figure 7.2 is a text file except the restart file, is a binary file that does not have a file extension. The files shown in the figure is generated by the pre-processor or the analysis module, except the particle library.

The **particle library** defines the particle shapes that are used in modeling and the simulations. The current version of BALLAST-BLOKS3D software package cannot generate the particle library, which means that the user must generate it externally before it can be used in BALLAST-BLOKS3D.app. A later version of BALLAST-BLOKS3D will address the particle shapes generate issues.

The user can either start a new project or resume an existing project by opening an existing project file. Once modeling is done, the graphical user interface (BALLAST-BLOKS3D.app) will generate two files: the **project file** and the **input file**.

The project file contains information on the project settings, and also contains the names of the restart file and particle library that are used for modeling for the project. If the user wants to resume a simulation conducted prior or wants to perform a similar simulation with the simulation previously carried out with change of values for modeling parameters, the user should open this file.

The input file contains all commands for performing the simulation, which are fed to BALLAST-BLOKS3D.anl along with the particle library file. In case of a resumed simulation, it will contain the associated restart file which is also pointed by the project file opened.

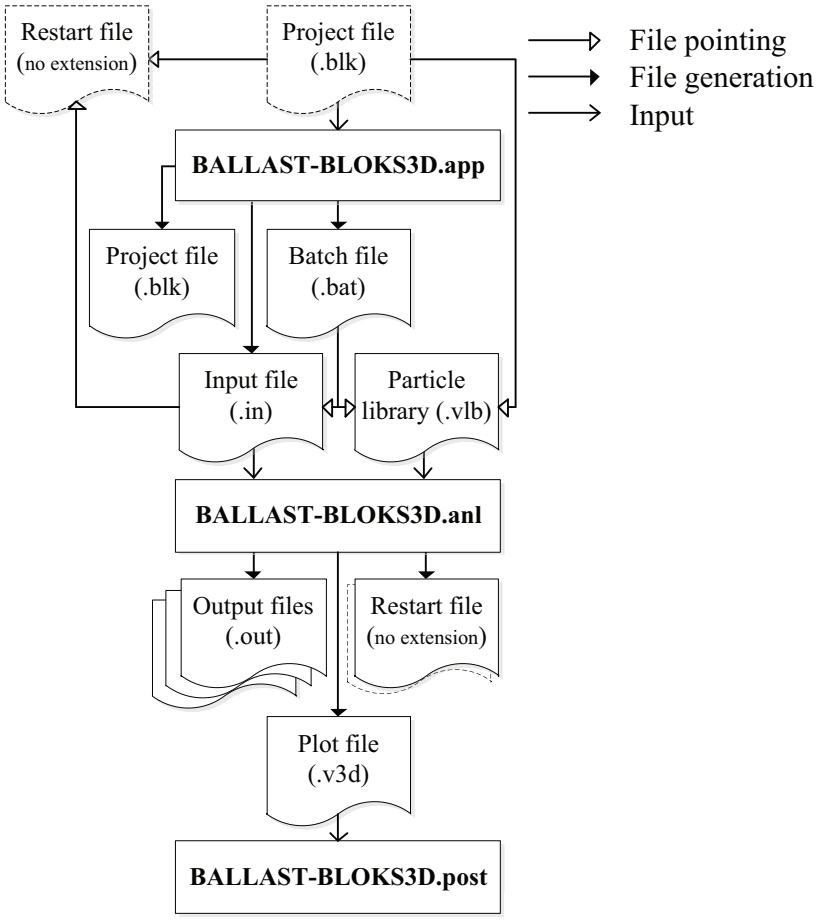

Figure 7.2. Flowchart Represents an Algorithm of the BALLAST-BLOKS3D

Once the simulation is completed by the analysis module (BALLAST-BLOKS3D.anl), it generates three types of files: the **restart file**, the **plot file** and a few **output files**.

The **restart file** contains all the information from a specific time step during a simulation so that simulation can be resumed from the specific timeframe for print out file. The frequency of printing restart files is a parameter in the input file, which can be selected by the user via BALLAST-BLOKS3D.app. Therefore, the number of restart files to be printed out depends on user choice.

The **plot file** contains the configuration and geometry information of all particles over the time steps throughout the simulation. BALLAST-BLOKS3D.post uses this file when it provides graphical post-processing of configurations. The frequency of printing the information in the plot file can also be selected like that of the restart file. However, it contains all the information from the time steps in a single file, while the restart files are separately generated from different time steps the user specified.

The **output files** contain a variety of information about the simulation such as contact force, memory usage, volume change of a triaxial chamber, etc.

7.3 Modeling Steps of BALLAST-BLOKS3D.app

In order to use the modeling features in the current version of BALLAST-BLOKS3D.app, the following steps must be performed as outlined below:

- Step 1: Project setting
- Step 2: Boundary conditions
- Step 3: Grain size distribution
- Step 4: Particle shape
- Step 5: Initial particle location
- Step 6: Material definition and assignment
- Step 7: Contact parameters and global variables
- Step 8: Additional controls

Step 1: Project Setting

The user can provide project information such as the title and comments and create the input file name as shown in Figure 7.3. By setting input such as the acceleration to each axis can be defined by the Cartesian coordinate system. The user can enter the name of the input file to be generated in the File Name edit box. If the user enters information into the Title and Comments edit boxes, they will be printed out as comments on the input text file that is generated at the end of modeling.

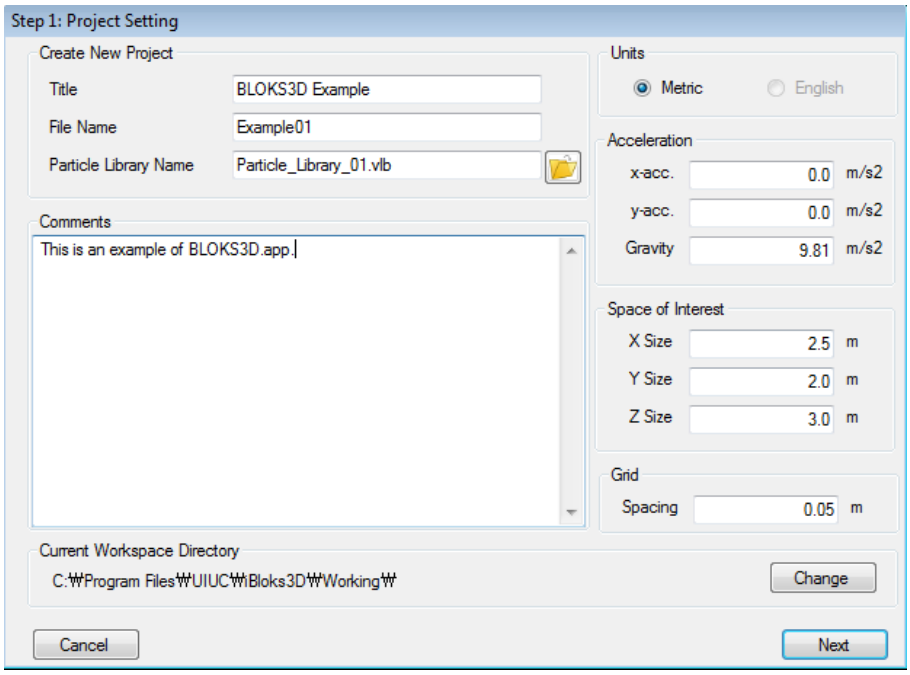

Figure 7.3. Step 1. Project Setting Window

Step 2: Boundary Conditions

The user selects boundary conditions from the given template. The boundary can be modeled via planes (Boolean half-spaces) or cuboid elements as shown in Figure 7.4. Modeling with the planes (Boolean half-spaces) is generally easier than using cuboid elements, since the first choice is just infinite planes without thickness. However, if the user wants to see the boundary motions updated by interactions with particles, such as the membrane of a triaxial testing chamber, the boundary should be modeled with cuboid elements.

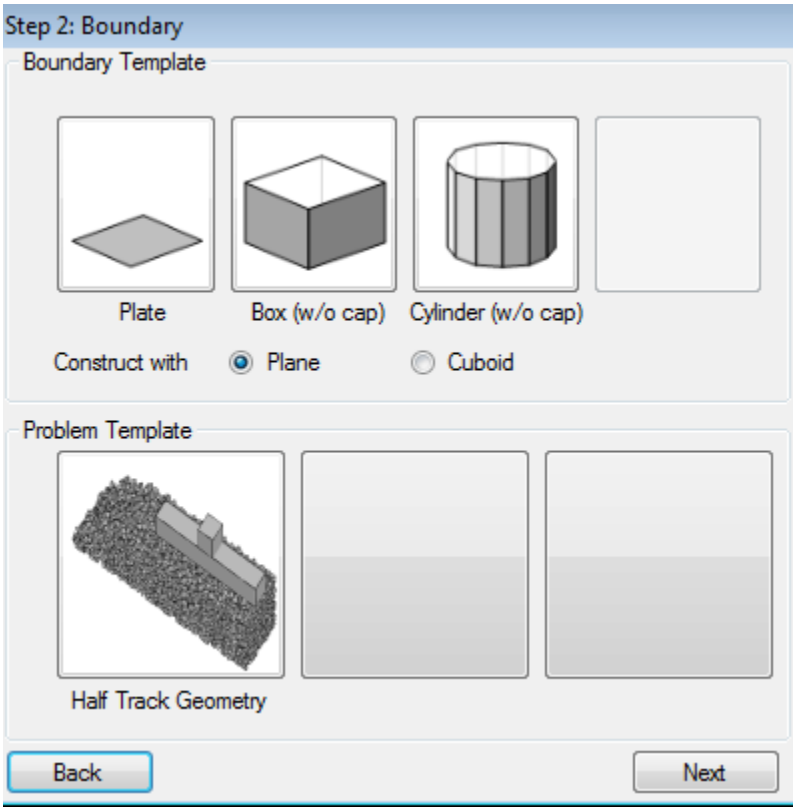

Figure 7.4. Step 2. Boundary Setting Window

Step 3: Grain Size Distribution

In this step as shown in Figure 7.5, the user specifies the size of particles that are considered by the simulation via the grain size distribution. The user enters the size (in centimeter) and the corresponding percent finer by weight in fields in the right pane. Once the input is done, the user can click the **Apply** button to see the generated grain size distribution.

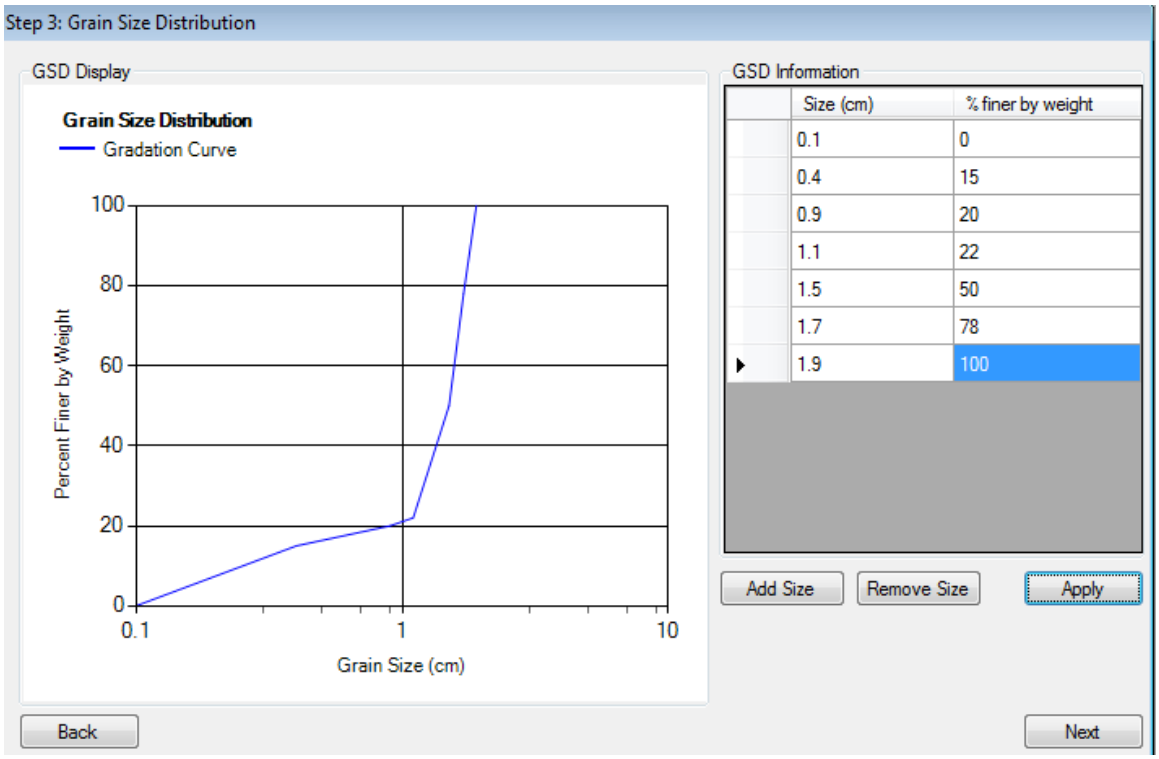

Figure 7.5. Step 3. Grain Size Distribution Window

Step 4: Particle Shape Selection

The user selects the particle shapes to be simulated from the dialog box as shown in Figure 7.6. The particle shapes in this dialog box are from the particle library which was selected in Step 1. The particle shapes defined in "Particle_Library_01.vlb" are provided in the software package. The user selects a particle by clicking the particle image button and de-selecting the same image button once again. The image of the selected particle is also shown on the right pane and the user can examine the 3D image in more detail by using the **Start**, **Pause**, and **Stop** buttons and additional information on the selected particle such as number of vertices are shown below the buttons as well

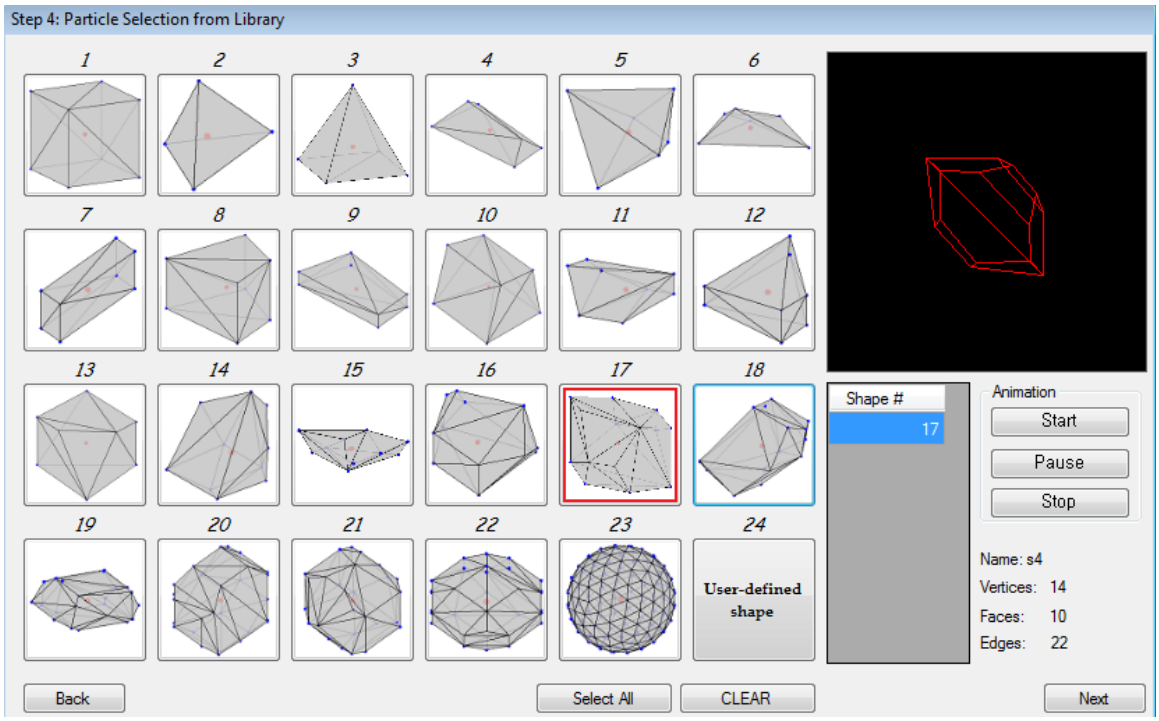

Figure 7.6. Step 4. Particle Selection Window

Step 5: Initial Particle Location

The initial locations of particles are generated as shown in Figure 7.7. For example, the particles should be generated in the air above the container for a simulation pouring particles into a container. In this version of BALLAST-BLOKS3D.app, there are four methods to generate particle locations. The user can place the particles manually one by one by using **Add Particle** button. Whenever the button is clicked, a row in the spreadsheet on the right will be added with all 0s shown in the cells. The user then may want to specify the location manually. Likewise, it is also possible to remove the particles with the Remove Particle button. The Clear button will delete all the particle information shown on the spreadsheet.

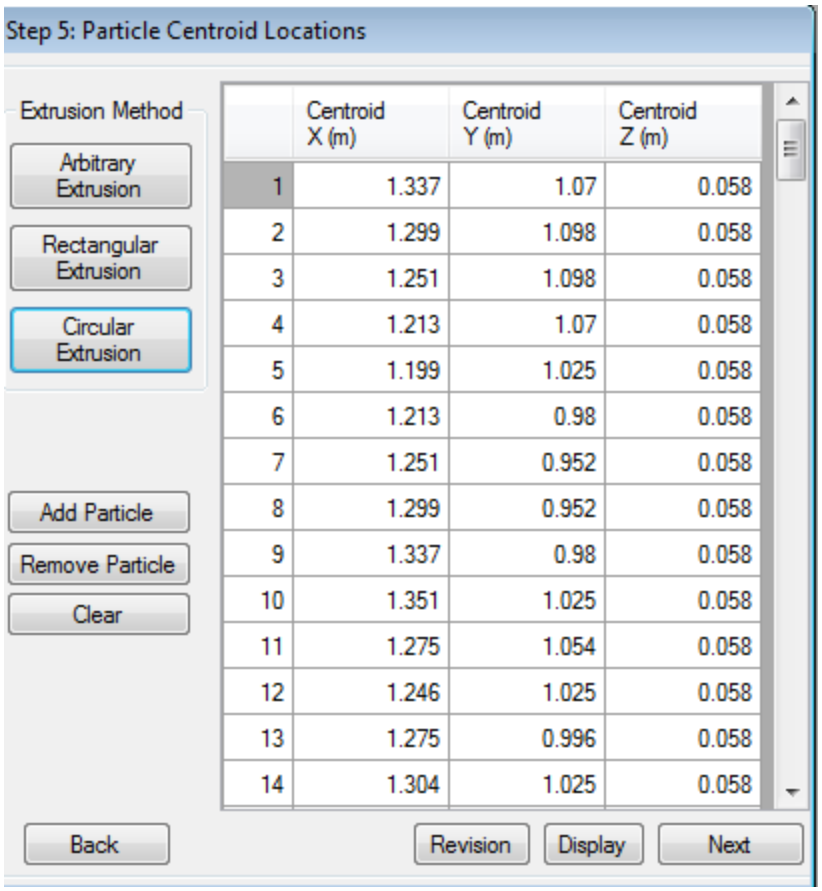

	Centroid X (m)	Centroid Y (m)	Centroid Z (m)
1	1.337	1.07	0.058
2	1.299	1.098	0.058
3	1.251	1.098	0.058
4	1.213	1.07	0.058
5	1.199	1.025	0.058
6	1.213	0.98	0.058
7	1.251	0.952	0.058
8	1.299	0.952	0.058
9	1.337	0.98	0.058
10	1.351	1.025	0.058
11	1.275	1.054	0.058
12	1.246	1.025	0.058
13	1.275	0.996	0.058
14	1.304	1.025	0.058

Figure 7.7. Step 5. Initial Particle Location Window

Step 6: Material Definition and Assignment

The user uses a dialog box to define the specific gravity and assign it to the generated particles. The material number is automatically assigned to all particles generated in the Material Assignment spreadsheet as shown in Figure 7.8. The user can use the tilde (~) to set the range of particle numbers. There is no default *Specific Gravity* value set in the Material Definition spreadsheet. To add a *Specific Gravity* value, the user can simply click **Add Material** button while the **Remove Material** button is used to delete a value.

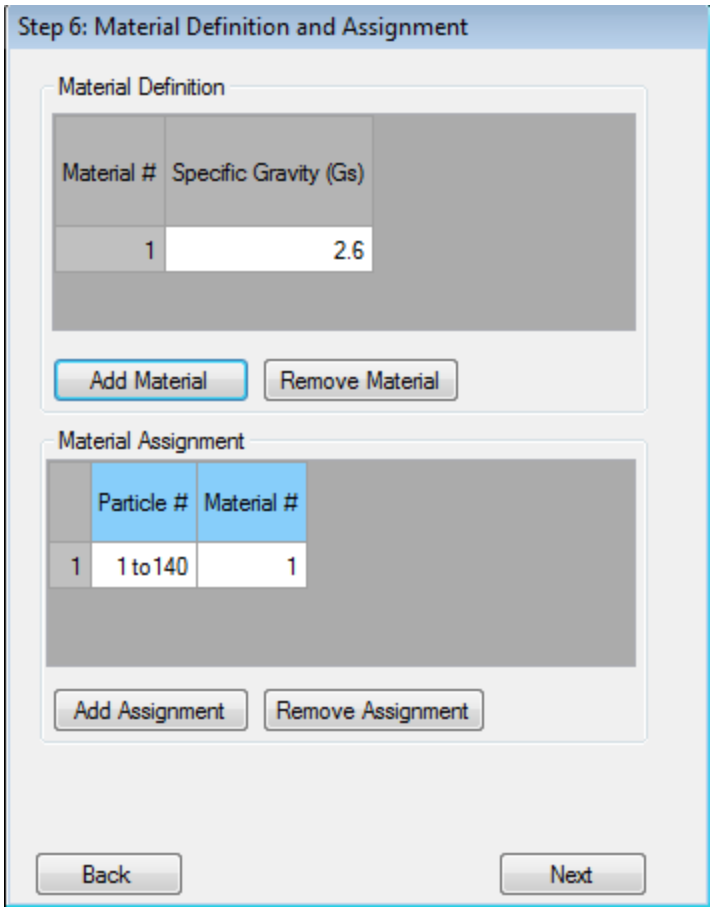

Figure 7.8. Step 6. Material Definition and Assignment

Step 7: Contact Parameters and Global Variables

The user determines contact parameters such as contact stiffness and friction angle as well as some global variables such as global damping. Inputs include normal stiffness, shear stiffness and inter particle friction angle values between the materials, and default values are assigned to the *Contact Damping/Global Damping*, the *Time Step Fraction Number* and the *Nonlinear Elastic Contact Parameter* fields. Figure 7.9 shows the contact parameters and global variables window.

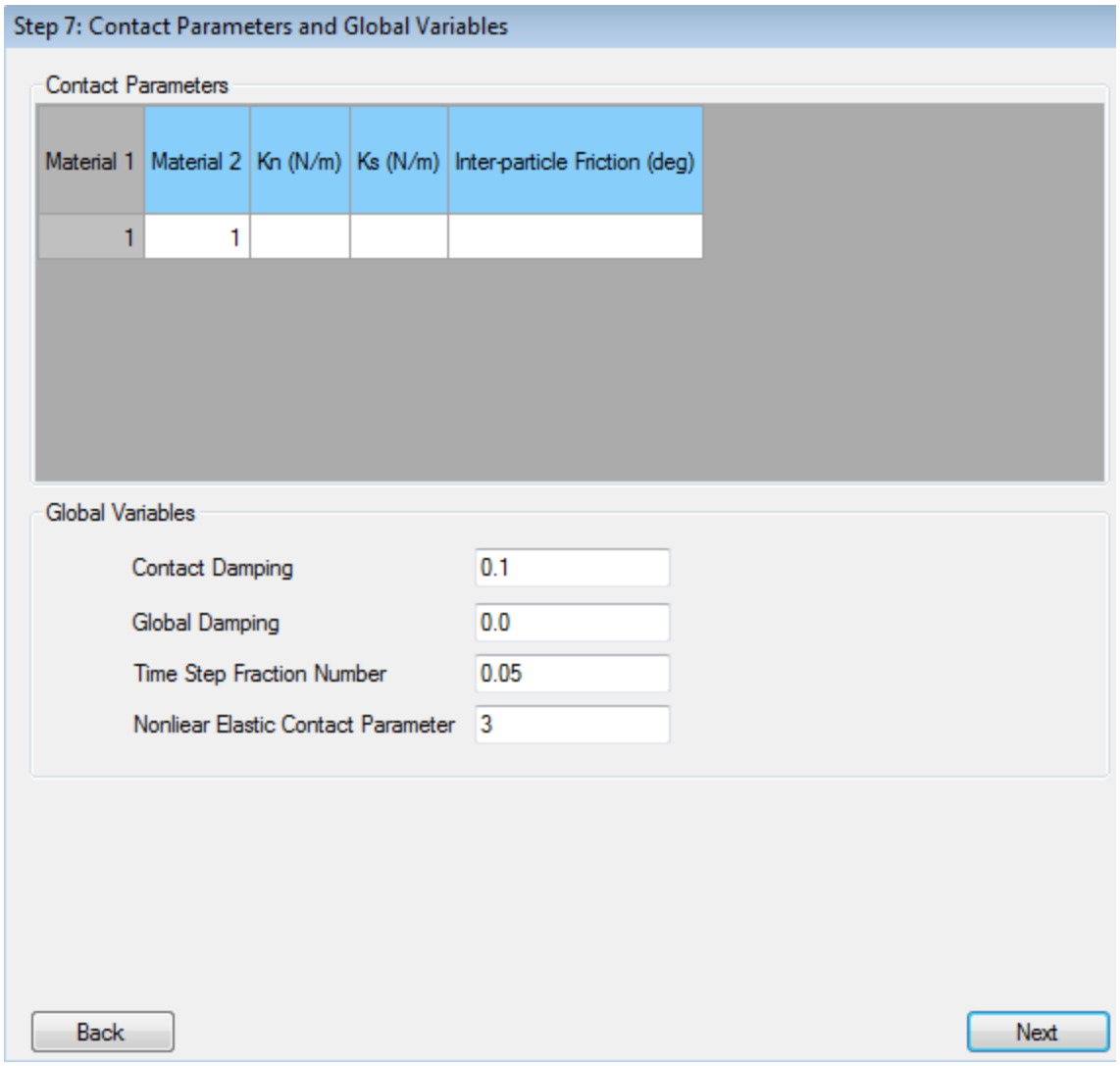

Figure 7.9. Step 7. Contact Parameters and Global Variables

Step 8: Additional Controls

The user can set the duration of the simulation and verify the final configuration generated via BALLAST-BLOKS3D.post (the post-processor). Once the user is at Step 8, the dialog box will show the time step that was calculated from the information entered in the previous steps. The simulation time can be entered in the *Duration of simulation* field, and then BALLAST-BLOKS3D.app will calculate the required number of time steps.

The user can click the **Finish** button to generate the project file, the input file and the batch file as shown in Figure 7.10. At the same time, the batch file will be run to feed the input file to BALLAST-BLOKS3D.anl only for the 1st time step to show the generated initial particle configuration. This configuration will then be shown in BALLAST-BLOKS3D.post. Once the correctness of the modeling is checked, the user can continue the simulation with the **Run** button for the duration of the simulation set.

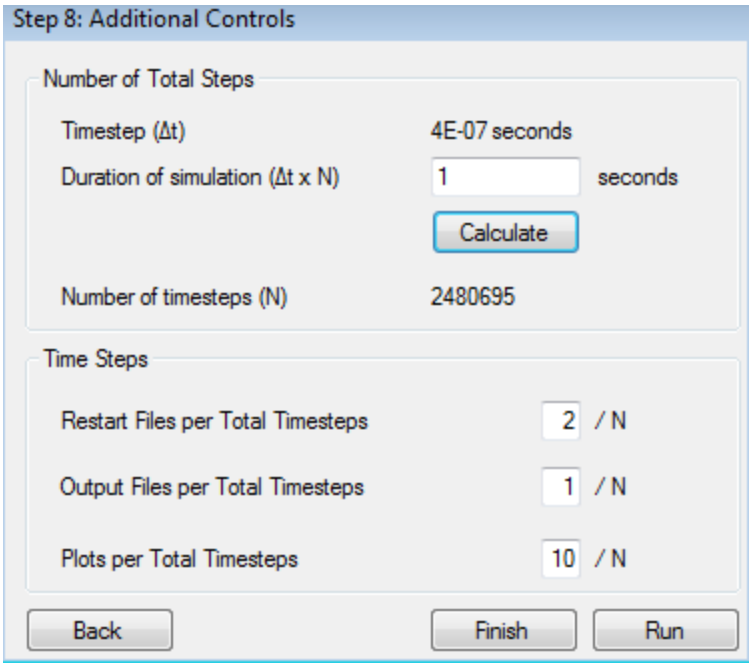

Figure 7.10. Step 8. Additional Controls Window

8. Conclusion

Since railroad ballast layer consists of discrete aggregate particles, the DEM is the most widely adopted numerical method for simulating the particulate nature of ballast materials and their particle interactions. The experimental study and numerical analyses performed by UIUC demonstrated that the DEM simulation approach, combined with image analysis, could serve as a quantitative tool that can predicts ballast performance. Both large scale triaxial monotonic strength tests and repeated loading tests with clean ballast that met AREMA No. 24 gradation have been successfully simulated with the dedicated ballast behavior DEM simulation program BALLAST-BLOKS3D. The key findings of this study are:

1. A dynamic track model was developed with discrete tie support and 3D subgrade that provided realistic load pulse shapes, magnitudes and rest periods acting on the ballast in the field. Accordingly, one load cycle applied on ballast specimens in the laboratory testing program and the DEM model simulations adequately considered the characteristics of the track, individual car axle spacing, car length, multiple wheel load interaction and train speed.
2. The experimental study indicated that the shearing rate has an insignificant influence on the results of the triaxial compression tests when using clean ballast.
3. The software DEM simulations can capture the measured shearing response of clean ballast during triaxial strength tests and repeated loading tests, and the IDSM adopted in DEM simulation can save significant computational resources and CPU time.
4. The initial configuration proved to be extremely important during the numerical simulation. The discrepancy caused by differing initial configurations can be successfully reduced by taking averages of several DEM results.
5. In a controlled laboratory environment, LA abrasion test equipment generated significant amounts of fouled ballast materials by abrading and breaking large particles into smaller particles and fine materials.
6. The FI, which is the summation of percentage by weight of ballast sample passing the 4.75 mm (No. 4) sieve and the percentage passing the 0.075 mm (No. 200) sieve, is a good indicator of ballast fouling conditions. As the FI approached 40, nearly all the voids among the larger particles were filled by finer materials resulting from ballast degradation.
7. After LA abrasion testing was completed, an image analyses of particles larger than 9.5 mm or 3/8 in. presented clear trends of alternation in both particle size and shape (i.e., flatness and elongation as well as angularity and surface texture). Statistically significant correlations were found between FI and the overall shape reductions in imaging-based on angularity and surface texture indices of the aggregate particles larger than 9.5 mm or 3/8 in.
8. Clean and fouled ballast samples differed considerably in permanent deformation behavior trends during repeated load triaxial testing. Coarse aggregate fraction of fouled ballast yielded higher permanent deformation than clean ballast due to variation in gradation and particle shape properties. Fouled ballast yielded higher permanent

deformations than those of the coarse aggregate fraction of the fouled ballast samples when fines were included.

9. By using the same gradation and particle shape properties, BALLAST-BLOKS3D successfully captured the permanent deformation behavior of clean ballast and coarse aggregate fraction of fouled ballast during large-scale repeated load triaxial testing.

This study focused on a limestone type ballast material and large scale triaxial testing in the laboratory under controlled monotonic and repeated loading conditions for shear strength, modulus, and deformation characteristics. Commonly used aggregate materials such as granite, trap rock and quartzite should also be tested in the laboratory. Additionally, there is a major gap in our understanding of such important effects of (i) different clean ballast gradations such as AREMA No. 3, No. 4 and No. 24, (ii) in-service or field ballast conditions (their degradation and fouling due to dynamic train loading), and (iii) moisture conditions of in-service ballast associated with partial to full saturation (associated field pumping) states.

These aspects need to be further studied in the laboratory for their effects on mechanics behavior. In addition, a relatively simple test needs to develop to study drainage and permeability aspects of the materials as a function of ballast grades. Finally, the degradation and abrasion potential of ballast aggregate materials may also be evaluated in the laboratory using a Micro-Deval type test, which tends to polish (smoothen) aggregate particles, and then the Micro-Deval test evaluates the abrasion resistance and frictional properties, while the LA abrasion test tends to break them.

To properly model the life-cycle degradation of a ballast material, all the ballast particle size, shape, and texture and angularity properties have to be taken into account at different track tonnage levels and how it linked to degradation trends. This can be incorporated into DEM simulation model parameter selection by developing cyclic interface constitutive laws that allow the behavior to mimic the degradation observed in the laboratory experiment or, more realistically, from field degradation trends. In addition to degradation and fouling of ballast gradation, moisture conditions that affect in-service aged ballast materials should be studied for partial to full saturation conditions, which are often associated with pumping and increased field degradation.

The BALLAST-BLOKS3D DEM program should be further developed as a quantitative ballasted track performance tool for modeling degraded/fouled ballast composition and life-cycle behavior, and to improve the ability to recognize the realistic field ballast degradation trends.

9. References

Agui, J. H., Hashash, Y. M. A., Lee, S. J., and Wilkinson, R. A. (n.d.). Simulation of Jsc-1a Lunar Soil Simulants with New Algorithms Developed for Realistic Soil Particle Geometries. *in Multiscale and Multiphysics Processes in Geomechanics (Results of the Workshop on Multiscale and Multiphysics Processes in Geomechanics* (pp. 193–196). Springer-Verlag Berlin Heidelberg.

Ahuja, N., Hart, J. M., Moaveni, M., Tutumluer, E., and Wang, S. (2013). Aggregate Size and Shape Evaluation Using Segmentation Techniques and Aggregate Image Processing Algorithms. *Transportation Research Record: Journal of the Transportation Research Board*. Retrieved from http://docs.trb.org/prp/13-4167.pdf

Anderson, W. F., and Fair, P. (2008). Behavior of Railroad Ballast under Monotonic and Cyclic Loading. *Journal of Geotechnical and Geoenvironmental Engineering, 134*(3), 316-327.

Andersson, C., and Oscarsson, J. (1999). Dynamic train/track interaction including state-dependent track properties and flexible vehicle components. *Vehicle System Dynamics: Supplement, 33*, 47-58.

Andrade, J. E., Lim, K.-W., Avila, C. F., and Vlahinić, I. (2012). Granular element method for computational particle mechanics. *Computer Methods in Applied Mechanics and Engineering, 241–244*, 262–274.

Armitage, R., Collop, A. C., Lim, W. L., McDowell, G. R., and Thom, N. H. (2005). Laboratory Simulation of Train Loading and Tamping on Ballast. *Proceedings of the Institution of Civil Engineers, 158*(2), 89-95.

Aursudkij, B. (2005). *Behaviour under Traffic Loading and Tamping Maintenance.* The University of Nottingham.

Aursudkij, B., Collop, A. C, and McDowell, G. R. (2009). Cyclic loading of railway ballast under triaxial conditions and in a railway test facility. *Granular Matter*, 391–401.

Banimahd, M., Kaddouri, A., Woodward, P. K., and Zettor, B. (2005). Advanced Non-Linear Dynamic Finite Element Modeling of Railway Track Behavior. *8th International Railway Engineering Conference.*

Barbosa, R., and Ghaboussi, J. (1990). Three-dimensional discrete element method for granular materials. *International Journal for Numerical and Analytical Methods in Geomechanics, 14*(7), 451–472.

Bardet, J. P. (1994). Numerical simulation of the incremental responses of idealized granular materials. *International Journal of Plasticity, 10*(8), 879–908.

Bathurst, R. J., and Raymound, G. P. (1994). Repeated-load response of aggregates in relation to track quality index. *Canadian Geotechnical Journal, 31*(1), 547–554.

Blader, F., Samavedam, G., Snyder, M., Thomson, D., and Wormley, D. (1997). *Analyses of Track Shift Under High-Speed Vehicle-Track Interaction.* Washington, DC: Federal Railroad Administration. Retrieved from https://www.fra.dot.gov/eLib/details/L16761#p2_z5_gD_lRT_y1997

Boucher, D. L., and Selig, E. T. (1990). Abrasion Tests for Railroad Ballast. *Geotechnical Testing Journal, 13*(4), 301–311.

Brown, S. F., and Thom, N. H. (1988). The Effect of Grading and Density on the Mechanical Properties of a Crushed Dolomitic Limestone. *14th Australian Road Research Board Conference*, *14*, pp. 94–100.

Cai, Z., and Raymond, G. P. (1994). Modeling the dynamic response of railway track to wheel/rail impact loading. *Structural Engineering and Mechanics, 2*(1), 95–112.

Cundall, P. A. (1988). Formulation of a Three-Dimensional Distinct Element Model—Part I. A Scheme to Detect and Represent Contacts in a System Composed of Many Polyhedral Blocks. *International Journal of Rock Mechanics and Mining Sciences & Geomechanics Abstracts, 25*(3), 107–116.

Cundall, P. A., and Strack, O. D. L. (1979). A discrete numerical model for granular assemblies. *Geotechnique, 29*(1), 47–65.

David, D. D., Ghaboussi, J., Hashash, Y. M. A., Qian, Y., and Tutumluer, E. (2011). Field Validated Discrete Element Model for Railroad Ballast. *In Proceedings of AREMA Annual Conference.*

Davis, D. D., Ghaboussi, J., Hashash, Y., Qian, Y., and Tutumluer, E. (2013). Discrete element modelling of ballasted track deformation behaviour. *International Journal of Rail Transportation, 1*(1-2), 57–73.

Dawson, A., Isacsson, U., and Lekarp, F. (2000). State of the Art. II: Permanent Strain Response of Unbound Aggregates. *Journal of Transportation Engineering, 126*(1), 76–83.

Diyaljee, V. A. (1987). Effects of Stress History on Ballast Deformation. *Journal of Geotechnical Engineering, 113*(8), 909–914.

Dombrow, W., Huang, H., and Tutumluer, E. (2008). Laboratory Characterization of Coal Dust Fouled Ballast Behavior. *Proceedings of AREMA Annual Conference.* Retrieved from https://www.arema.org/files/library/2008_Conference_Proceedings/Laboratory_Characterization_of_Coal_Dust_Fouled_Ballast_Behavior_2008.pdf

Ebrahimi, A., Edil, T. B., and Tinjum, J. M. (2010). Large-Scale Cyclic Triaxial Testing of Rail Ballast. *AREMA Annual Conference.*

Frenkel, R., Selig, E. T., and Suiker, A. S. J. (2005). Static and Cyclic Triaxial Testing of Ballast and Subballast. *Journal of Geotechnical and Geoenvironmental Engineering, 131*(6), 771–782.

Garcia, X., Guises, R., Latham, J.-P., Munjiza, A., and Xiang, J. (2008). Three-dimensional particle shape acquisition and use of shape library for DEM and FEM/DEM Simulation. *Minerals Engineering, 21*(11), 797–805.

García-Rojo, R., Herrmann, H. J., and Peña, A. A. (2007). Influence of particle shape on sheared dense granular media. *Granular Matter, 9*(3-4), 279–291.

Garg, N., and Thompson, M. R. (1997). Triaxial Characterization of Minnesota Road Research Project Granular Materials. *Transportation Research Record, Journal of the*

Transportation Research Board, 27–36. Retrieved from http://trrjournalonline.trb.org/doi/pdf/10.3141/1577-04

Gehringer, E., Kazmee, H., Mishra, D., Pforr, J., Read, D., and Tutumluer, E. (2013). Characterization of Railroad Ballast Behavior under Repeated Loading Using a New Large Triaxial Test Setup. *Transportation Research Record: Journal of the Transportation Research Board*.

Ghaboussi, J., Hashash, Y. M. A., Huang, H., and Tutumluer, E. (2006). Aggregate Shape Effects on Ballast Tamping and Railroad Track Lateral Stability. *In AREMA Annual Conference.* Louisville, KY. Retrieved from https://www.arema.org/files/library/2006_Conference_Proceedings/067.pdf

Ghaboussi, J., Hashash, Y. M. A., Huang, H., and Tutumluer, E. (2007). Discrete Element Modeling of Railroad Ballast. *In AREMA Annual Conference.*

Ghaboussi, J., Hashash, Y. M. A., Huang, H., and Tutumluer, E. (2009). AREMA Gradations Affecting Ballast Performance Using Discrete Element Modeling (DEM) Approach. *In Proceedings of the AREMA 2009 Annual Conference.* Chicago, IL. Retrieved from https://www.arema.org/files/library/2009_Conference_Proceedings/AREMA_Gradations_Affecting_Ballast_Performance_Using_Discrete_Element_Modeling_DEM_Approach.pdf

Ghaboussi, J., Hashash, Y. M. A., Nezami, E. G., and Zhao, D. (2006). Shortest link method for contact detection in discrete element method. *International Journal for Numerical and Analytical Methods in Geomechanics, 30*, 783–801. Retrieved from ftp://crack.seismo.unr.edu/downloads/russell/common_plane/nezami_2006_shortest_link_method_cp.PDF

Ghaboussi, J., Hashash, Y. M. A., Nezami, E. G., and Zhao, D. (2006). Three-dimensional discrete element simulation for granular materials. *Engineering Computations, 23*, 749–770. Retrieved from ftp://crack.seismo.unr.edu/downloads/russell/zhao_2006_3D_dem_granular_materials.PDF

Ghaboussi, J., Hashash, Y. M. A., Nezami, E. G., and Zhao, D. (2007). Simulation of front end loader bucket-soil interaction using discrete element method. *International Journal for Numerical and Analytical Methods in Geomechanics, 31*, 1147–1162.

Ghaboussi, J., Hashash, Y. M. A., Nezami, E., and Zhao, D. (2004). A fast contact detection algorithm for 3-D discrete element method. *Computers and Geotechnics, 31*(7), 575–587.

Grassie, S. L., and Knothe, K. L. (1993). Modelling of Railway Track and Vehicle/Track Interaction at High Frequencies. *Vehicle System Dynamics: International Journal of Vehicle Mechanics and Mobility, 22*(3-4), 209.

Han, X., and Selig, E. T. (1996). *Investigation of the Effects of Fouling Material and Degree of Fouling on the Settlement of Ballast Bed by Ballast Box.* Project Report for Association of American Railroads.

Hashash, Y. M. A., Lee, S. J., and Nezami, E. G. (2012). Simulation of triaxial compression tests with polyhedral discrete elements. *Computers and Geotechnics, 43*, 92–100.

Hicks, R. G. (1970). *Factors Influencing the Resilient Properties of Granular Materials.* University of California, Berkeley.

Hicks, R. G. and Monismith, C. L. (1971). Factors Influencing the Resilient Response of Granular Materials. *Highway Research Record*(345), 15-31.

Hogue, C., and Newland, D. (1994). Efficient computer simulation of moving granular particles. *Powder Technology, 78*(1), 51–66.

Horvli, I., Noålsund, R., and Tutumluer, E. (2013). Degradation of railway ballast through large scale triaxial and full scale rail track model tests-comparison with mechanical laboratory tests. *10th International Conference on Bearing Capacity of Roads, Railways and Airfields.* Retrieved from https://www.researchgate.net/profile/Roar_Nalsund/publication/281112173_Degradation_of_railway_ballast_through_large_scale_triaxial_and_full_scale_rail_track_model_tests_-Comparison_with_mechanical_laboratory_tests/links/55d6402a08ae9d65948bcea4/Degradati

Hu, Y., and Kempfert, H. G. (1999). Rediction on the Long-Term Behavior of Subsoils under High-Speed Railways. *XII European Conference on Soil Mechanics and Geotechnical Engineering*.

Huang, H., and Tutumluer, E. (2011). Discrete Element Modeling for fouled railroad ballast. *Construction and Building Materials, 25*(8), 3306–3312.

Huang, H., Dombrow, W., and Tutumluer, E. (2009). Laboratory Characterization of Fouled Railroad Ballast Behavior. *Transportation Research Record: Journal of the Transportation Research Board, 2117*, 93–101. Retrieved from http://railtec.illinois.edu/articles/Files/Journal%20Articles/2009/Huang%20et%20al%202009_1.pdf

Huang, H., Shen, S., and Tutumluer, E. (2010). Moving load on track with asphalt trackbed. *Vehicle Systems Dynamics: International Journal of Vehicle Mechanics and Mobility, 48*(6), 737-749.

Indraratna, B., Ionescu, D., and Christie, H. D. (1998). Shear Behavior of Railway Ballast Based on Large-Scale Triaxial Tests. *Journal of Geotechnical Geoenvironmental Engineering, 124*(5), 439–449.

Indraratna, B., Lackenby, J., and McDowell, G. (2007). Effect of confining pressure on ballast degradation and deformation under cyclic triaxial loading. *Geotechnique, 57*(6), 527–536.

Indraratna, B., Ngo, N. T., Rujikiatkamjorn, C., and Vinod, J. S. (2012). Behaviour of Fresh and Fouled Railway Ballast Subjected to Direct Shear Testing: Discrete Element Simulation. *International Journal of Geomechanics, 14*(1).

Indraratna, B., Nimbalkar, S. S., Tennakoon, N. C., and Rujikiatkamjorn, C. (2013). Behaviour of clay-fouled ballast under drained triaxial testing. *Geotechnique: International Journal of Soil Mechanics, 63*(5), 410–419. Retrieved from http://ro.uow.edu.au/cgi/viewcontent.cgi?article=1593&context=eispapers

Indraratna, B., Thakur, P. K., and Vinod, J. S. (2010). Experimental and Numerical Study of Railway Ballast Behavior under Cyclic Loading. *International Journal of Geomechanics, International Journal of Geomechanics*(4), 136–144.

Iwashita, K., and Oda, M. (2000). Micro-deformation mechanism of shear banding process based on modified distinct element method. *Powder Technology, 109*(1-3), 192–205.

Kacianauskas, R., and Markauskas, D. (2006). Compacting of Particles for Biaxial Compression Test by the Discrete Element Method. *Journal of Civil Engineering and Management, 12*(2), 153–161.

Lim, W. L. (2004). *Mechanics of Railway Ballast Behaviour.* The University of Nottingham. Retrieved from http://eprints.nottingham.ac.uk/10060/1/Thesis.pdf

Lu, M., and McDowell, G. R. (2010). Discrete element modelling of railway ballast under monotonic and cyclic triaxial loading. *International Journal of Soil Mechanics, 60*(6), 458–466.

Mesri, G., Peck, R. B., and Terzaghi, K. (1996). *Soil Mechanics in Engineering Practice.* John Wiley & Sons Inc.

Mollon, G., and Zhao, J. (2013). Generating realistic 3D sand particles using fourier descriptors. *Granular Matter, 15*(1), 95–108.

O'Connor, R., and Williams, J. R. (1999). Discrete element simulation and the contact problem. *Archives of Computational Methods in Engineering, 6*(4), 279–304.

Olson, S. M., and Sadrekarimi, A. (2011). Critical state friction angle of sands. *Geotechnique, 61*(9), 771–783.

Raymond G. P. (2002). Reinforced ballast behaviour subjected to repeated load. *Geotextiles and Geomembranes, 61*(9), 771–783.

Sallam, A. M. (2004). *Studies on Modeling Angular Soil Particles Using the Discrete Element Method.* Department of Civil and Environmental Engineering. University of South Florida. Retrieved from http://citeseerx.ist.psu.edu/viewdoc/download?doi=10.1.1.875.5674&rep=rep1&type=pdf

Selig, E. T., and Waters, J. M. (1994). *Track Geotechnology and Substructure Management.* London: Thomas Telford Services Ltd.

Shenton, M. J. (1975). Deformation of Railway Ballast under Repeated Loading Conditions. 387–404.

Tonon, F., and Wang, Y. (2009). Modeling Triaxial Test on Intact Rock Using Discrete Element Method with Membrane Boundary. *Journal of Engineering Mechanics, 135*(9), 1029–1037.

Abbreviations and Acronyms

2D	Two-Dimensional
3D	Three-Dimensional
AI	Angularity Index
C_c	Coefficient of Curvature, $C_c=(D_{30})^2/(D_{60}\square D_{10})$
C_u	Coefficient of Uniformity, $C_u=(D_{60}\square D_{10})$
CP	Common Plane
D_{10}	Grain Diameter at 10% Passing
DEM	Discrete Element Method
E-UIAIA	Enhanced University of Illinois Aggregate Image Analyzer
FFT	Fast Fourier Transform
FEM	Finite Element Method
FI	Fouling Index
F&E	Flat and Elongated Ratio
GSD	Gain Size Distribution
GUI	Graphical User Interface
ICT	Illinois Center for Transportation
IDSM	Incremental Displacement Shearing Method
LA	Los Angeles Abrasion Test
LVDT	Linear Variable Displacement Transducer
RailTEC	Rail Transportation and Engineering Center
ST	Surface Texture Index
TX-24	Triaxial Test Device at the University of Illinois
UIAIA	University of Illinois Aggregate Image Analyzer
UIUC	University of Illinois at Urbana-Champaign
RTF	Railway Test Facility